MASTER

Measurements and modelling of transmission of radiowaves through buildings

Koelen, M.H.J.L.

Award date:
2000

Eindhoven University of Technology
Faculty of Electrical Engineering
Division of Telecommunication Technology and Electromagnetics
Radiocommunications Group

Measurements and modelling of transmission of radiowaves through buildings

By Ing. M.H.J.L. Koelen

Abstract

At present many microcell propagation tools are being developed to predict the fieldstrength distribution around a base station (BS) in a microcell. The μFiPre model, developed at Eindhoven University of Technology, uses a 2D-environment database in which buildings are represented by smooth opaque block-type obstacles. The μFiPre model incorporates only direct, reflected, diffracted rays and their combinations. In order to model the fieldstrength distribution in a microcell more accurately, the transmission of radio waves through buildings must be taken into account. In this report a model is presented that predicts the fieldstrength due to transmission of radio waves through buildings.

This model is based on outdoor building measurements carried out using a wideband channel sounder, which operates at 1900 MHz and has a temporal resolution of 20 ns. During a building measurement a vertically polarised omnidirectional transmitting antenna was placed at one side of the building and a vertically polarised dipole receiving antenna at the other side of the building.

The angular superresolution algorithm UCA-MUSIC was used to calculate the angle of arrival (AoA) of the incident wavefronts that arrive at the receiving antenna. This AoA can be used to distinguish the different mechanisms of propagation (reflection, diffraction, scattering and transmission). With each AoA measurement we can determine the fieldstrength for only one position behind a building. As we are interested in the total fieldstrength distribution behind a building we should perform an infinite number of AoA measurements, which are complex and time consuming. Therefore a measurement method has been developed for a fast and accurate measurement of transmission of radio waves through buildings.

The transmission model based on these measurements models the field due to transmission through a building as if it were the result of a single transmitted ray directly from the source through the building to the observation point. The building transmission loss, defined as the loss associated with this ray path relative to free-space loss, can be modelled as the sum of all losses due to the building along the transmitted ray trajectory. These losses include the transmission losses at the two interfaces between the building interior and free-space and all remaining losses due to obstructions inside the building. These remaining losses are accounted for by a specific building loss coefficient.

The transmission model was compared with measurement results, where the possible differences could be explained by the internal structure of the buildings. For one building a specific transmission model was developed which improves the basic transmission model by including the attenuation due to the internal walls.

The specific building loss coefficient was thought to be related to the type of building, therefore the buildings within a microcell were categorised (residential row houses, apartments, shops located beneath apartments and office buildings). Extra measurements

Acknowledgements

I would like to use this page of my report, to express my sincere gratitude to the people involved in my M.Sc. project.

First of all I would like to thank Prof. dr. ir. G. Brussaard, who gave me the opportunity for working on this project.

I also would like to thank ir. Y.L.C. de jong and dr. ir. M.H.A.J. Herben, who coached me during the months I was working on my M.Sc. project.

I would like to thank the employees of the Radiocommunications group of the TUE who all contributed to my M.Sc. project.

Finally I would like to thank my family and friends, who supported me during my entire period of study.

Maikel.

Contents

List of figures

List of tables

Chapter 1

Introduction

This chapter gives an introduction of the M.Sc. project. Mobile radio communication is complex and diverse and is used in many applications. Which specific part this M.Sc. project occupies in the world of mobile radio communication will be clarified in the next paragraphs.

1.1 Background

The exponential growth of today's mobile users treatens the mobile radio network to overload. A lot of research is conducted to overcome this problem. One of the solutions is application of so-called advanced frequency-planning techniques, which provides a more efficient use of the channels available within the network. Only software adaptations have to be made to implement these techniques, and are therefore relatively cheap. However, these advanced frequency-planning techniques do not increase the number of channels available per unit area. Eventually, with the exponential growth in mind, the mobile radio network will reach its capacity in spite of the advanced frequency planning techniques. To increase the number of channels, microcells (smaller cells) must be used in parts of the network were the traffic intensity is very high.

For an accurate planning of cellular networks, propagation models are used which predict the electromagnetic fieldstrength around a base station (BS). For planning of the conventional macrocells statistical-empirical propagation models are being used. These models use parameters such as antenna height of the BS and mobile station (MS), the distance between the BS and the MS, frequency and terrain type. A well-known model that is based on these parameters is the so-called Okumura model [1]. Whereas the BS in macrocells is usually situated at a high elevation to cover a wide area, in microcells the BS is often placed below the average height of the surrounding buildings. Therefore the distribution of the electromagnetic fieldstrength is highly dependent on the local features of the environment (such as locations, shapes and dielectric properties of the buildings) and important channel characteristics such as path loss and delay spread become very location-specific. The statistical-empirical models only cover some general classification of the environment and therefore fail when used in a microcell environment. For reliable microcell planning new models have to be developed, which takes the complex building environment into account.

Presently many institutes and companies are developing their own deterministic models for the planning of microcells. These deterministic models are based on the physical phenomena of the propagation of radio waves. The prediction accuracy of these deterministic models is better than that of the statistical models, but is still unsatisfactory in some of the cases, especially when cells become smaller and smaller not only to deal with the explosive

growth of mobile subscribers, but also with the increasing bandwidth in a scenario where the available spectrum is scarce. This increasing bandwidth is needed for new applications such as mobile internet, which will be provided in the near future. Therefore new, more accurate deterministic models for the microcell environment need to be developed. With these new models better microcell planning (i.e. fewer base stations for achieving the same network capacity) can be achieved. This will lead to important cost savings.

To develop these more accurate deterministic microcell models the different mechanisms of radio propagation must be examined. The different mechanisms of radio propagation are complex and diverse and can generally be attributed to four basic propagation mechanisms: reflection, diffraction, scattering and transmission (see Figure 1.1).
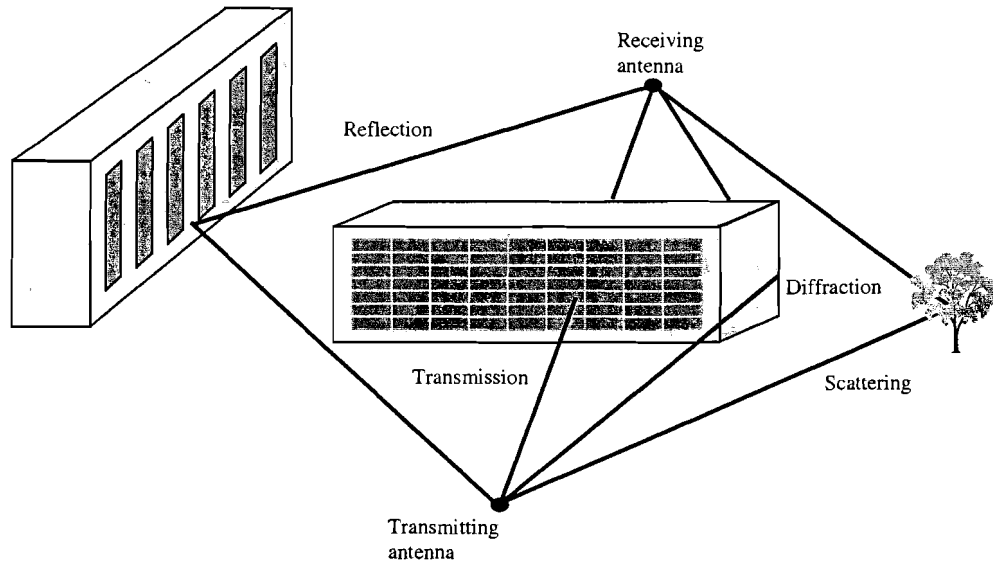
Figure 1.1: Different mechanisms of propagation.

Reflection occurs when a radio wave impinges on an obstruction with dimensions that are large compared to the wavelength of the radio wave. An example is reflection from the earth's surface or buildings. Diffraction occurs on edges, like building edges. Scattering occurs when the radio path includes objects with dimensions that are in the order of the wavelength or less than the propagation wave, such as tree elements (branches, leaves). Transmission is the mechanism in which the radio wave travels through a building. The existing microcell propagation models often model the buildings as opaque objects, therefore neglecting the transmission of radio waves. Whereas in macrocells transmission through buildings can be neglected, in microcells this mechanism is sometimes very important as can be seen in [2]. When using microcell propagation models a more accurate fieldstrength prediction can be achieved by including the transmission of radio waves. Most microcell propagation models use databases containing building locations and sizes for the fieldstrength predictions. This information can also be used for the modelling of transmission through buildings. Possible extra information about the buildings needed for the modelling of transmission through buildings is very costly and should therefore be avoided.

1.2 Recent work

In the recent past, Eindhoven University of Technology (EUT) developed the three dimensional ray-tracing model FiPre [3,4], which is based on geometrical optics (GO) and uniform theory of diffraction (UTD). The FiPre prediction tool uses a 3D-environment

database in which buildings are represented by smooth opaque block-type obstacles. This model was first developed for satellite communication, but was later adapted for microcellular mobile radio communication systems [5]. Fieldstrength calculations with these models were very time consuming because of the 3D nature and consequently only small databases could be used. Therefore a new 2D-propagation model (2D-µFiPre) was developed at EUT. The µFiPre model [6] is a 2D ray-tracing model based on GO and UTD. This model incorporates direct, reflected, diffracted rays and their combinations. The buildings are modelled as 2D (lossy) dielectric scatterers ($\varepsilon_r' = 5.3$) with plane, smooth impedance faces. The reflected field amplitudes are computed using the reflection coefficient for plane constant-impedance interfaces [7]. The waves diffracted from the vertical building edges are evaluated using the UTD diffraction coefficient proposed in [8]. When comparing 2D-models with 3D-models, great advantages could be found in the reduced fieldstrength calculation time. Different building heights cannot be modelled by 2D-models, which constitutes a disadvantage of 2D-models compared to 3D-models in cases where the BS is situated above the average building heights.

The results of the 2D-µFiPre model are generally in good agreement with the measured electromagnetic fieldstrength in microcell environments with the BS located below the average height of the surrounding buildings. In some of the cases however, there still is a discrepancy between theory and practice. The received electromagnetic field is generally the composition of contributions due to different mechanisms of propagation, see Figure 1.1. To determine the cause of the discrepancy between theory and practice one must identify the different mechanisms of propagation. For this purpose a high-resolution angle of arrival (AoA) method [9-11] was developed at Eindhoven University of Technology. Knowing the AoA with respect to the receiving antenna, the different mechanisms of propagation can be easily distinguished.

With decreasing cell areas (microcells) and decreasing BS transmission heights, transmission may be the prime mechanism by which the power is transferred from the transmitter to receiver. Concerning transmission models there is little or nothing to be found in the literature. In [12,13] building penetration models are presented which could be a start for the modelling of transmission through buildings. These models try to accommodate the building penetration losses based on external wall losses as a function of incidence angle, internal wall losses, floor losses and an extra internal attenuation (dB/m). The models given in [12,13] use the internal structure of the building in the prediction of the penetration loss. In practice however, there is no information about the internal structure of the building. It is therefore impossible to use these models in the fieldstrength prediction of microcells.

1.3 Scope and Outline of the report

The objective of this M.Sc. project is to develop a good transmission model that will need a minimum of information about the buildings. This model can then be used to adjust existing microcell models (in this case the µFiPre model), which often model buildings as opaque objects, for a more accurate field prediction.

The transmission model is based on outdoor building measurements; the experimental set-up that is used for these measurements is described in Chapter 2. To separate the field due to transmission from the other multipath contributions, the AoA of the incident rays with respect to the receiving antenna must be derived. The angular superresolution algorithm UCA-MUSIC, which is described in Chapter 3, is used to calculate these AoA. In Chapter 4 the measurement results are discussed and a measurement method is presented for a fast and accurate measurement of the field due to transmission through buildings. Chapter 5 describes

a basic transmission model. In Chapter 6 this model is compared with the measurement results. A more detailed transmission model based on the internal structure of a building is presented in Chapter 7, were it is compared with the measurement results. Some extra measurements were conducted in Chapter 8 to verify the basic transmission model. Finally, conclusions and recommendation are given in Chapter 9.

Chapter 2

Experimental set-up

This chapter gives a description of the measurement equipment that was used by the M.Sc. project. The experimental set-up, which is used to measure the complex impulse response (CIR) of the radio channel, consists of the parts shown in the figure below.
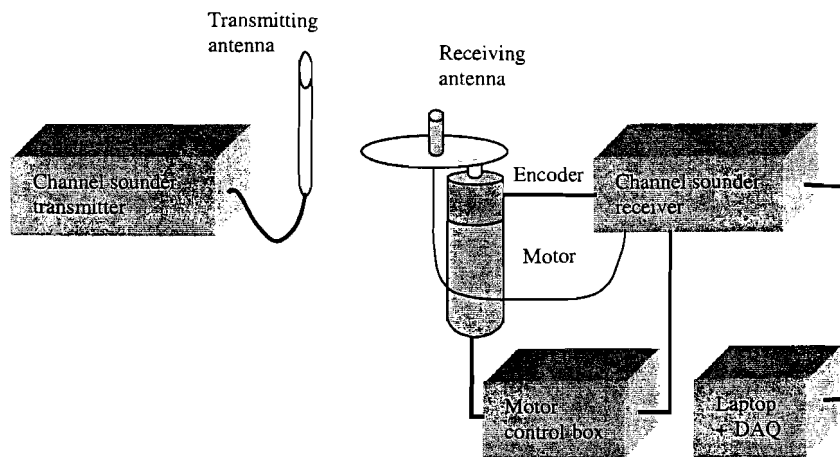
Figure 2.1: Experimental set-up.

The main part of the experimental set-up is the channel sounder, which will be explained in detail in the next paragraph. The channel sounder transmits a wideband pseudo noise (PN) sequence at 1.9 GHz by an omni directional antenna. Due to the multipath radio channel the channel sounder receives many delayed and attenuated sequences of the PN sequence by the receiving vertically polarised dipole antenna. The received signal is cross-correlated with a signal identical to the initial PN sequence to obtain an estimate of the complex impulse response. The receiving antenna is mounted on a stepper motor, which is driven by a motor control box. As the antenna rotates, burst acquisitions are triggered off at regularly spaced angles between 0° and 360°. The measurement taken over one revolution (i.e. 157 burst acquisitions) is called a snapshot. At each sampling position the data acquisition card (DAQ) samples the I and Q signals (see Figure 2.3), which provide information about the phase and amplitude of the CIR, and stores it on the hard disk. For AoA measurements, the measurement sequence must start at a fixed position. An encoder is therefore placed on top of the stepper motor, and gives a pulse everytime the motor passes a certain position. This pulse is used to start and end the measurement. At the receiver the Labview program, which is installed on the laptop controls the system. The program controls the data acquisition card (DAQ), rotation of the antenna, start of the sampling process, i.e. all the actions that are

needed for the experiment. In our experimental set-up the transmitter is mounted on a trailer, and the receiver in a vehicle. The receiving antenna together with the motor and the encoder are mounted on top of the vehicle.

2.1 Wideband channel sounder

The channel sounder is based on the popular pseudonoise (PN) correlation method [14,15]. The correlation property of the maximum-length PN binary sequence is used to estimate the complex impulse response of the radio channel under measurement. A PN binary sequence, $a(t)$, consists of a series of +1 and -1 transitions. These sequences are not random, but are sequences known both by the channel sounder transmitter and receiver. The sequences are called pseudonoise because their autocorrelation functions,

$$R_S(\tau) = \frac{1}{T} \int_0^T a(t)a(t-\tau)dt \qquad (2.1)$$

are similar to the autocorrelation of band-limited noise. The triangle of the autocorrelation has a base width of $2t_0$ and is periodic with period T because of the repeating nature of $a(t)$. This means that two echoes of equal amplitude can be separated if they are at least 20 ns apart. Figure 2.2 shows a schematic diagram of the channel sounder transmitter.
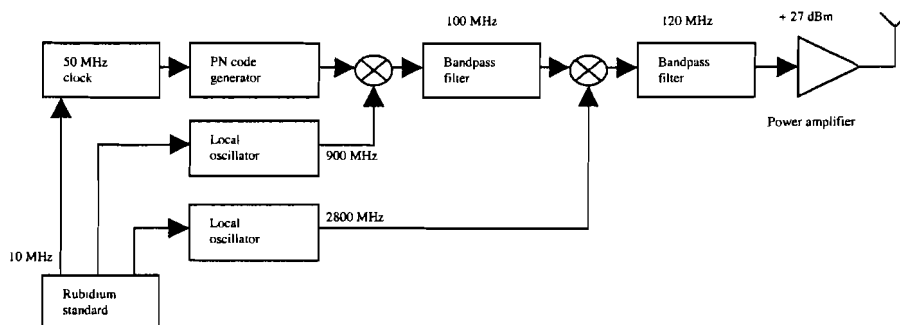
Figure 2.2: Channel sounder transmitter.

The PN code generator generates the PN binary sequence $a(t)$ with a length of 511 bits and a bit time of 20 ns. A 900MHz carrier is modulated by the PN binary sequence and bandpass filtered with a bandwidth of 100MHz. The resulting signal is again upconverted to 1900 MHz, bandpass filtered (120 MHz), amplified to 27 dBm and transmitted by a suitable antenna. The rubidium standard provides stability to all the local oscillators used by either the transmitter or the receiver.

At the channel sounder receiver, which is shown in Figure 2.3, the received signal is first bandpass filtered to reduce interference from unwanted sources. Subsequently, it is down converted from 1.9 GHz to 900 MHz. A step attenuator, controlled by a micro controller sets the signal level to the I/Q demodulator input. The input power level to the I/Q demodulator has to be carefully adjusted to provide the best dynamic range without distortion due to non-linearity. A wideband PN sequence, identical to the signal generated by the transmitter, is fed to the demodulator as the reference signal. The reference signal has a slightly lower frequency than the received signal. The reference signal is therefore time-shifted against the received signal and integrated, both in-phase and in-quadrature. This combination, time shifting and integration, performs the convolution action between the transmitted PN sequence and the received multipath signal. The output signal is digitised by the DAQ, and

stored on the hard disk. The I/O interface is the interface between the channel-sounder receiver, the DAQ, motor and encoder.

Figure 2.3: Channel sounder receiver.

2.2 Antennas

In the estimation of AoA of a wave impinging on a planar array a twofold ambiguity exists with respect to waves coming from the upper and lower hemisphere. To distinguish these waves we used an antenna with lower sensitivity towards the lower hemisphere. Further the applied angular resolution alg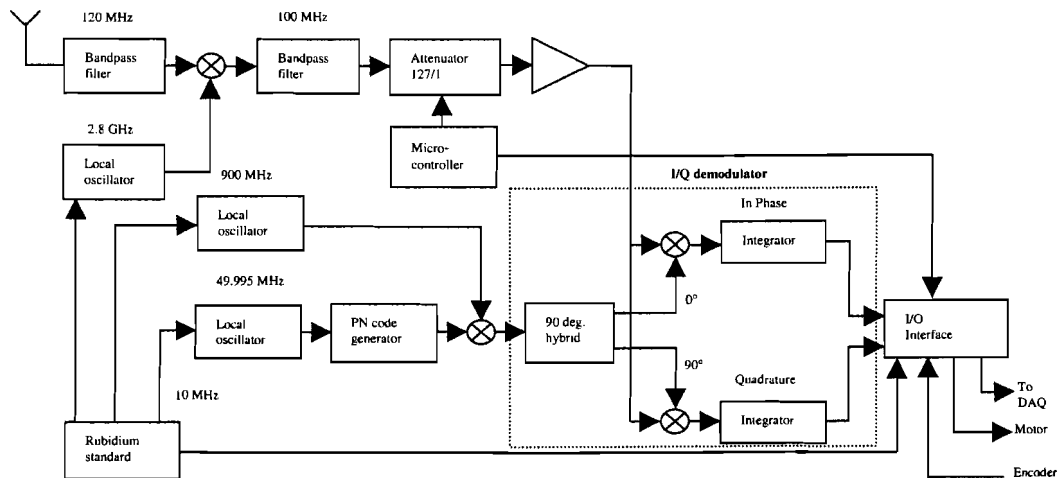orithm UCA-MUSIC assumes constant gain in the azimuth plane. Therefore we used a 2 dBi sleeve antenna with an omnidirectional radiation pattern in the azimuth plane, a vertical beamwitdth of 60° and maximum directivity for an elevation of +20°. The receiving antenna bandwidth extends from 1.7 to 2.0 GHz. As already told the receiving antenna is mounted on top of a vehicle. Reflection and diffraction of the incoming signals below the horizontal plane on the vehicle will result in distortion of the azimuth symmetry. To reduce these effects a circular groundplane with diameter $D = 5\lambda$ was mounted under the receiving antenna together with an electromagnetic absorbing plate. The receiving antenna is mounted on a stepper motor and synthesises a circular array. As the angular accuracy decreases with decreasing array radius, it is important to choose the array radius sufficient large. However, some other important factors also limit the size of the array radius.

1. *Plane Wave Assumption*: The UCA-MUSIC algorithm assumes that the electromagnetic field on the array is the sum of plane waves. Therefore the array size must be small compared to the distance of the array to the nearest scattering centre.
2. *Narrowband Array Assumption*: Each multipath contribution must arrive at the same time at all array elements. Therefore the array size should be small compared to the distance covered at the speed of light during a bit period.
3. *Practical considerations*: Practical requirements with respect to size and weights also put limitations on the array radius.

An array radius of 30 cm was found to be a good compromise between the above factors. For the transmitting antenna we used a vertically polarised omnidirectional antenna with a gain of 2 dBi, so we have an uniform illumination of the building under test. The antenna bandwidth extends from 1850 to 1990 MHz

2.3 AoA measurement

When calculating the AoA by an algorithm such as UCA-MUSIC one must derive the covariance matrix from the stored data. That is the correlation between the signals from the different array elements (the rotating antenna synthesises an uniform circular array). To calculate the exact AoA the covariance matrix must be the true covariance matrix. This is impossible to achieve. Firstly to achieve the true covariance matrix, the covariance matrix must be averaged over an infinite number of snapshots in a stationair environment. Secondly, the environment consist of all kinds of statistical components such as moving trees, people and vehicles. Some statistical components can be easily avoided. Wind effects (moving trees) can be avoided by conducting the experiments on a day where there is no or little wind, and moving people can be avoided by conducting the experiments not on a working day. As for moving vehicles, the statistical averaging of many snapshots will strongly reduce their interference, which typically lasts a few seconds. A good compromise can therefore be found by averaging the covariance matrix over a finite number of snapshots, making it a good estimate of the true covariance matrix. Forward/ backward averaging can effectively double the number of snapshots as will be explained in paragraph 3.4.

2.4 Panorama camera

At each measurement location a 360-degrees photo was taken by a panorama camera to obtain a visual description of the surrounding environment of the mobile station. The panorama camera (Seitz Roundshot 35/35) can be mounted at the same position as the rotating antenna. A long rod was mounted on the vehicle for angular reference, and can be seen on the photo. The position of the rod in relation to the starting position of the antenna is fixed and known. UCA-MUSIC calculates the azimuth and elevation angle of the incident wavefronts with respect to the starting position of the antenna. With this and providing the panorama photo with a grid of degrees, taking the starting position of the antenna as the $0°$ position, one can directly relate the AoA to the panorama photo. This procedure gives a clear insight in the mechanisms of propagation.

Chapter 3

Angular superresolution

In our experimental set-up, a receiving antenna is placed at one side of a building and the transmitting antenna at the other side. To gain a good insight in the different mechanisms of propagation one must determine from which direction the incident wavefronts arrive at the receiving antenna. These directions of the incident wavefronts are called angles of arrival (AoA). The algorithm UCA-MUSIC [16,17] can be used for calculating the AoA of the incident wavefronts.

The rotating receiver antenna that was used in the experimental set-up synthesises a uniform circular array (UCA), consisting of M antenna elements, which are equally distributed along a circle (see Figure 3.1).
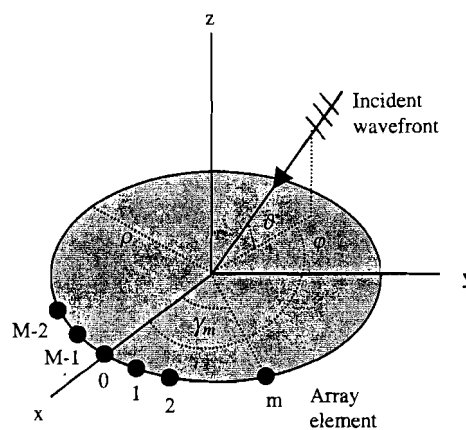
Figure 3.1 Circular antenna array.

At each antenna element a complex impulse response (CIR) of the radio channel is measured and stored on a hard disk. The covariance matrix, also called the array correlation matrix, is derived from this data. UCA-MUSIC uses this covariance matrix to calculate the AoA of the incident wavefronts; for example, UCA-MUSIC calculates the incident wavefront in Figure 3.1 by giving the elevation (ϑ) and azimuth (φ) angle with respect to a certain reference point.

3.1 Data model

First a data model will be derived to start the multiple signal classification approach. All multipath contributions, which add up to the total electromagnetic field received at the array elements, originate in the far field of the array (*Plane Wave Assumption*). The total

electromagnetic field on the array is therefore the sum of N plane waves. The correlation signal $y_m(\tau)$, at the mth antenna element ($m = 0,1,2,....., M\text{-}1$) can be written as

$$y_m(\tau) = \sum_{n=1}^{N} c_n g(\zeta_n) e^{j\zeta_n \cos(\varphi_n - \gamma_m)} x(\tau - T_n) + \eta_m(\tau). \tag{3.1}$$

In the above expression the azimuth of the array element is expressed as $\gamma_m = 2\pi m / M$, the elevation dependence is given by $\zeta = 2\pi\rho \cos(\vartheta_n) / \lambda$ and the autocorrelation function of the applied PN maximum length bit sequence $a(t)$ as $x(\tau)$. Further, $g(\zeta)$ is the voltage elevation pattern of the array elements, c_n and T_n are the complex amplitude and the relative delay of the nth incident wavefront respectively. The additive noise signal, whether sensed along with the incident wavefront or generated internal to the instrumentation, is represented as n_m. In vector notation, (3.1) can be rewritten as

$$\underline{y}(\tau) = [y_0(\tau), y_1(\tau), \ldots, y_{M-1}(\tau)]^T$$
$$= \sum_{n=1}^{N} \underline{u}(\theta_n) s_n(\tau) + \underline{\eta}(\tau), \tag{3.2}$$

where $s_n(\tau) = c_n g(\zeta) x(\tau\text{-}T_n)$,

$$\underline{u}(\theta) = [e^{j\zeta \cos(\varphi - \gamma_0)}, e^{j\zeta \cos(\varphi - \gamma_1)}, \ldots, e^{j\zeta \cos(\varphi - \gamma_{M-1})}]^T \tag{3.3}$$

represents the array steering vector in the direction $\theta = \{\vartheta, \varphi\}$, and

$$\underline{\eta}(\tau) = [\eta_0(\tau), \eta_1(\tau), \ldots, \eta_{M-1}(\tau)]^T \tag{3.4}$$

the noise signals at the array elements. In the above expressions the superscript ^{T} denotes transpose. In matrix notation 3.1 becomes

$$\begin{bmatrix} y_1 \\ y_2 \\ \vdots \\ y_M \end{bmatrix} = \begin{bmatrix} \underline{u}(\theta_1) & \underline{u}(\theta_2) & \cdots & \underline{u}(\theta_N) \end{bmatrix} \begin{bmatrix} s_1 \\ s_2 \\ \vdots \\ s_N \end{bmatrix} + \begin{bmatrix} \eta_1 \\ \eta_2 \\ \vdots \\ \eta_M \end{bmatrix}$$

or

$$\underline{y} = U(\theta)\underline{s} + \underline{\eta}. \tag{3.5}$$

The u_{ij} are known functions of the signal arrivals angles and the array element locations. In other words, u_{ij} depends on the ith array element, its position relative to the origin of the co-ordinate system, and its response to a signal incident from the direction of the jth signal. The jth column of U is a steering vector $\underline{u}(\theta_j)$ of response to the direction of arrival θ_j of the jth signal. In geometrical language, the measured $\underline{y}$ vector can be visualised as a vector in M-dimensional space. The M-dimensional space can be divided into two subspaces, the signal subspace and the noise subspace. If U has two columns, the signal subspace is no more than a two dimensional subspace within the M-dimensional space containing two steering vectors, i.e. two incident wavefronts. The continuum of all possible vectors, $\underline{u}(\theta)$, lies within the M-dimensional space. To visualise this, see Figure 3.2.
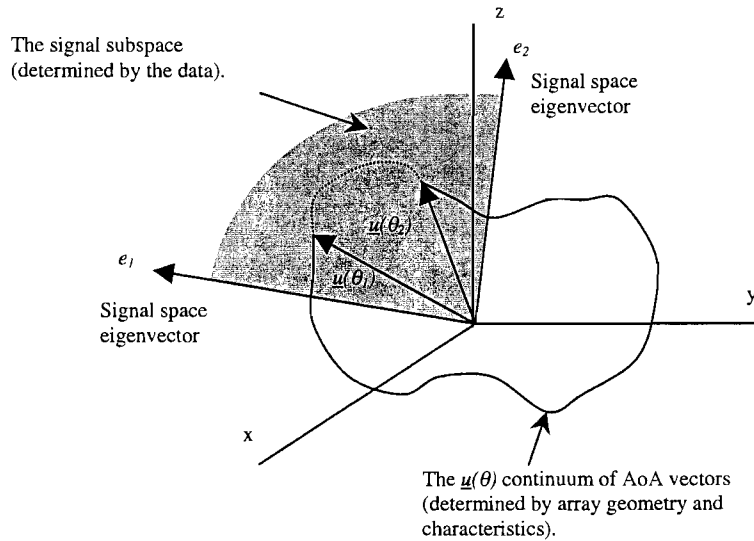
Figure 3.2: Geometric representation of a three array antenna.

Figure 3.2 shows the geometrical representation of an antenna consisting of three array elements and receiving two incident wavefronts given by the mode vectors $\underline{u}(\theta_1)$ and $\underline{u}(\theta_2)$. An example for azimuth-only direction finding system is shown, to extent this to an azimuth/elevation/range system θ must be written as $\theta = \{\vartheta, \varphi, r\}$. The $\underline{u}(\theta)$ is a vector continuum such as a snake (azimuth only) or a sheet (azimuth/ elevation) twisting and winding through the M-space. The $\underline{u}(\theta)$ continuum is determined by the array geometry and characteristics, the signal subspace by the data. In these geometrical terms (Figure 3.2), the problem of solving the AoA of multiple incident wavefronts consists of locating the intersections of the $\underline{u}(\theta)$ continuum with the signal subspace. When the number of incident wavefronts exceeds the number of array elements, the AoA can not be determined anymore. In that case the dimension of the $\underline{u}(\theta)$ continuum will be smaller that the dimension of the signal subspace, so the $\underline{u}(\theta)$ continuum will not intersect with the signal subspace.

3.2 Beamspace processing

For improved resolution the covariance matrix is first transformed from element space to beamspace [18,19]. This transformation also leads to other advantages such as reduced computation, reduced sensitivity to system errors and reduced bias in the estimate of an AoA. The data will be processed in the spatial frequency domain, also referred to as phase mode excitation-based beamspace processing [18]. The elements of the steering vector $\underline{u}(\theta)$ can be thought of as samples of the continuous signal,

$$u(\gamma,\theta) = e^{j\zeta \cos(\varphi-\gamma)}$$

(3.6)

which is periodic in γ with period 2π and can therefore be represented by the Fourier series

$$u(\gamma,\theta) = \sum_{h=-\infty}^{\infty} j^{|h|} a_h(\theta) e^{-jh\gamma} ,$$

$$a_h(\theta) = \frac{1}{2\pi j^{|h|}} \int_0^{2\pi} u(\gamma,\theta) e^{jh\gamma} d\gamma = J_{|h|}(\zeta) e^{jh\varphi} .$$

(3.7)

In the above expression $J_h(.)$ denotes the Bessel function of the first kind of order h. As can be seen, the spectral width of $u(\gamma,\theta)$ is infinite but the magnitudes of the Fourier coefficients decrease fast for $|h| > \zeta$, and are bounded by [20]

$$\left|J_{|h|}(\zeta)\right| \leq \left(\frac{\zeta e}{2|h|}\right)^{|h|} \leq \left(\frac{\pi\rho e}{\lambda|h|}\right)^{|h|}, \quad h \neq 0. \tag{3.8}$$

Here, e denotes the Euler number. The $a_h(\theta)$ coefficients become negligibly small for sufficiently large $|h|$, $|h| > \pi\rho e/\lambda$. To avoid aliasing, the number of array elements (sample frequency) must satisfy $M > 2\pi\rho e/\lambda$. Ignoring the small coefficients results in a series of $2*H$ coefficients $a_h(\theta)$ where $-H \leq h \leq H$ with $H = \lfloor \pi\rho e/\lambda \rfloor$. Here $\lfloor . \rfloor$ is the largest integer smaller than the argument. In the experimental set-up ($M = 157$, $\rho = 0.30$ m, $\lambda = 0.16$ m) the above condition is well satisfied. Let us define a unit-norm vector,

$$\underline{a}(\theta) = \left[a_{-H}(\theta),\ldots,a_0(\theta),\ldots,a_H(\theta)\right]^T \right] \tag{3.9}$$

which can be directly obtained from $\underline{u}(\theta)$ by the transformation

$$\underline{a}(\theta) = \frac{1}{\sqrt{M}} CV\underline{u}(\theta). \tag{3.10}$$

In the above transformation,

$$C = diag\left\{j^{-H},\ldots,j^0,\ldots,j^H\right\},$$

$$V = \frac{1}{\sqrt{M}}[\underline{v}_0,\underline{v}_1,\ldots,\underline{v}_{M-1}],$$

$$\underline{v}_m = [\omega^{-mH},\ldots,\omega^0,\ldots,\omega^{mH}]^T, \tag{3.11}$$

and $\omega = \exp(j2\pi/M)$, which is based on the $(2H+1) \times M$ submatrix of the spatial Fourier transform [18,21]. Multiplication of (3.5) by the matrix CV results in

$$\underline{z} = A(\theta)\underline{s} + \underline{n}, \tag{3.12}$$

where

$$A(\theta) = \sqrt{M}\left[\underline{a}(\theta_1),\underline{a}(\theta_2),\ldots,\underline{a}(\theta_N)\right],$$

$$\underline{n}(\tau) = CV\underline{\eta}. \tag{3.13}$$

The beam-space steering vector $\underline{a}(\theta)$ is centro-Hermitian. A complex vector $\underline{a}$ is defined to be centro-Hermitian if it satisfies $J\underline{a} = \underline{a}^*$, where J is the reverse permutation matrix. This property can be used to employ forward/ backward averaging, which will be explained in paragraph 3.4.

3.3 UCA-MUSIC

The eigenstructure of the beamspace array output is the basis for the UCA-MUSIC algorithm [17,19]. The covariance matrix is given by

$$R = E[\underline{z}\,\underline{z}^h] = AE[\underline{s}\,\underline{s}^h]A^h + E[\underline{n}\,\underline{n}^h]$$

or

$$R = ASA^h + \lambda R_0,$$ (3.14)

under the basic assumption that the noise and the incident wavefronts are uncorrelated, where $S = E[\underline{s}\,\underline{s}^h]$. The superscript ^{h} denotes Hermitian transposition (i.e. the operation of transposition with complex conjugation). In the special case wherein the elements of the noise vector $\underline{n}$ have mean zero and variance σ^2, λR_0 can be written as $\sigma^2 I$. If the number of incident wavefronts N is less than the number of array elements M, ASA^h becomes singular, because it has a rank less than M. Therefore

$$\left| AE[\underline{s}\,\underline{s}^h]A^h \right| = \left| R - \lambda R_0 \right| = 0.$$ (3.15)

This equation is only satisfied with λ equal to one of the eigenvalues of R. In theory the eigenvalues of signal vectors and the noise vectors can be easily distinguished. In practice however, there is not such a clear difference between the eigenvalues of the signal and the noise vectors, because of the finite data. Therefore, UCA-MUSIC needs to know a priori how many incident wavefronts (N) arrive at the antenna, which is calculated by another algorithm [21]. Now the eigenvectors associated with the $M - N$ smallest eigenvalues, λ_{min}, can be calculated, and are called the noise eigenvalues. Equation (3.14) can be rewritten to

$$R = ASA^h + \lambda_{min} R_0.$$ (3.16)

The M eigenvectors of R must satisfy

$$R e_i = \lambda_i R_0 e_i, \quad i = 1,2,\cdots,M.$$ (3.17)

Substituted in equation (3.14) we have

$$ASA^h e_i = (\lambda_i - \lambda_{min}) R_0 e_i.$$ (3.18)

Clearly, for each of the λ_i that is equal to λ_{min} we must have $ASA^h e_i = 0$ or $A \times e_i = 0$. That is, the eigenvectors associated with λ (R,R_0) are orthogonal to the space spanned by the columns of A. So now we can define the noise space as the $(M$-$N)$-dimensional subspace spanned by the M-N noise vectors and the signal subspace as the N-dimensional subspace spanned by the N incident signal mode vectors.

We now have the means to solve the AoA. If E_N is defined to be the $M \times N$ matrix whose columns are the N noise eigenvectors, then the ordinary Euclidean distance from the steering vector $\underline{a}(\theta)$ to the signal subspace is $d = \left| E_N^h \underline{a}(\theta) \right|$. We can plot d for points along the $\underline{a}(\theta)$ continuum as a function of θ, to form a null spectrum.

That is ,

$$Q(\theta) = \underline{a}^h(\theta) E_N E_N^h \underline{a}(\theta).$$ (3.19)
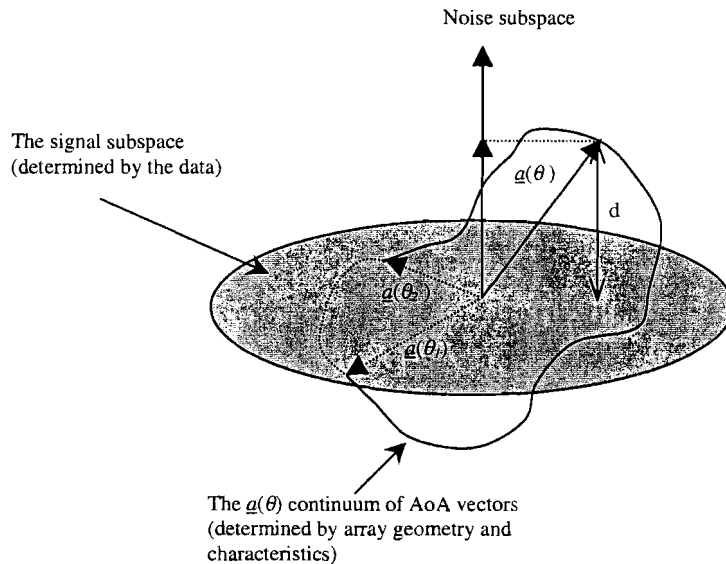
To illustrate this see Figure 3.3.

Figure 3.3: Geometric representation of a three array antenna.

Again we have a three-array antenna with two incident wavefronts, so the dimension of the signal space is two and the dimension of the noise space is one. As you can see in Figure 3.3 the Euclidean distance of the vector $\underline{a}(\theta)$ is the projection of the vector to the noise subspace. The Euclidean distance becomes zero when the $\underline{a}(\theta)$ vector intersects with the signal subspace, i.e. an AoA. This will result in a large peak in the null spectrum.

3.4   Forward/ backward averaging

Perfect correlation of signals may exist when two or more multipaths have exactly the same delay. This correlation tends to reduce the rank of the source covariance matrix, making it singular. Superresolution algorithms such as UCA-MUSIC fail when the source covariance matrix becomes singular. Averaging the covariance matrix over a number of snapshots removes the perfect correlation between two multipath signals with exactly the same delay. Although the perfect correlation is removed the signals are still strongly correlated. Because of this strong correlation the algorithm will be less accurate. To reduce this strong correlation spatial smoothing [22] can be used.

Spatial smoothing decorrelates the correlated signal by subdividing the array into a number of smaller overlapping subarrays and than averaging the array covariance matrix obtained from each subarray. The spatial smoothing methods using subarrays reduce the effective aperture of the array and hence the angular resolution and estimation accuracy. To overcome this problem an improved spatial smoothing method, forward/ backward (FB) averaging [18,21] is used to reduce the correlation. FB averaging exploits the centro-Hermitian property of the beamspace array steering vector $\underline{a}(\theta)$.

The FB averaged matrix is given by

$$\tilde{R} = \frac{1}{2}\left(R + JR^*J\right) = A\tilde{S}A^h + \lambda_{min}R_0,\tag{3.20}$$

where

$$\tilde{S} = (S + S^*)/2\tag{3.21}$$

is the FB averaged signal covariance matrix. The superscript * denotes complex conjugate. The FB averaging improves the conditions of the array output covariance matrix, it decorrelates strongly correlated signals and consequently improves the performance of the UCA-MUSIC algorithm.

3.5   Effects of finite data

The eigenvectors of the true covariance data can be easily divided into a set of small eigenvectors and a set of bigger eigenvectors, which are the noise eigenvectors and the signal eigenvectors, respectively. In our measurement, the covariance matrix is estimated from a finite number of beamspace snapshots $z(\tau_k)$, $k = 1,2,\ldots,K$. The estimated covariance therefore differs from the true covariance matrix The resulting covariance matrix is given by

$$\hat{R} = \frac{1}{2K}\sum_{k=1}^{K}\left(\underline{z}(\tau_k)\underline{z}^h(\tau_k) + J\underline{z}^*(\tau_k)\underline{z}^T(\tau_k)J\right).\tag{3.22}$$

As a result of this there is not such a clear discrepancy between the noise eigenvectors and the signal eigenvectors. In order to determine the dimension of the noise subspace, i.e. the number of noise eigenvectors, an algorithm is used to estimate this dimension. This algorithm is a modified version of Akaike's information criterion [21], which operates on the FB averaged covariance matrix. Because of the estimated covariance matrix the null spectrum will also differ from the true null spectrum. The estimated null spectrum is given by

$$\hat{Q}(\theta) = \underline{a}^h(\theta)\hat{E}_N\hat{E}_N^h\underline{a}(\theta).\tag{3.23}$$

The AoA estimates are obtained by searching the N deepest nulls. The estimated covariance matrix causes a perturbation of the estimated null spectrum from the true null spectrum. This perturbation causes errors in the AoA estimates and limits the capability to discriminate between closely spaced sources.

Chapter 4

Measurement results

The experimental set-up was used to measure the transmission of radio waves through buildings. The transmitting antenna was placed at one side of the building and the receiving antenna at the other side. In theory we are looking for a building standing alone on an infinitely extended area, so the CIR of the channel is completely determined by the building under test. In practice however this is impossible to achieve; therefore, some compromises had to be made. Two buildings at Eindhoven University of Technology precinct were found to be suitable for the transmission measurements. The first building is the Traverse Building with a large open area behind the building and a large square in front of the building to place the antennas. When placing the transmitting antenna on the Laplace square the Traverse Building can be directly illuminated, except for a small part of the building which is shadowed by the Laplace Building as can be seen on the map given in Figure 4.1. The second building is the PABO Building with a large open area in front of the building and a street behind the building to place the antennas (see Figure 4.5).

4.1   Representation of the measurement results

For every building and the built-up environment a map is given indicating the positions of the transmitting antenna (Tx) and receiving antenna (Rx). At every combination of transmitting and receiving antenna the CIR of the radio channel was measured and stored on the hard disk. At exactly the same position as the receiving antenna a panorama picture was taken to give an overview of the built-up environment. The algorithm UCA-MUSIC was used to calculate the AoA of the incident rays. The μFiPre model was used to visualise the possible rays from transmitting antenna to receiving antenna and their corresponding delay times. For each measurement location, the appendices provide a figure (a) with a map of the built-up environment containing the 15 strongest rays predicted by the μFiPre model.   In figure (b) the measured CIR is compared with the predicted CIR (plotted in solid grey), where we are only interested in the absolute delay times. Further, the appendices provide a figure (c) with the AoA as a function of the elevation angle, a figure (d) with a panorama photo of the built-up environment, a figure (e) with the CIR of the radio channel under test and a figure (f) with the AoA as a function of the delay time. In the figures containing the AoA information, the incident rays are represented as bullets. The size of the bullets corresponds to the respective signal strengths relative to the total received power. The AoA figures contain the incident waves, which are less than 30 dB weaker than the total received power in case of the Traverse Building and less than 40 dB weaker in case of the PABO Building. These figures also

contain light grey zones and a dark grey zone. The dark grey zone indicates in which azimuth and elevation angle the building under test is visible. The light grey zone indicates the reflection surfaces, seen by both the transmitting and receiving antenna, of the surrounding buildings. A dashed, vertical line indicates the azimuth angle of the transmitting antenna. The starting position of the receiving antenna corresponds to $0°$ azimuth angle. The transmitting antenna was placed at a height of 6.5 meter and the receiving antenna at a height of 2.4 meter to simulate a typical microcell situation.

4.2 Traverse Building

A map of the Traverse Building and the built-up environment is given in Figure 4.1. The transmitting antenna is placed at two different positions Tx1 and Tx2, illuminating the building directly with the only single reflection originating from the Laplace Building. The receiving antenna is placed at three different positions (Rx1, Rx2, and Rx3) behind the building for AoA measurements.
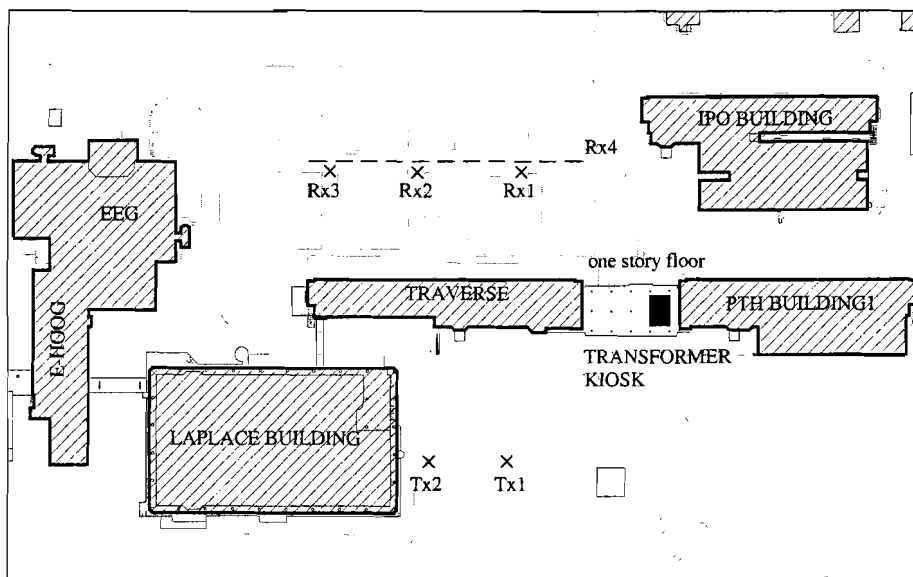
Figure 4.1: Map of Traverse Building and built-up environment.

4.2.1 AoA measurements

A note should be made about the way the μFiPre model was used. From Figure 4.1 it can be seen that the Traverse Building is connected with the PTH Building with a one-story floor which is located above a road. Beneath this floor there is a transformer kiosk. From the measurement results in paragraph 4.2.2 it will become clear that we have two important contributions to the total field coming from the PTH Building and transformer kiosk. When we use the 2D-μFiPre model containing the PTH Building and transformer kiosk, the reflection and/ or diffraction from the PTH Building becomes invisible for the model. An other important contribution to the total field is reflection/ diffraction coming from the E-hoog Building, which will be blocked by the Laplace Building and the EEG Building in a 2D environment. Therefore the μFiPre model was used two times for every measurement location. First with an actually 2D-environment of the measurement location. Secondly, with the transformer kiosk and without the Laplace and EEG Building, were only the reflected and/ or diffracted rays from the transformer kiosk and E-hoog Building were taken into

account. The predicted rays of the µFiPre model are plotted in the appendices. The surrounding buildings are plotted in dark grey the transformer kiosk, Laplace Building and EEG Building in light grey. Because of the height differences, the rays plotted through the light grey buildings are actually rays going over these buildings (see the figures (a) in the appendices A and B). The absolute power of the predicted CIR differs with the measured CIR, which is probably the result of the one-story floor that is not included in the µFiPre model. The absolute power of the reflected/ diffracted rays coming from the E-hoog Building differ from the predicted rays, which is most likely the result of the partial blockage by the Laplace Building.

Tx1-Rx1

The resolved rays that correspond to the first peak of the measured CIR are plotted in the dark grey zone and are therefore the result of transmission through the Traverse Building. When we compare the predicted and measured CIR we notice that the transmission peak is missing from the predicted CIR. The first peak in the predicted CIR is the result of reflection/ diffraction at the transformer kiosk; the second peak is the result of reflection/ diffraction at the PTH Building. These results could also be seen in the AoA figures and the measured CIR. From the measured CIR it can be seen that the transmission is only 8 dB weaker than the strongest peak and is therefore an important contribution to the received field. The received field caused by the transmission is the contribution of many incident rays coming from different parts of the building, whereby the strongest contribution arrives from the direction of the transmitting antenna. In this situation the incident angle of the shadowed line of sight (LOS) is almost perpendicular to the building surface, resulting in a maximum value of the transmission coefficient (the transmission coefficient will be explained in Chapter 5).

Tx2-Rx1

The receiving antenna is kept at the same position while the transmitting antenna is moved from Tx1 to Tx2. The incidence angle of the transmitted ray path is smaller ($\approx 63°$) compared to the previous situation, making the transmission coefficient smaller. The smaller incident angle will also increase the pathlength (internal pathlength) of the transmitted ray path through the building; therefore it is likely to expect that more obstacles will arise on the path depending on the internal structure and furniture. The combination of the smaller transmission coefficient and the internal structure results in a 12 dB weaker transmission compared to the previous situation. Although the transmission is weaker, the transmission still is an important mechanism of propagation as can be seen in the measured CIR. The rays with an elevation higher than the building rooftop could be the result of diffraction from obstacles in the neighbourhood of the receiving antenna or ground reflection. The predicted CIR shows again reflection/ diffraction at the PTH Building and transformer kiosk.

Tx2-Rx2

This situation is comparable with Tx1-Rx1, whereby the incident angle of the transmitted ray path is again almost perpendicular to the building surface. Although the power in the transmission peak is almost the same as the power in the Tx1-Rx1 situation, the power in the second peak has decreased significantly making the transmission the prime propagation mechanism. The strongest contribution of the transmission is coming from the direction of the transmitting antenna. The three strongest peaks in the predicted CIR are the results of reflection/ diffraction at the transformer kiosk, reflection/ diffraction at the PTH Building and

diffraction at the IPO Building, respectively. These results could also be seen in the AoA figures and measured CIR. Except for the diffraction at the IPO Building, because the resolved rays corresponding to this diffraction are more than 30 dB below the average power.

Tx1-Rx2

When looking at the measured CIR we notice besides the transmission and transformer kiosk reflection/ diffraction peak a third important peak. This peak is the result of reflection at the E-hoog Building. Because of the 2D nature of µFiPre it is impossible to deal with different building heights, therefore the E-hoog reflection is not predicted in the model. The incident angle of the transmitted ray path on the building surface is about 78°, resulting in a decreasing transmission coefficient and an increasing internal pathlength compared to the previous situation. Therefore the power of the transmission peak is about 16 dB weaker. The power in the second peak of the measured CIR is smaller compared to the previous situation, although the pathlength corresponding to this peak is smaller. This may be the result of attenuation due to the tree at 190°. In this measurement situation the transmission is again one of the most important mechanisms of propagation.

Tx1 – Rx3

As can be seen from the measured CIR the transmission is a very important mechanism of propagation. When we look at the AoA figure we see a lot of power coming from the right side of the building, which is not predicted by the model. This power is probably the result of a carport like structure standing on this side of the building. An other important contribution is the reflection at the E-hoog Building. The rays at 100° are probably the result of tree scattering.

Tx2 – Rx3

As in all the previous measurements we see that transmission is an important mechanism of propagation. From the predictions and measurements it can be seen that the reflection/ diffraction from the transformer kiosk and PTH Building is stronger than in the previous situation. On the other hand the power coming from the right side of the building and the reflection at the E-hoog Building is weaker than in the previous situation. This is the result of the geographic position of the Laplace Building. Where in this case the Laplace Building blocks most of the possible rays coming from the right side of the building.

With each AoA measurement we can only determine the electromagnetic fieldstrength for one position behind the building. As we are interested in the total electromagnetic field distribution behind the building we should perform an infinite number of AoA measurements, which are complex and time consuming. To overcome this problem we developed a new measurement method, which will be explained in the next paragraph.

4.2.2 Fieldstrength measurement

The vehicle with the antenna mounted on the roof was driven with constant speed along the dotted line behind the building (Rx4, in Figure 4.1). At every 0.1s a CIR was measured and stored on the hard disk. For both positions of the transmitting antenna these measurements were conducted. Figure 4.2 shows the measurements results of Tx1 – Rx4, the CIR are placed next to each other along the vertical axis with the power density indicated by a particular

colour. The vertical axis represents the delay time in μs, i.e. the time in which the radio wave travels from the transmitting antenna to the receiving antenna. The horizontal axis represents the distance D travelled by the vehicle in meters, i.e. the building length. Beneath the CIR the Traverse Building and the transmitting antenna are shown to give a clear overview of the measurement situation. From the AoA measurements it is clear that the electromagnetic field is mainly determined by transmission through the building, and multipath contributions originating from the right and left side of the building. These contributions can be easily distinguished from Figure 4.2. As the vehicle starts driving with constant speed, the pathlengths of the multipath contributions originating from the left side of the building become longer resulting in longer delays times. These contributions appear as patterns with a positive slope in Figure 4.2. On the other hand the pathlengths of the multipath contributions originating from the right side of the building become shorter resulting in shorter delays times, which appear as patterns with a negative slope.
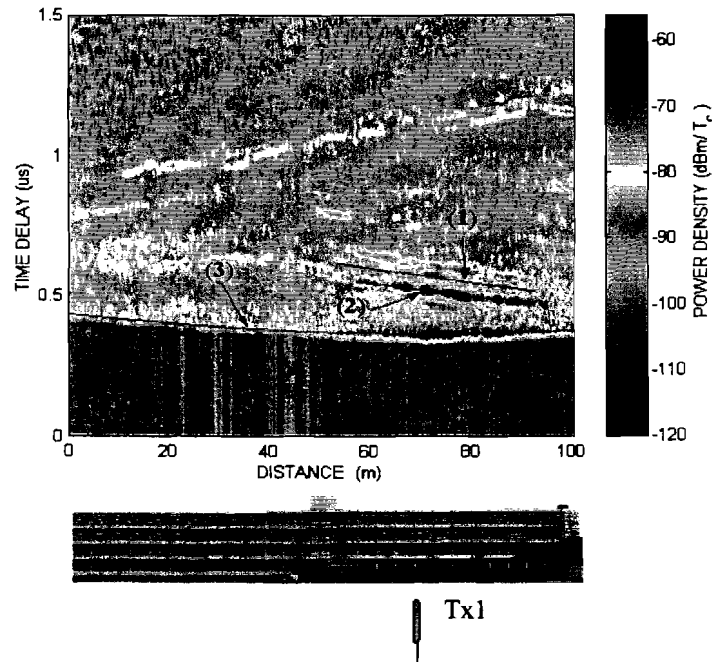
Figure 4.2 : Measurement results of Tx1 – Rx4.

In Figure 4.2 three theoretical lines are plotted which represent the pathlengths expressed in terms of delay time of certain multipath contributions. The first line (1) represents reflection at the PTH Building and the second line (2) reflection at the transformer kiosk. The third line (3) represents the shortest distance d between the transmitting and receiving antenna in terms of delay time. This shortest distance equals the pathlength of transmission, therefore the pattern with the flat hyperbolic shape is the result of transmission of radio waves through the building.

4.2.3   Measured building transmission loss

Link budget

At every position behind the building the received transmission power can be expressed as

$$P_{re} = \frac{P_{tr} G_{tr} G_{re}}{L_{tr} L_{re} L_b} \left(\frac{\lambda}{4\pi d} \right)^2 \qquad\qquad (4.1)$$

or

$$P_{re} = P_{tr} + G_{tr} + G_{re} - L_{tr} - L_{re} - L_{b} - L_{fs} \quad dBm, \tag{4.2}$$

where

P_{re} = received power in dBm

P_{tr} = transmitted power in dBm

G_{tr} = gain of transmit antenna in dBi

G_{re} = gain of receive antenna in dBi

L_{tr} = transmitter cable losses in dB

L_{re} = receiver cable losses in dB

L_{b} = building transmission loss in dB

L_{fs} = free-space loss in dB

In equation (4.2) the free-space loss L_{fs} is given by

$$L_{fs} = 20 \log \left(\frac{4 \pi d}{\lambda} \right) \quad dB, \tag{4.3}$$

where d is the distance between the transmit and receive position and λ the wavelength, both in m. In Table 4.1 the link budget is given

Transmit power P_{tr} (+)	27	dBm
Gain of transmit antenna G_{tr} (+)	12	dBi
Cable losses transmitter L_{tr} (-)	1.3	dB
Gain of receiving antenna G_{re} (+)	2	dBi
Cable losses receiver L_{re} (-)	5.13	dB
Max free-space loss L_{fs} (-)	80.4	dB

Table 4.1: Link budget.

The free-space loss in Table 4.1 is a function of the distance d, the maximum value corresponds therefore with the maximum distance d in the Tx1 − Rx4 situation. The received power signal consists of slow variations burdened with fast fluctuations, which are respectively lognormal and Rayleigh distributed. The lognormal fading can be obtained by spatial averaging (40 λ window) as will be explained in the next section. Figure 4.3 shows the building transmission loss L_{b}.
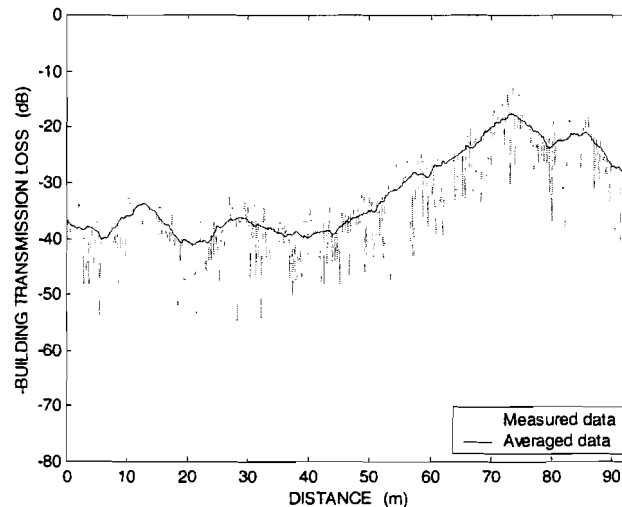
Figure 4.3: Tx1 − Rx4 measured building transmission loss.

At a distance D of 71.22 meter the transmitted ray path is perpendicular to the building surface. The smallest building transmission loss corresponds to this position behind the building as can be seen from Figure 4.3. The measured building transmission loss in the Tx2 – Rx4 situation is plotted in Figure 6.5 were it will be compared with the transmission model explained in Chapter 5.

Spatial averaging

The received power signal $P_{re}(l)$ can be can be expressed as

$$P_{re}(l) = m(l)r_o(l).$$ (4.4)

The component $m(l)$ is called *local mean, long-term fading* or *lognormal fading*. The factor r_o is called *multipath fading, short-term fading* or *Rayleigh fading* and its variation is due to the waves reflected from the internal structure and furniture of the building. The *long-term fading* $m(l)$ can be obtained from

$$m(l_1) = \frac{1}{2L} \int_{l_1-L}^{l_1+L} r(l)dl.$$ (4.5)

According to [23] the length of $2L$ has been determined to be 40 wavelengths to smooth out Rayleigh fading. If the length $2L$ is shorter than 40 λ, the average output would still include a weaker portion of Rayleigh fading. If the length is greater than 40 λ, the excessive length of averaging also smoothes out the local-mean information. Using 36 up to 50 samples in an interval of 40 wavelengths is an adequate averaging process for obtaining the local means [24].

The vehicle in our experimental set-up drives with a constant speed of 1.44 m/s, the term 40 λ corresponds to 6.32 m and at every 0.1s a sample was taken. The number of samples within the 40 λ windows is approximately 44 and is therefore a suitable window for obtaining the local means.

The *short-term fading* can be obtained by

$$r_0(l) = \frac{P_{re}(l)}{m(l)}$$ (4.6)

and is Rayleigh distributed. The *short-term fading* component of P_{re} in case of the Tx1 – Rx4 measurement was obtained to verify whether the short-term fading is Rayleigh distributed. The cumulative distribution of this fading was compared with the theoretical Rayleigh cumulative distribution function (CDF),

$$F(r_0) = 1 - e^{(\frac{-r_o^2}{2K^2})}.$$ (4.7)

The relationship between the factor K in equation (4.7) and the mean of r_0 can be shown to be

$$K = \sqrt{\frac{2}{\pi}} E\{r_o\}.$$ (4.8)

Figure 4.4 shows the comparison of the theoretical Rayleigh CDF and experimental CDF.
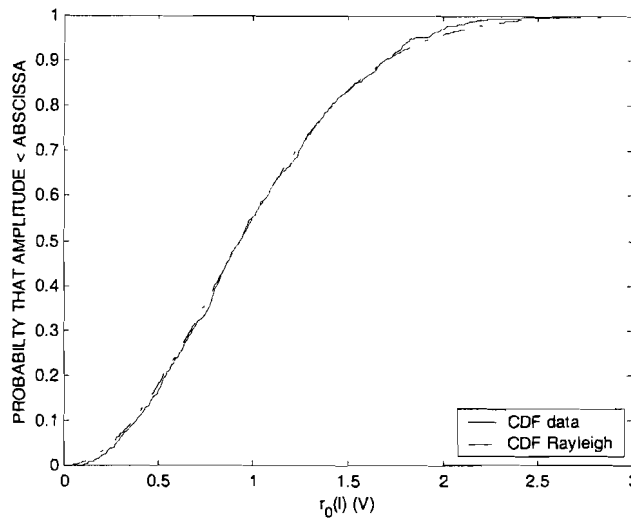
Figure 4.4: Comparison of the theoretical Rayleigh and experimental CDF.

From Figure 4.4 it can be seen that the probability distribution of the *short-term fading* component is very well approximated by the Rayleigh distribution. This implies that a 40 λ averaging window is an adequate window for obtaining the *long-term fading*.

4.3 PABO Building

A map of the PABO Building and the built-up environment is given in Figure 4.5. The transmitting antenna is placed at four different positions Tx1, Tx2, Tx3 and Tx4, illuminating the PABO Building uniformly. The receiving antenna is placed at three different positions (Rx1, Rx2, and Rx3) behind the building for AoA measurements.
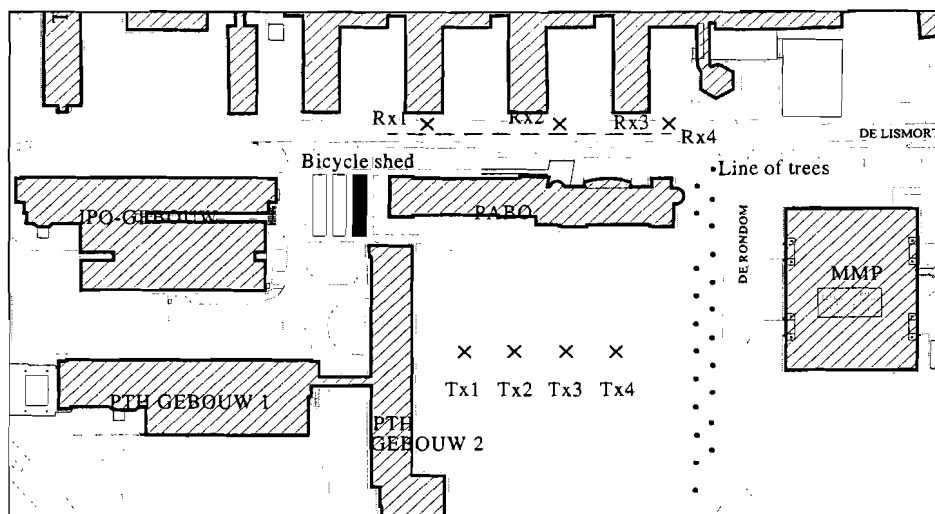
Figure 4.5 : Map of PABO Building and built-up environment.

4.3.1 AoA measurements

From the measurement results in paragraph 4.3.3 we will see two important contributions coming from the IPO Building and the bicycle shed. Because of the 2D nature of μFiPre it is impossible to predict these two contributions. Therefore the μFiPre model was used twice for every measurement location. First without and secondly with the bicycle shed where only the reflected and/ or diffracted rays from this shed were taken into account. The predicted rays of the μFiPre model are plotted in the appendices. The surrounding buildings are plotted in dark grey and the bicycle shed in light grey. The bicycle shed and IPO Building differ in height, therefore the rays plotted through the bicycle shed are actually rays going over the bicycle shed.

Tx1-Rx1

The power in the first peak of the measured CIR is the result of transmission through the PABO Building, which is about 15 dB weaker than the strongest peak in the CIR. From the AoA figures it can be seen that a lot of power is coming from the right side of the building. Both the measurements and predictions show that this is the result of reflection/ diffraction at the IPO Building and bicycle shed. The first peak in the predicted CIR is the result of reflection at the bicycle shed and the third peak is the result of reflection/ diffraction at the IPO Building. When we look at the predicted rays we see some reflection/ diffraction at the MMP Building. This appears as the plotted rays coming from the left side of the building in the AoA figures.

Tx2 – Rx1

Although there is transmission through the building, the incident rays that correspond to this transmission are not depicted in the AoA figures. The transmission peak in the CIR is very small compared to the strongest peak and therefore the transmission is more than 40 dB below the total received power. In this case we have a very strong contribution of the reflection at the bicycle shed, which appears as the first peak in the predicted CIR. Finally we see some reflection at the IPO Building and Paviljoen.

Tx3 – Rx1

In this situation we see a small contribution of transmission to the total field. The incident wavefronts that correspond to the transmission arrive from the direction of the transmitting antenna. The first and second peak in the predicted CIR are the result of reflection/ diffraction at the bicycle shed and IPO Building respectively.

Tx4 – Rx1

Again we have a small contribution of transmission to the total field arriving from the direction of the transmitting antenna. The first peak in the predicted CIR is the result of diffraction (PABO Building) in combination with reflection (bicycle shed). The second peak is the result of diffraction (PTH Building) in combination with reflection (bicycle shed). The strongest peak in the measured CIR is the result of reflection at the IPO Building.

Tx1 – Rx2

In this case we have a strong contribution coming from the left side of the building, which is partly the result of reflection/ diffraction at the MMP Building. This result appears as the strongest peak in the predicted CIR. When we compare the predicted with the measured CIR we see besides the transmission some other peaks missing from the predictions. These peaks are the result of three scattering as will come clear in paragraph 4.3.3. Further we see a little transmission and some reflection at the IPO Building.

Tx2 – Rx2

Again we have a small transmission contribution. The rays coming from the right side of the building are the result of reflection/ diffraction at the IPO Building and bicycle shed. The rays coming from the left side are mainly the result of reflection/ diffraction at the MMP Building.

Tx3 – Rx2

Both the transmission and three scattering are missing from the predictions as can be seen from the predicted CIR. The first peak in the predicted CIR is the result of MMP reflection. From the measured CIR it can be seen that the power of the MMP reflection is about the same as the three scattering. We also see some reflection at the IPO Building, and a small contribution of transmission.

Tx4 – Rx2

The transmission and three scattering are again missing from the predictions. From both the measurements and predictions we see some reflection at the PABO Building. Further we have some MMP and IPO reflection and a small transmission.

Tx1 – Rx3, Tx2 – Rx3, Tx3 – Rx3, Tx4 – Rx3

For each of these four measurements we see a lot of power coming from the left side of the building. This is the result of the vegetation standing on this side of the building and MMP reflection. The measured CIR shows that the scattering at the vegetation is the most important contribution, i.e. the strongest peak. From the other side of the building we see a small contribution to the total field, which is the result of reflection/ diffraction at the IPO Building and the bicycle shed. Further we see little or no transmission. The transmission is more than 40 dB below the total received power and is therefore not depicted in the AoA figures.

4.3.2   Fieldstrength measurement

For each transmitting antenna position a fieldstrength measurement was conducted. Figure 4.6 shows the measurement results of Tx4 – Rx4. Beneath the CIR the PABO Building and the transmitting antenna are shown to give a clear overview of the measurement situation. From the photo it can be seen that the PABO Building is partly shadowed by the PTH Building. In Figure 4.6 five theoretical lines are plotted which represent the pathlengths expressed in terms of delay time of certain multipath contributions. The lines (1), (2), (3) and (4) represents respectively reflection at the IPO Building, reflection at the bicycle shed, reflection/ diffraction at the MMP Building and three scattering. The fifth line (5) represents the shortest distance d between the transmitting and receiving antenna in terms of delay time.

This shortest distance equals the pathlength of transmission, therefore the pattern with the flat parabolic shape is the result of transmission of radio waves through the building.
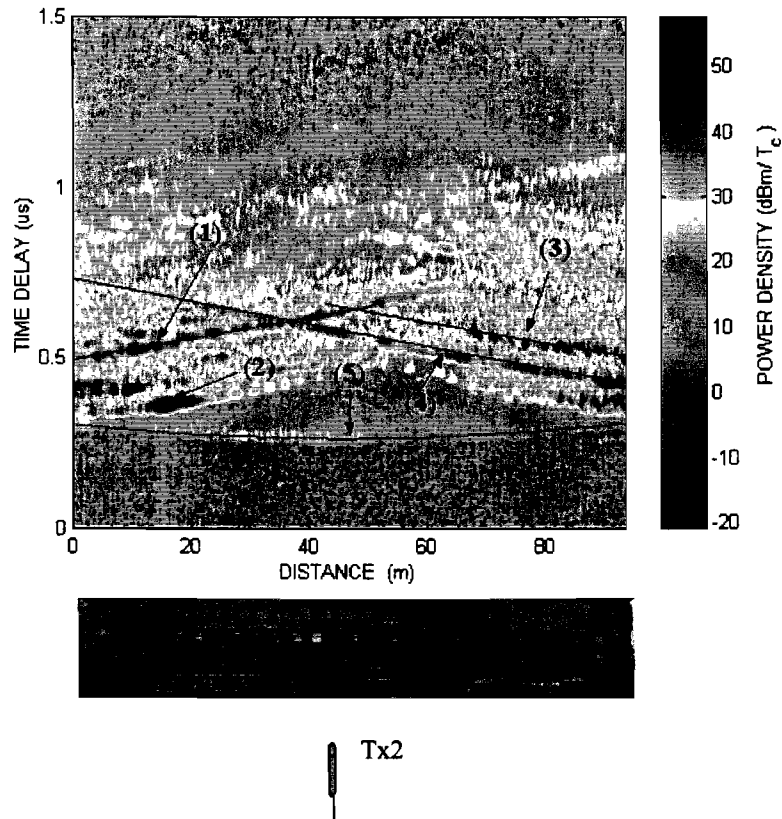
Figure 4.6: Measurement results of Tx2 – Rx4.

4.3.3   Measured building transmission loss

For the PABO Building the same link budget can be used as in paragraph 4.1.3, except for the maximum free-space loss. Figure 4.7 shows the building transmission loss in the Tx2 – Rx4 situation. The other transmission measurement results are given in Chapter 6.
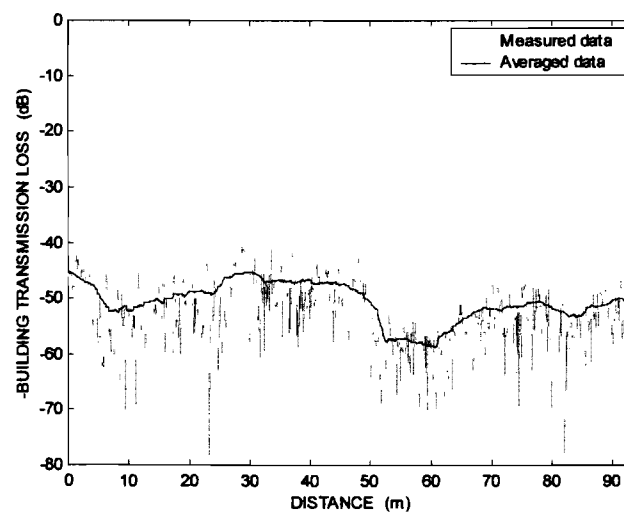
Figure 4.7: Tx2 – Rx4 measured building transmission loss.

4.4   Conclusions

From the AoA measurements we see that transmission is an important mechanisms of propagation. In some of the measurements transmission seems to be the prime mechanism of propagation. The fieldstrength measurement method, described in paragraph 4.2.2, provides an easy, fast an accurate way to measure the field due to transmission through buildings.

The incident angle on the building and the internal structure seems to be the two most important parameters by which the transmission is characterised. Further it can be seen that there is more transmission through the Traverse Building than through the PABO Building. This could be explained by the percentage of windows, which is larger for the Traverse Building .

Chapter 5

Basic transmission model

Most existing propagation prediction models model the buildings as being completely opaque to radio signals. From the previous measurement results and [2] we see that transmission is an important mechanism of propagation in a micro cell environment. Our goal is to improve the μFiPre model by including transmission through buildings.

5.1 Transmission coefficient

In our experimental set-up we assume that we have 2-D propagation and vertical polarisation. Therefore the electromagnetic field has a component parallel to the reflecting surfaces and the attenuation due to reflection is modelled by the soft Fresnel reflection coefficient

$$R_s(\theta) = \frac{\sin\theta - \sqrt{\varepsilon_r - \cos^2\theta}}{\sin\theta + \sqrt{\varepsilon_r - \cos^2\theta}} \ . \tag{5.1}$$

The incidence angle θ is the angle between the reflecting surface and the direction of the incident or reflecting ray. The quantity ε_r is called the relative complex permittivity and is modelled as

$$\varepsilon_r = \varepsilon_r' - j\varepsilon_r'' = \varepsilon_r'(1 - j\tan\delta) \ , \tag{5.2}$$

where ε_r' is the dielectric constant of the reflecting medium. The imaginary part ε_r'' incorporates all losses that occur in the material, and is called the relative loss factor. This relative loss factor divided by the real part of the permittivity is called the loss tangent of the material. The electrical parameters $\varepsilon_r' = 5.3$ and $tan\delta = 1.8 \ 10^{-4}$ are used in the μFiPre model. With these electrical parameters the relative complex permittivity is relatively large compared to the cosine term, therefore equation (5.1) can be rewritten as

$$R_s(\theta) = \frac{\sin\theta - \sqrt{\varepsilon_r}}{\sin\theta + \sqrt{\varepsilon_r}} \ . \tag{5.3}$$

This reflection coefficient is used in the μFiPre model; therefore we shall refer to this coefficient as being the μFiPre reflection coefficient. To indicate the minor difference between the Fresnel and μFiPre coefficient, the two coefficients are plotted in Figure 5.1.
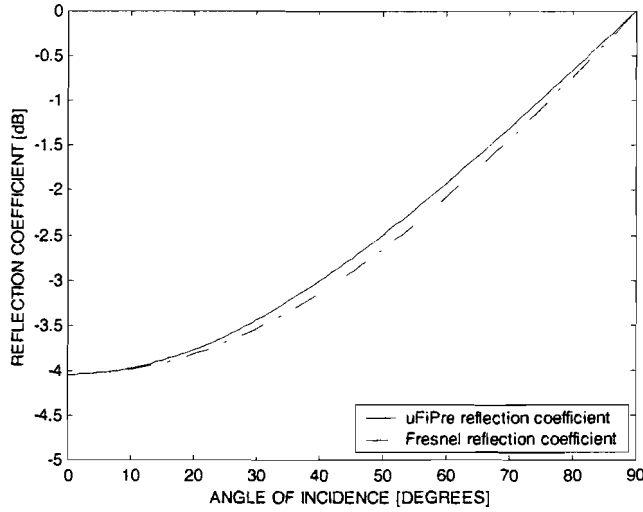
Figure 5.1: Comparison of Fresnel and μFiPre reflection coefficient.

The soft transmission coefficient can be derived from the soft reflection coefficient with the following expression

$$T_s(\theta) = 1 + R_s(\theta).$$ (5.4)

5.2 Basic transmission model

Some existing propagation models [25] use the following expression to calculate the path loss if the propagation path crosses N different areas,

$$L = \left(\frac{4\pi d_1}{\lambda}\right)^{\gamma_1} \left(\frac{d_2}{d_1}\right)^{\gamma_2} \left(\frac{d_3}{d_2}\right)^{\gamma_3} \cdots \left(\frac{d_N}{d_{N-1}}\right)^{\gamma_N} \quad d_{N-1} \le d \le d_N,$$ (5.5)

where λ is the wavelength and γ is a factor which indicates how the received signal power varies as a function of the propagation path length d_{n-1} - d_n, $1 \le n \le N$. For free-space the factor γ equals 2. We model the transmission through a building as if it were a single transmitted ray directly from source through the building to the receiver, see Figure 5.2.
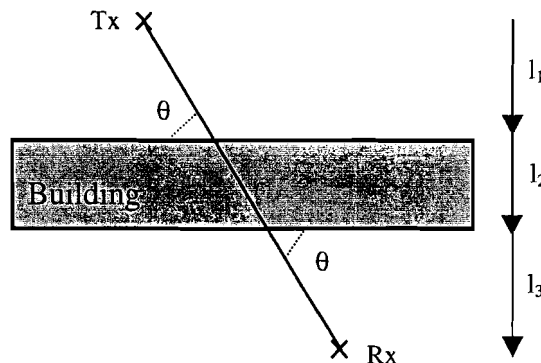
Figure 5.2: Plan view of building.

In our basic transmission model we have three different areas as can be seen from Figure 5.2. First from transmitter to building, through the building and from building to receiving antenna. The received signal power is then given by

$$P_{re} = A d_1^{-2} |T_{s1}(\theta)|^2 \left(\frac{d_2}{d_1}\right)^{-\gamma} |T_{s2}(\theta)|^2 \left(\frac{d_3}{d_2}\right)^{-2},$$

(5.6)

where $d_1 = l_1/\cos\theta$, $d_2 = l_2/\cos\theta$, $d_3 = l_3/\cos\theta$ and

$$A = \frac{P_{tr} G_{tr} G_{re}}{L_{tr} L_{re}} \left(\frac{\lambda}{4\pi}\right)^2.$$

(5.7)

In equation (5.7) L_{tr} represents the transmitter cable losses and L_{re} the receiver cable losses. The transmission coefficients $T_{s1}(\theta)$ and $T_{s2}(\theta)$ are used to determine the total amount of energy loss at the two interfaces between the building interior and free-space. Although the model given in equation (5.5) is used in the literature [25], the model fails when tested on reciprocity. The factor γ in equation (5.6) deals with the divergence of the radio wave and the attenuation caused by the internal path length. Therefore we can replace the term $\left(\dfrac{d_2}{d_1}\right)^{-\gamma}$ by

$$\left(\frac{d_2}{d_1}\right)^{-2} 10^{-\alpha d_{in}/10},$$

(5.8)

where α indicates a specific building loss in dB per meter and d_{in} the internal building pathlength $d_2 - d_1$. If we substitute equation (5.8) in (5.6) we have

$$P_{re} = A(d_1)^{-2} |T_{s1}(\theta)|^2 \left(\frac{d_2}{d_1}\right)^{-2} 10^{-\alpha d_{in}/10} |T_{s2}(\theta)|^2 \left(\frac{d_3}{d_2}\right)^{-2} = A |T_{s1}(\theta)|^2 (d_3)^{-2} |T_{s2}(\theta)|^2 10^{-\alpha d_{in}/10}.$$

(5.9)

If the two external walls are parallel spaced and made of the same materials the building transmission loss, defined as the loss relative to free-space can be written as

$$L_b = \alpha d_{in} - 40 \log |T_s(\theta)| \quad dB.$$

(5.10)

where $T_{s1}(\theta) = T_{s2}(\theta) = T_s(\theta)$. In equation (5.10) α incorporates the remaining losses due to the external walls and obstructions inside the building.

5.3   Verification of µFiPre's dielectric constant

The dielectric constant used in the µFiPre model for buildings is that of brick with a relative humidity of 5% ($\varepsilon_r' = 5.3$). To verify this dielectric constant we performed some

measurements at the PABO Building. The measurement situation is shown in Figure 5.3. To calculate the power due to reflection at the PABO Building we used the following expression

$$P_{re} = |R_s(\theta)|^2 \frac{P_{tr}G_{tr}G_{re}}{L_{tr}L_{re}} \left(\frac{\lambda}{4\pi d}\right)^2 , \qquad\qquad (5.11)$$

were $d = d_1 + d_2$.
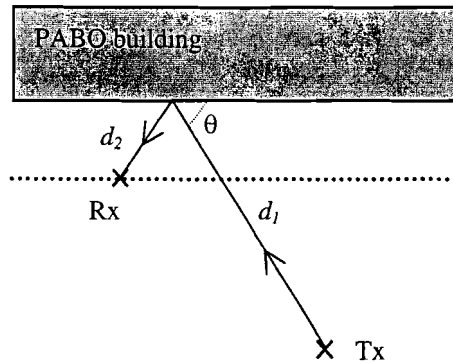
Figure 5.3: PABO reflection measurement.

The power due to reflection was measured along the dotted line in Figure 5.3. The measured reflection loss compared to the theoretical reflection loss is given in Figure 5.4. For the theoretical reflection loss we use the µFiPre reflection coefficient with the electrical parameters $\varepsilon_r' = 5.3$ and $tan\delta = 1.8 \ 10^{-4}$.
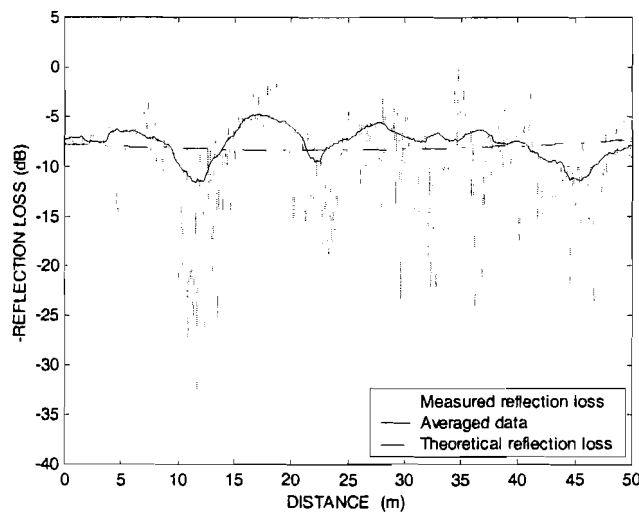
Figure 5.4: Comparison of measured reflection loss with theoretical reflection loss.

The theoretical reflection loss assumes a flat surface and constant dielectric properties of the surface, in practice we have a rough surface that explains the differences in Figure 5.4. In the next chapter the basic transmission model is compared with the measurements results obtained at the PABO Building and Traverse Building.

Chapter 6

Comparison of basic transmission model with measurements

This chapter compares the basic transmission model explained in Chapter 5 with the measurements. Possible differences of this comparison will be explained by looking at the internal structures of the two buildings.

6.1 Prediction error

We use the specific building loss coefficient that corresponds to the smallest rms value of the prediction error. The prediction error was obtained by subtracting the predicted building transmission loss ($\hat{L}_b$) from the measured building transmission loss (L_b). The rms value of the prediction error is calculated with

$$e_{rms} = \sqrt{\frac{1}{n}\sum_{j=1}^{n}(\hat{L}_{b,j} - L_{b,j})^2} \;. \tag{6.1}$$

Further for every measurement path the mean and standard deviation of the prediction error were calculated with

$$\mu = \frac{1}{n}\sum_{j=1}^{n}(\hat{L}_{b,j} - L_{b,j}) \tag{6.2}$$

and

$$\sigma = \sqrt{\frac{1}{n-1}\sum_{j=1}^{n}((\hat{L}_{b,j} - L_{b,j}) - \mu)^2} \;, \tag{6.3}$$

respectively. In the above equations n is the number of samples taken over the measurement path.

6.2   PABO Building

We performed four measurements, which are compared with the basic transmission model in the case of the PABO Building. Figure 6.1 shows the comparison of the basic transmission model with the measured building transmission loss in the Tx1 – Rx4 situation. For this measurement situation we have a mean error of 0.11 dB, a standard deviation of 2.83 dB and a specific building loss coefficient of 2.85 dB/m. The measured building transmission loss is well predicted by the basic transmission model.
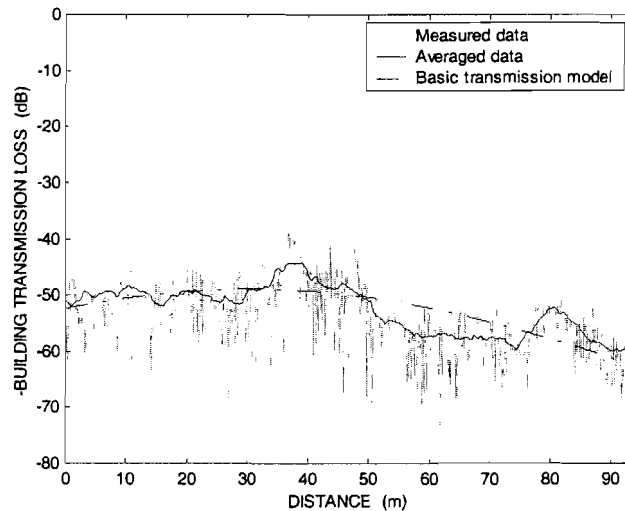
Figure 6.1: Comparison of Tx1-Rx4 measured building transmission loss with basic transmission model.

The comparison of the measured building transmission loss with the basic transmission model in the Tx2 – Rx4 situation is shown in Figure 6.2. In this measurement situation we have a mean error of 0.11 dB, a standard deviation of 4.27 dB and a specific building loss coefficient of 2.84 dB/m.
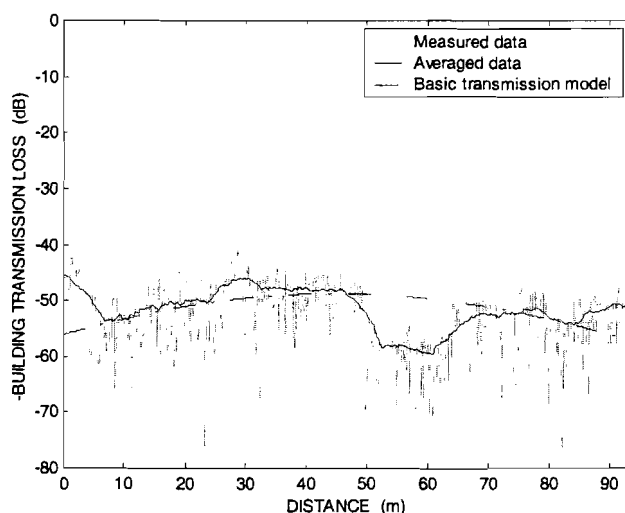
Figure 6.2: Comparison of Tx2 - Rx4 measured building transmission loss with basic transmission model.

At an interval of 50m to 60m on the Rx4 path we see that the basic transmission model predicts a smaller building transmission loss than the measured building transmission loss. At the corresponding interval at the PABO Building we notice an elevator shaft and a stairwell, which explains the large building transmission loss.

Figure 6.3 shows the comparison of the measured building transmission loss with the basic transmission model in the Tx3 – Rx4 measurement situation.
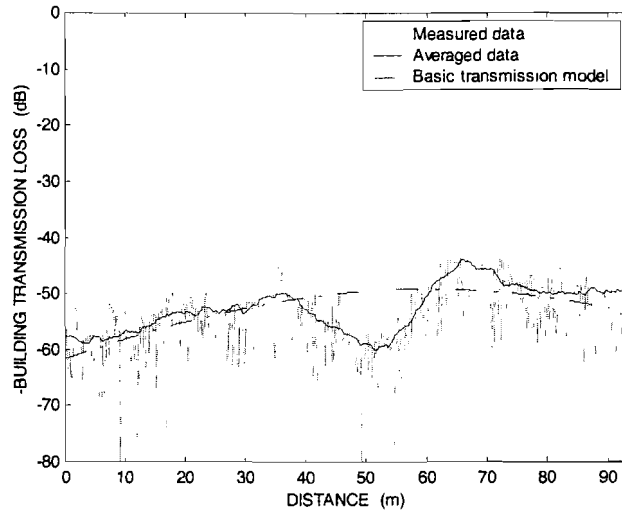
Figure 6.3: Comparison of Tx3 - Rx4 measured building transmission loss with basic transmission model.

The building transmission loss is again well predicted by the basic transmission model, with a mean error of 0.12 dB, a standard deviation of 3.84 dB and a specific building loss coefficient of 2.87 dB/m. The elevator shaft and the stairwell causes a large building transmission loss as can be seen on the 40m to 60m interval at the Rx4 path.

Finally the comparison between the measured building transmission loss and the basic transmission model for the Tx4 – Rx4 situation is given in Figure 6.4.
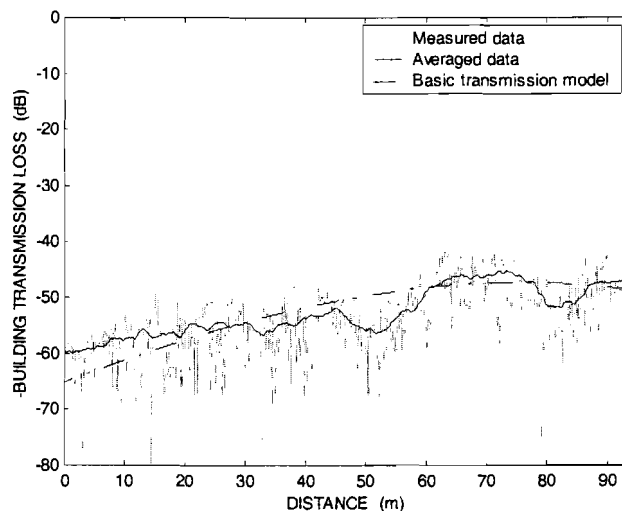
Figure 6.4: Comparison of Tx4 - Rx4 measured building transmission loss with basic transmission model.

In this measurement situation we have a mean error of 0.22 dB, a standard deviation of 2.97 dB and a specific building loss coefficient of 2.79 dB/m.

6.3 Traverse Building

In the case of the Traverse Building we performed two measurements which are compared with the basic transmission model. Figure 6.5 shows the comparison of the basic transmission model with the Tx2 – Rx4 measurement.
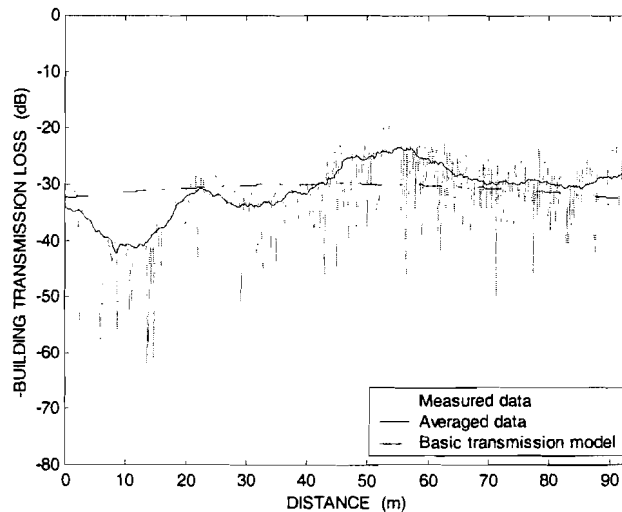
Figure 6.5: Comparison of Tx2-Rx4 measured building transmission loss with basic transmission model.

In this case we have a mean error of –0.06 dB, a standard deviation of 4.33 dB and a specific building loss coefficient of 1.21 dB/m. The internal structure of the ground floor, given in Figure 6.9, can be used to explain the differences between the basic transmission model and the measurements. As we compare two different paths (path 1 and path 3), which are drawn in Figure 6.9 we see respectively no and two internal walls perpendicular to the building surface which arise on the internal path (the effects of these internal walls in reference to the transmission will be described in detail in chapter 7). These perpendicular walls are believed to play a role in the calculation of the building transmission loss, because of the grazing incidence of the radio waves. This grazing incidence results in a large reflection coefficient and a small transmission coefficient. The position of the measured building transmission loss for path 1 and path 3 correspond to respectively 10m and 48m on the Rx4 path. When we look at Figure 6.5 we see that at a position of 10m (two internal walls) the basic transmission model predicts a smaller building transmission loss than the measured building transmission loss. At a position of 48m (no internal walls) the basic transmission model predicts a larger building transmission loss than the measured building transmission loss. Although the perpendicular walls seems to be of some importance in the prediction of the building transmission loss we choose not to include these walls in the basic transmission model. Every building has a different internal structure and in practice we have no information about the internal structure, which forms the rationale behind our choice not to include these walls. In paragraph 7.3 it will become clear that the internal walls are relatively unimportant in the prediction of the building transmission loss.

Figure 6.6 shows the comparison of the basic transmission model with the measured building transmission loss for the Tx1 – Rx4 measurement situation. In this case we have a mean error of –0.13 dB, a standard deviation of 6.02 dB and a specific building loss coefficient of 1.23 dB/m. The differences between the basic transmission model and the measured building transmission loss can be explained by the internal structure of the

building. At a distance of 60m to 90m on the Rx4 path we notice that the basic transmission model predicts a larger building transmission loss than the measured building transmission loss. When we look at Figure 6.9 we encounter a large canteen at this position. In this canteen we have no internal walls, therefore we have a small building transmission loss. At a distance of 0m to 60m on the Rx4 path we see that the basic transmission model predicts a smaller building transmission loss than the measured building transmission loss. This could be explained by the extra internal walls, perpendicular to the building surface, which arise on the transmitted ray path.
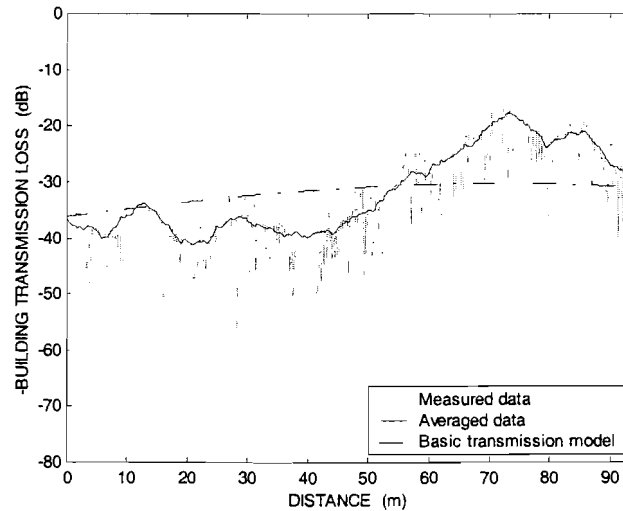
Figure 6.6: Comparison of Tx1-Rx4 measured building transmission loss with basic transmission model.

We use one specific building loss coefficient in the case of the Traverse Building. If we look at the internal structure of the Traverse Building we could divide the Traverse Building into two parts. One part (A) as a typical office building with rooms situated on both sides of a corridor and one part (B) as a office building which contains a large open area (canteen). For both of these parts we can determine a specific building loss coefficient.

Figure 6.7 shows the comparison of the measured building transmission loss and the basic transmission model containing two different specific building loss coefficients for the Tx2 – Rx4 measurement situation. For part (A) we find a specific building loss coefficient of 1.40 dB/m and for part (B) a specific building loss coefficient of 1.04 dB/m. For this case we have a mean error of –0.03 dB and a standard deviation of 2.81 dB.
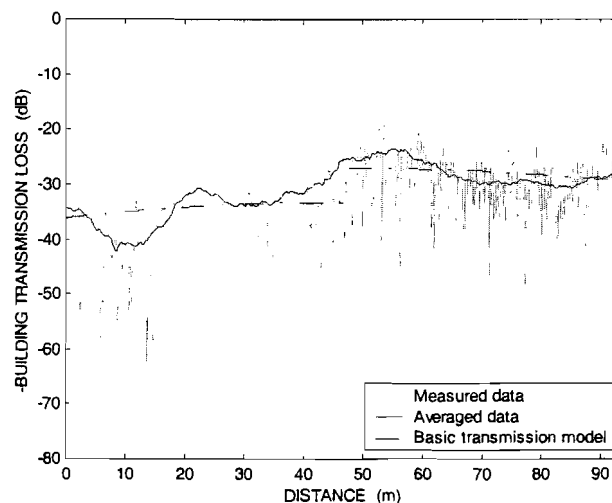
Figure 6.7: Comparison of Tx2-Rx4 measured building transmission loss with basic transmission model containing two specific building loss coefficients.

Figure 6.8 shows the comparison of the measured building transmission loss compared with the basic transmission model in the case of the Tx1 – Rx4 situation. For part (A) we find a specific building loss coefficient of 1.47 dB/m and for part (B) a specific building loss coefficient of 0.97 dB/m.
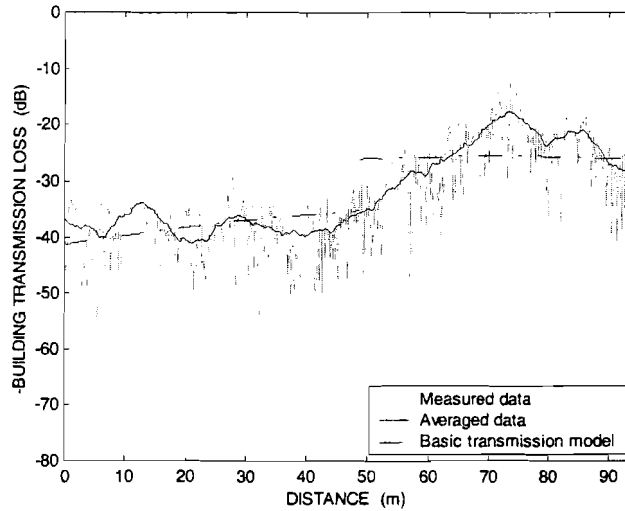
Figure 6.8: Comparison of Tx1-Rx4 measured building transmission loss with basic transmission model containing two specific building loss coefficients.

For this measurement situation we find a mean error of 0.03 dB and a standard deviation of 3.78 dB. For the above comparisons we derived the specific building loss coefficient by obtaining the smallest rms value of the prediction error. Some indoor measurements were taken to verify these coefficients in case of the Traverse Building. The results of these measurements are given in the next paragraph.

6.4 Verification of specific building loss coefficient

For three internal paths we measured the specific building loss coefficient. The three internal paths (path 2, path 3 and path 4) are shown in Figure 6.9.
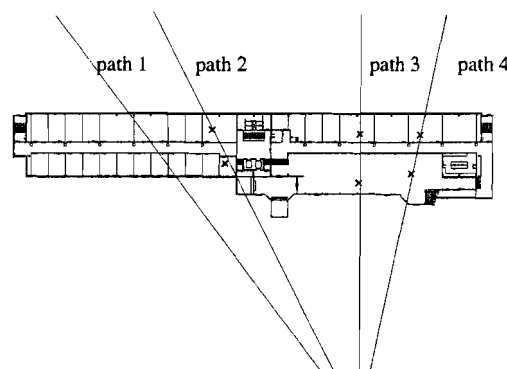
Figure 6.9: Plan view of Traverse Building (ground floor).

The crosses near each path indicate the measurement locations. For each path we measure the relative building transmission loss (L_{b_rel}), further we calculate the relative free-space loss

(L_{fs_rel}) and distance (d) between the two crosses. With these parameters we can calculate the specific building loss for each path with the following equation

$$\alpha = \frac{(L_{b\_rel} - L_{fs\_rel})}{d} .$$

(6.4)

The different parameter to calculate the specific building loss are listed in the Table 6.1

	Relative building transmission loss [dB]	Relative Free-space loss [dB]	distance [m]	Specific building loss coefficient [dB/m]
Path 2	11.38	1.17	8.62	1.18
Path 3	12.63	1.82	11.92	0.91
Path 4	10	1.34	8.81	0.98

Table 6.1: Measured specific building loss coefficient.

6.5   Conclusions

As we can see from the previous sections, the building transmission loss is well predicted by the basic transmission model. The different specific building loss coefficients found for each building are approximately the same. Therefore we can conclude that different parts of the same building can be described by the same specific building transmission loss.

The PABO Building is a typical school building with large open areas. Because of these open areas we have little or no walls that are perpendicular to the building surface. Therefore the building transmission loss, in case of the PABO Building, can be perfectly described with a specific building loss coefficient. The large building transmission loss is in contradiction with the large open areas inside the building. The external walls are believed to be the cause of the large building transmission loss.

The Traverse Building is a typical office building with rooms situated on both sides of a corridor. The differences between the measured building transmission loss and the basic transmission model can be explained by the extra walls, which are perpendicular to the building surface. Therefore a specific transmission model was derived for the Traverse Building which includes these walls. This specific transmission model will be explained in chapter 7.

Chapter 7

Specific transmission model

A specific transmission model based on the internal structure of the Traverse Building will be explained in this chapter. We use the basic transmission model and extend it with the attenuation due to internal walls that are perpendicular to the building surface. First the number of these walls as a function of the incident angle of the radio wave will be derived in case of the Tx1 – Rx4 measurement situation. Then a little theoretical background will be given about the reflection and transmission at a dielectric wall (read: internal building wall). Finally the specific transmission model will be compared with the measured data.

7.1   Number of internal walls

Figure 7.1 shows a simple plan of the internal structure of the ground floor of the Traverse Building. We use this plan to determine the number of internal walls that are perpendicular to the building surface as a function of the incidence angle.
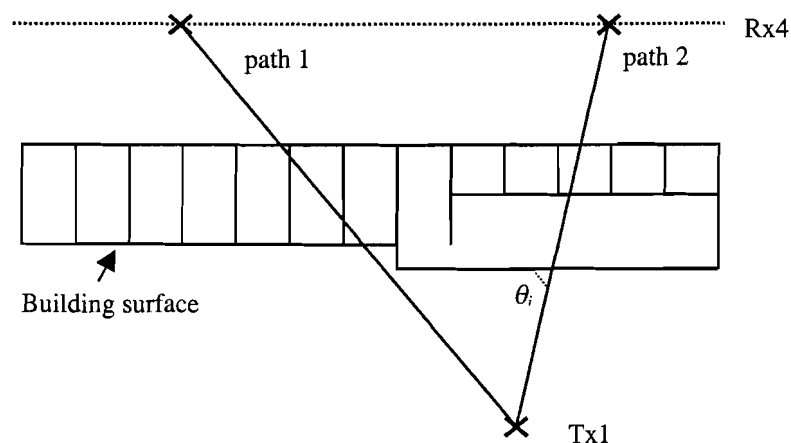
Figure 7.1: Simple plan of internal structure of Traverse Building (ground floor).

As we compare the two different paths we see, respectively, none and two internal walls perpendicular to the building surface, which arise on the path. Figure 7.2 shows the number of these walls as a function of the incidence angle θ_i.
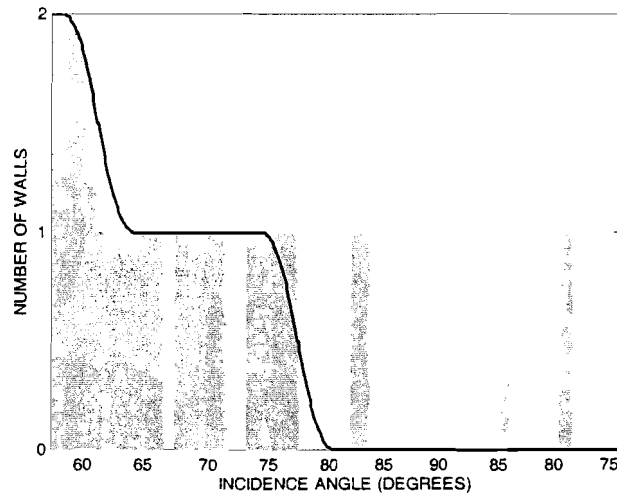
Figure 7.2: Number of internal walls that are perpendicular to the building surface.

If we include these internal walls in the transmission model, all the possible reflections and diffraction's at these walls must be included to ensure a continuous predicted field. This will result in a very complex model. To overcome this complexity we make the assumption that the number of walls as a function of the incidence angle will follow the solid line. This means that the number of walls is a real and not an integer anylonger.

7.2 Reflection and transmission at a dielectric wall

The modelling of electromagnetic transmission through an infinitely long building wall [26] is illustrated in Figure 7.3.
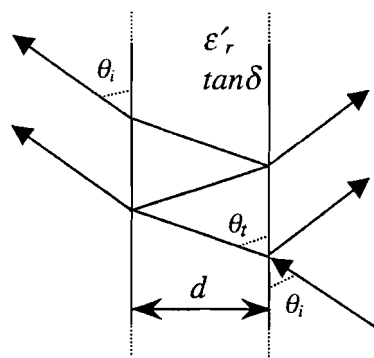
Figure 7.3: Transmission through an internal building wall.

The incidence angle is given by θ_i, the angle θ_t is given by

$$\theta_t = \pi/2 - \arctan\left(\frac{\cos\theta_i}{\mathrm{Re}\sqrt{\varepsilon_r - \cos^2\theta_i}}\right).$$

(7.1)

The soft reflection and transmission coefficients for an air/ material boundary (R_1, T_1) are given by equations (5.2) and (5.4) respectively. For an material/ air boundary the reflection and transmission coefficient (R_2, T_2) are nearly the same, except for ε'_r being changed into $1/\varepsilon'_r$ and θ_i being changed into θ_t. This will lead to $R_2 = -R_1$ and $T_1 T_2 = 1 - R_1^2$. Due to the complex nature of the permittivity of the material, a wave propagating through the material is attenuated and phase shifted. The latter is expressed in the phase of the transmission coefficient. For the calculation of the transmission coefficient of the whole wall, assumed to be infinitely long, multiple reflections and transmissions have to be taken into account. The propagation factor for the wave in the material will be

$$G = e^{(-j\frac{2\pi}{\lambda} d(\cos\theta_t \tan\theta_t + \sqrt{\varepsilon_r - \cos^2\theta_i}))}. \tag{7.2}$$

From Figure 7.3 it can be seen that subsequent rays leave the wall at different points, which will lead to mutual phase differences, expressed in the following phase factor

$$F = e^{j\frac{2\pi}{\lambda} 2d\cos\theta_i \tan(\theta_t)}. \tag{7.3}$$

The transmission coefficient of the wall, including all multiple reflections and transmissions is

$$T_{w1} = T_1 T_2 G + T_1 T_2 G^3 R_2^2 F + T_1 T_2 G^5 R_2^4 F^2 + \cdots = T_1 T_2 G \sum_{n=0}^{\infty} (G^2 R_2^2 F)^n = \frac{T_1 T_2 G}{1 - G^2 R_2^2 F}. \tag{7.4}$$

Because of the internal reflections and a longer transmission path the higher order terms in equation (7.4) are very small compared to the $T_1 T_2 G$ term and can therefore be neglected. So we use the following transmission coefficient.

$$T_{w2} = T_1 T_2 G. \tag{7.5}$$

To indicate the minor difference between the transmission coefficients given in equations (7.4) and (7.5), the absolute values of the coefficients are plotted in Figure 7.4. For the calculation we use a 10-cm thick wall made out of brick.
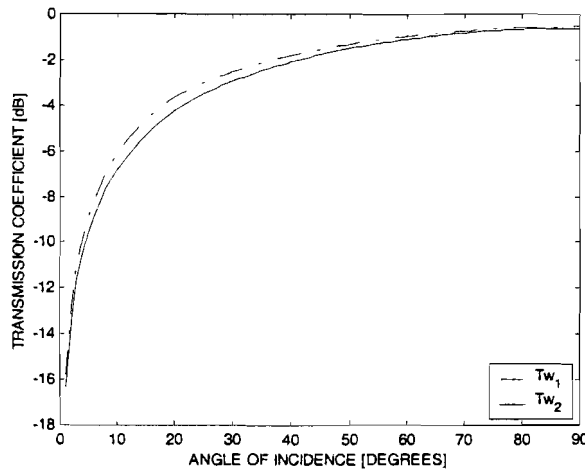
Figure 7.4: Transmission coefficients Tw_1 and Tw_2.

Table 7.1 shows some dielectric constant of typical internal building walls.

	ε'_r	$\tan\delta$
Brick	3.4	0.025
Plasterboard	2.65	0.005
Cement	2.1	0.035

Table 7.1 dielectric constants of typical internal building walls.

7.3 Comparison of specific transmission model with measurements

The building transmission loss is now given by

$$L_{b\_specific} = \alpha d_{in} - 40\log\left|T_s(\theta)\right| - \gamma 20\log\left|T_w(\theta)\right| \quad \text{dB}, \tag{7.6}$$

were γ is the number of internal walls and $T_w(\theta)$ is the transmission coefficient given in equation (7.5). The comparison of the specific transmission model with the measured building transmission loss in the case of the Tx1 - Rx4 measurement situation is given in Figure 7.5.
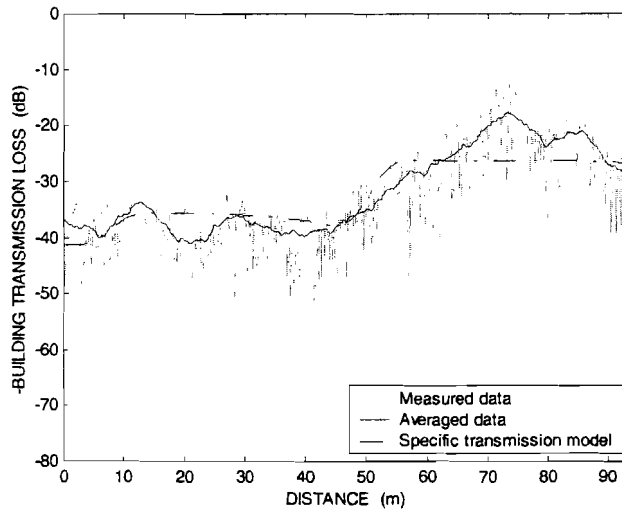
Figure 7.5: Comparison of Tx1 – Rx4 measured building transmission loss with specific transmission model.

The internal walls of the Traverse Building are made of brick and have a thickness of 10 cm. The specific building loss coefficient, which minimises the rms prediction error, was found to be 1.00 dB/m. With this specific building loss coefficient we find a mean error of –0.11 dB and a standard deviation of 3.40 dB. When we compare the specific building loss coefficient, means of error and standard deviations in this case with the basic transmisison model we can conclude that the internal walls are relatively unimportant in the prediction of the building transmission loss.

Table 7.2 summarises the means of error, standard deviations and specific transmission coefficients of all the comparisons given in chapter 6 and 7.

			Mean error [dB]	Standard deviation of errors [dB]	Specific transmission coefficient [dB/m]
Traverse Building	basic transmission model (one α)	Tx1 – Rx4	-0.13	6.02	1.23
		Tx2 – Rx4	-0.06	4.33	1.21
	basic transmission model (two α's)	Tx1 – Rx4	0.03	3.78	1.47/ 0.97
		Tx2 – Rx4	-0.03	2.81	1.40/ 1.04
	specific transmission model	Tx1 – Rx4	-0.11	3.40	1.00
PABO Building	basic transmission model (one α)	Tx1 – Rx4	0.11	2.83	2.85
		Tx2 – Rx4	0.11	4.27	2.84
		Tx3 – Rx4	0.12	3.84	2.87
		Tx4 – Rx4	0.22	2.97	2.79

Table 7.2: Means of errors, standard deviations and specific transmission coefficients.

7.4   Conclusions

We compared three transmission models with the measurements in case of the Traverse Building. For the basic transmission model with one specific building loss coefficient we have a relative large prediction error but still acceptable in the world of mobile radio communication. We can reduce the prediction error by dividing the building in different parts and find a specific building loss coefficient for each part. Further reduction of the prediction error can be achieved by including the internal structure of the building. This further reduction of the prediction error results in a 0.38 dB improvement in the case of the Tx1 – Rx4 situation. For practical reasons it is impossible to model all the internal structures of the buildings within a micro cell. Given the minor improvement in the prediction error and for practical reasons we shall now continue with the basic prediction model. The basic model gives a good prediction for both the measurements at the Traverse Building and PABO Building.

It is now the task to find a good specific building loss coefficient for each building. Given the variety of buildings it is impossible to find an α for each building, therefore we try to categorise the buildings and find an α for each category. When we look at a typical micro cell we see streets with shops located beneath an apartment, office buildings, apartments and residential row houses. In the next chapter we try to find an α for these different categories.

Chapter 8

Specific building loss coefficients for typical buildings in microcells

Some extra measurements were conducted to determine the specific building loss coefficient for typical buildings located inside microcells. Shops located beneath an apartment, office buildings, apartments and residential row houses are believed to be the most important buildings inside a microcell.

The measurements were conducted in the city Eindhoven. Table 8.1 list the category of typical buildings that have been defined and the number of measurements locations taken within each category.

Category	Number of measurement locations
Residential row houses	5
Apartments	5
Shops located beneath apartments	5
Office buildings	8

Table 8.1: Category of buildings.

For each measurement the mean error, standard deviation and specific building loss coefficient has been determined as described in chapter 6.

8.1 Representation of the measurement results

The experimental set-up, which is described in chapter 2, was used for these measurements. The loss due to the buildings relative to free-space is called the building transmission loss. The building transmission loss was measured by the measurement method described in chapter 4. For each measurement the Appendix C provide a photo of the building under test. The front view represents the side of the building that is illuminated by the transmitting antenna and the back view the side of the building, which is seen by the receiving antenna. Further the Appendix C provide a plan view of the measurement situation and a comparison of the measured building transmission loss with the basic transmission model.

8.2   Residential row houses

Five residential row houses were found to be suitable, i.e. enough space in front of and behind the row houses to place the antennas, for the building transmission loss measurements. The measurements are labelled with the street in which the residential row houses are located. The measurement results can be found in Appendix C, Table 8.2 contains the mean of errors, standard deviation and specific building loss coefficient for each measurement location.

Measurement location	Mean error [dB]	Standard deviations of error [dB]	Specific building loss coefficient [dB/m]
Heermoes (Tx1 – Rx1)	-0.07	2.16	1.35
Heermoes (Tx2 – Rx1)	-0.03	2.48	1.33
Oudaen (Tx1 – Rx1)	-0.01	1.45	1.56
Oudaen (Tx2 – Rx1)	-0.06	3.05	1.48
Kasteellaan (Tx1 – Rx1)	-0.21	2.62	1.54
Kasteellaan (Tx2 – Rx1)	-0.08	1.84	1.48
Vivaldi (Tx1 – Rx1)	-0.001	1.38	1.82
Adelaarstraat (Tx1 – Rx1)	0.17	3.98	1.69

Table 8.2: Measurement results of residential row houses.

8.3   Apartments

We found five apartments, which were found to be suitable, i.e. enough space in front of and behind the apartments to place the antennas, for the building transmission loss measurements. The measurements are labelled with the street in which the apartments are located. The measurement results can be found in Appendix C, Table 8.3 contains the mean of errors, standard deviation and specific building loss coefficient for each measurement location.

Measurement location	Mean error [dB]	Standard deviations of error [dB]	Specific building loss coefficient [dB/m]
Telemannlaan (Tx1 – Rx1)	-0.04	3.56	1.31
Regerweg (Tx1 – Rx1)	-0.42	3.88	1.16
Regerweg (Tx2 – Rx1)	-0.26	4.75	1.25
Genovevalaan (Tx1 – Rx1)	0.47	4.29	1.20
Badelochstraat (Tx1 – Rx1)	-0.31	3.80	1.86
Fruinlaan (Tx1 – Rx1)	-0.07	2.60	1.28
Fruinlaan (Tx2 – Rx2)	-0.36	3.21	1.20

Table 8.3: Measurement results of apartments.

8.4   Shops located beneath apartments

Five shops located beneath an apartment were found to be suitable, i.e. enough space in front of and behind the shops located beneath apartments to place the antennas, for the building transmission loss measurements. The measurements are labelled with the street in which the shops are located. The measurement results can be found in Appendix C, Table 8.4 contains

the mean of errors, standard deviation and specific building loss coefficient for each measurement location.

Measurement location	Mean error [dB]	Standard deviations of error [dB]	Specific building loss coefficient [dB/m]
Elkerlyclaan (Tx1 – Rx1)	-0.10	2.71	1.38
Donizettilaan (Tx1 – Rx1)	-0.08	2.36	1.51
Mendelsonlaan (Tx1 – Rx1)	-0.07	1.35	1.22
Belinnistraat (Tx1 – Rx1)	0.02	1.52	1.48
Winkelcentrum Woensel (Tx1 – Rx2)	-0.37	4.12	1.44
Winkelcentrum Woensel (Tx2 – Rx2)	-0.18	2.46	1.55

Table 8.4: Measurement results of shops located beneath apartments.

8.4 Office buildings

In addition to the already found office buildings (Traverse, PABO), we have found eight more office buildings that were suitable, i.e. enough space in front of and behind the office buildings to place the antennas, for the building transmission loss measurements. The measurements are labelled with the name of the office building. The measurement results can be found in Appendix C, Table 8.5 contains the mean of errors, standard deviation and specific building loss coefficient for each measurement location.

Measurement location	Mean error [dB]	Standard deviations of error [dB]	Specific building loss coefficient [dB/m]
Deloitte & Touch (Tx1 – Rx1)	-0.04	1.51	1.55
Franken (Tx1 – Rx1)	0.01	2.85	1.28
Pricewaterhousecoopers (Tx1 – Rx1)	0.10	1.63	1.52
Philips pensioenfonds (Tx1 – Rx1)	0.04	1.57	3.33
Randstad (Tx1 – Rx1)	-0.21	3.56	0.97
BDO (Tx1 – Rx1)	-0.06	3.09	1.47
Start (Tx1 – Rx1)	-0.03	2.72	1.54
Dela (Tx1 – Rx1)	-0.14	7.17	1.38
Traverse (Tx2 – Rx4)	-0.06	4.33	1.21
PABO (Tx1 – Rx4)	0.11	2.83	2.85

Table 8.5: Measurement results of office buildings.

8.5 Conclusions

The basic transmission model successfully describes the general trend of the measured building transmission loss. The prediction error can be reduced be choosing the proper specific building loss coefficient (α). The averaged α's of the residential row houses; apartments and shops located beneath apartments are given in Table 8.6.

The categorised buildings given in Table 8.6 roughly have the same internal structure, and are basically made out of the same materials. Because of this the α's only differ some tenth's of dB for the different measurement locations.

Category	Specific building loss coefficient [dB/m]
Residential row houses	1.53
Apartments	1.32
Shops located beneath apartments	1.43

Table 8.6: Averaged specific building loss coefficients.

The α's in case of office buildings show a relative large spread: 0.97– 3.33 dB/m. This large spread could be the result of the large variety of building materials, internal structures and shapes of the different office buildings. Although the spread is relatively large, most of the α's lie in the range of 0.97 – 1.55 dB/m. The large α in case of the Philips pensioenfonds Building could be the result of the coated windows and rough structure of the exterior walls. As for the PABO Building, the small windows are believed to be the reason for the large α.

Chapter 9

Conclusions and recommendations

Here we state the most important conclusions found by the M.Sc. project. Furthermore we give some recommendations to continue the research.

9.1 Conclusions

From the measurement results throughout the report it can be seen that transmission of radio waves through buildings is an important mechanism of propagation. In some of the cases it is the prime mechanism of propagation. Therefore it is important to include this transmission in the 2D-μFiPre model for an improved fieldstrength prediction.

For the measurement of the transmission of radio waves through buildings a fast, simple and accurate method is presented. The measured building transmission loss was found to be in the range of 20 – 60 dB, depending on the building type.

A basic transmission model has been developed and compared with the measured field due to transmission through buildings. The results of the basic transmission model are in good agreement with the measurement results. For one building a specific transmission model was developed that includes the internal structure of the building. When compared to the basic transmission model, the improvement of this model is minimal; the internal structure is therefore relatively unimportant in the modelling of the building transmission loss.

When comparing the basic transmission model with the measurement results, mean errors of $\pm$ 0.2 dB and standard deviations of $\pm$ 3 dB can be achieved if the proper specific building loss coefficient is selected. To determine this specific building loss coefficient the buildings are categorised by type: residential row houses, apartments, shops located beneath apartments and office buildings. For each of these categories measurements were conducted to determine the specific building loss coefficient. Table 9.1 shows the averaged specific building loss coefficient. With this averaged specific building loss coefficient the overall mean of the prediction error was calculated using all measured data of each category (see Table 9.1). The overall standard deviation, in Table 9.1, of each category was calculated using this overall mean. The overall standard deviation in case of the office building category is relatively large compared with the other categories, which is the result of the large spread in the specific building loss coefficient. The first three categories in Table 9.1 have roughly the same internal structure and are basically made out of the same materials. The specific building loss coefficients therefore only differ some tenths of dB for the different measurement locations.

Category	Specific building loss coefficient [dB/m]	overall mean error [dB]	overall standard deviation of error [dB]
Residential row houses	1.53	-0.09	2.83
Apartments	1.32	0.02	4.89
Shops located beneath apartments	1.43	0.56	3.23
Office buildings	1.71	0.90	11.09

Table 9.1: Averaged specific building loss coefficients.

The α's in case of office buildings show a relative large spread: 0.97 – 3.33 dB/m. This large spread could be the result of the large variety of building materials, internal structures and shapes of the different office buildings. Although the spread is relatively large, most of the α's lie in the range of 0.97 – 1.55 dB/m.

9.2 Recommendations

The presented method for a fast, simple and accurate measurement of transmission of radio waves through buildings was used to distinguish the transmission from other mechanisms of propagation. This method could also be used for the separation of other important contributions to the total field. With this information, reflection coefficients of specific surfaces or diffraction coefficient of building corners could be determined.

The ε_r used in the transmission coefficient is that of brick with a relative humidity of 5%. For the categories residential row houses, apartments and shops located beneath apartments, the spread in the specific building loss coefficient is relatively small. Therefore we may conclude that the proper ε_r was used in the calculation of the building transmission loss. Some extra measurements are recommended in these categories to verify the values of the α's. As for office buildings we see a relative larger spread in the α's. The reason of this may be found in the different building materials. Therefore we recommend further investigation of the different building materials used for office buildings and subdivide the category office building in smaller categories each with a different ε_r.

The losses due to the external building walls are now partly described by the transmission coefficient and partly by the specific building loss coefficient. We could refine the basic transmission model by including the actual physical external wall losses. The remaining losses due to the internal structure and furniture could then also be accounted for by a specific building loss coefficient.

Bibliography

[1]   Okumura Y, et al., "*Field strength and its variability in VHF and UHF land mobile service,*" Rev. Elec. Comm. Lab., vol. 16, 1968, pp 825-873.

[2]   Jong Y.L.C de and M.H.A.J.Herben and J.-F. Wagen and A. Mawira, "*Transmission of UHF waves through buildings in urban cellular environments,*" Electr. Letters, vol. 35, no. 9, April 1999, pp. 743-745.

[3]   Dooren G.A.J. van and M.H.A.J. Herben,"*A deterministic approach for the modelling of wave propagation around buildings,*" Journal of Electromagn. Waves and Appl., vol. 8, 1994, pp. 175-194.

[4]   Dooren G.A.J. van, "*A deterministic approach for the planning of microcellular mobile radio communication system,*" in Proc. 5th IEEE Int. Symp. PIMRC'94, The Hague, 1994, pp. 389-395.

[5]   Klaassen M.G.J.J. and A. Mawira, "*A deterministic model for the planning of microcellular mobile radio communication systems,*" PIMRC'94, Conference Proceedings, 1994, pp.389-395.

[6]   Jong Y.L.C. de and M.H.A.J Herben, "*Experimental verification of ray-tracing based propagation prediction models for urban microcell environments,*" IEEE Trans. Veh. Technol., vol. 3, September 1999, pp 1434-1438.

[7]   Felsen L.B and N.Marcuvitz, "*Radiation and Scattering of Waves,*" Originally published : Englewood Cliffs, N.J.:Prentice – Hall, 1972, c1973.

[8]   Tiberio R. and G. pelosi and G. Manara, "*A uniform GTD formulation for the diffraction by a wedge with impedance faces,*" IEEE Trans. Antennas Propagat., vol. 33, no.8, pp.867-873, 1985.

[9]   Jong Y.L.C. de and M.H.A.J.Herben, "*Accurate identification of scatterers for improved microcell propagation modelling,*" in Proc. 8th IEEE Int. Symp. Personal, Indoor and Mobile Radio Communications (PIMRC'97), Helsinki, Finland, vol. 2, 1997, pp. 645-649.

[10]   Jong Y.L.C de and M.H.A.J.Herben, "*High-resolution angle-of-arrival estimation for improved microcell propagation modelling,*" in Proc. 8th ProRISC/IEEE Workshop CSSP-97, Mierlo, The Netherlands, 1997, pp. 247-253.

[11]   Jong Y.L.C de and M.H.A.J.Herben and A. Mawira, "*High-resolution time delay and angle-of-arrival measurements in multipath environments,*" in Proc. 8th URSI-F Triennial Open Symp, Aveiro Portugal, 1998, pp. 208-211.

[12]   COST 231 Final Report, "Digital mobile radio: COST 231 view on the evolution towards 3rd generation systems,: European comission – COST Telecommunications, Brussel, Belgium, 1998.

[13]   Stavrou S and M.Fiacco and S.R.Saunders, "Outdoor to indoor window penetration modelling at 2 and 5 GHz," Millenium conference on Antennas and Propagat. AP 2000, ESA SP-444 proceedings, 9 – 14 April, Davos, Switzerland.

[14]   Manabe T. and H. Takai, "*Superresolution of multipath delay profiles measured by PN correlation method,*" IEEE Trans. Antennas Propagat., vol. 20, September, 1972, pp. 500-509.

[15]   Cox D.C., "*Delay doppler characteristics of multipath propagation at 910 MHz in a suburban mobile environment,*" IEEE Trans. Antennas Propagat., vol. 20, September 1972, pp. 625-635.

[16]   Schmidt R.O., "*Multiple emitter location and signal parameter estimation,*" IEEE Trans. Antennas Propagat., vol. 34, March 1986, pp. 276-280.

[17]   Jong Y.L.C. de and M.H.A.J. Herben, "High-resolution angle-of-arrival measurement of the mobile radio channel," IEEE Trans. Antennas Propagat., vol. 47, no.11, November 1999, pp 1677-1687.

[18]   Mathews C.P. and M.D. Zoltowski, "*Eigenstructure techniques for 2-D angle estimation with uniform circular arrays,*" IEEE Trans. Antennas Propagat., vol. 42, no. 9, 1994, pp. 2395-2407.

[19]   Godara L.C. , "*Applications of antenna arrays to mobile communications, part II: beam-forming and direction-of-arrival considerations,*" Proc. IEEE, vol. 85, no.8, Augustus 1997, pp.1195-1245.

[20]   Rossi J.-P. et al., "*Theory and measurement of the angle of arrival and time delay of UHF radiowaves using a ring array,*" IEEE Trans. Antennas Propagat., vol. 45, no. 5, May 1997, pp.876-884.

[21]   Xu G. and R.H. Roy and T. Kailath, "*Detection of number of sources via exploitation of centro-symmetrie property,*" IEEE Trans. Signal Proc., vol. 42, no. 1, January 1994, pp. 102 112.

[22]   Wax M. and J. Sheinvald, "*Direction finding of coherent signals via spatial smoothing for uniform circular arrays,*" IEEE Trans. Antennas Propagat., vol. 42, no. 5, May 1994, pp. 613-620.

[23]   Lee W.C.Y., "*Mobile communication design fundamentals,*" Howard W.sams & Co., 1986, pp.52 –54

[24]   Lee W.C.Y., "*Mobile cellular telecommunications systems,*" McGraw–Hill Book Co., International edition, 1990, pp.13-14.

[25]   Lee C.Y. "*Mobile communications engineering,*" second edition, 1998, pp. 128-130.

[26]   Klaassen M.G.J.J and E. kooistra and H.J.F.G. Govaerts and M.H.A.J. Herben and G. Brussaard, "*Validation of the GTD/UTD-based LMS channel simulator,*" Final report of ESA/ESTEC contract PO 144125, September 1995.

Appendix A

Traverse Building – angular distributions
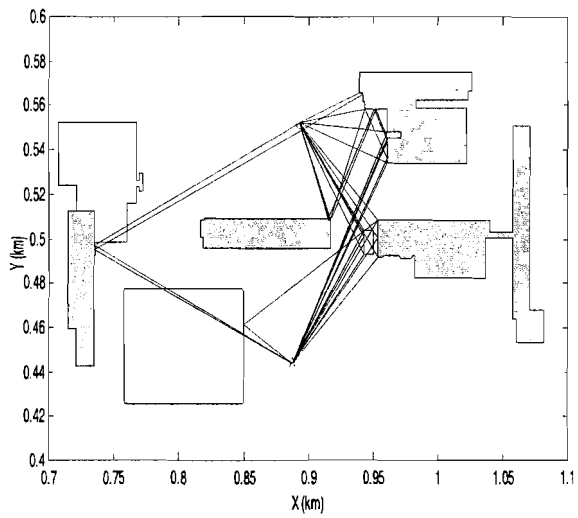
(a)
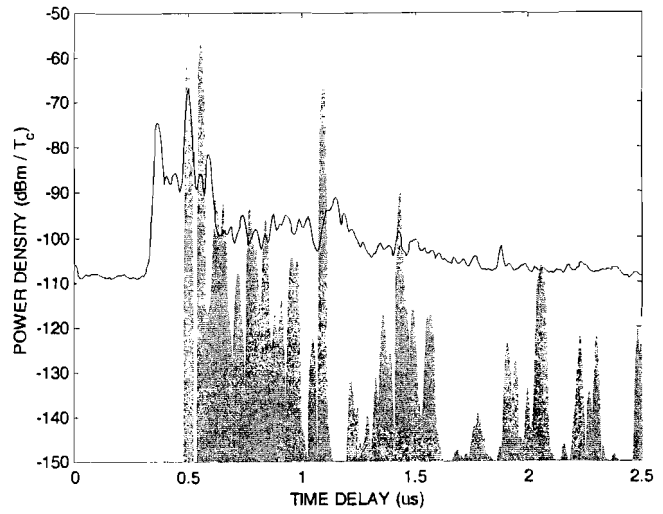
(b)
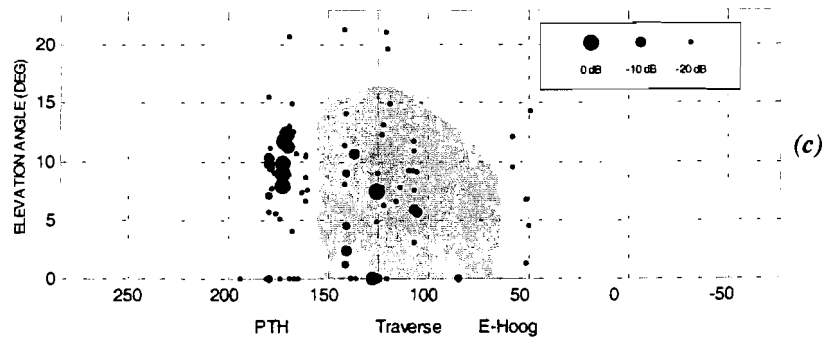
(c)
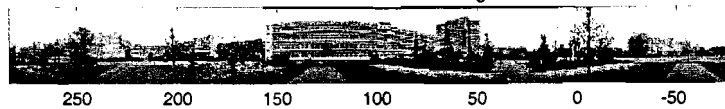
(d)
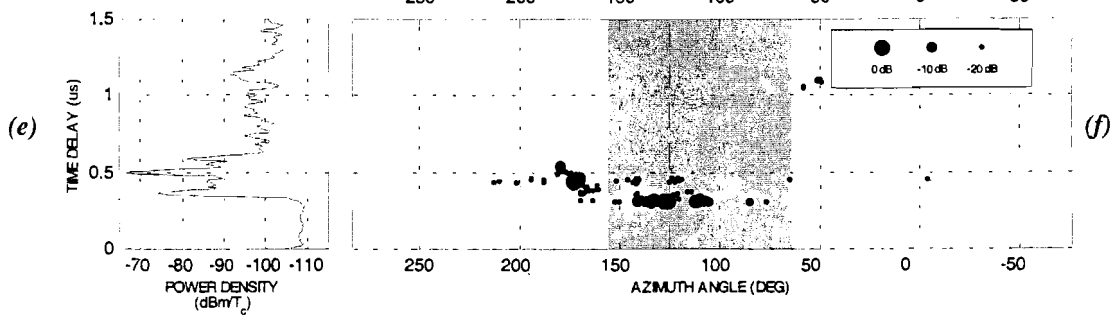
(e)

(f)

Figure A.1: Tx1 – Rx1.

(a)

(b)

(c)

(d)

(e)

(f)
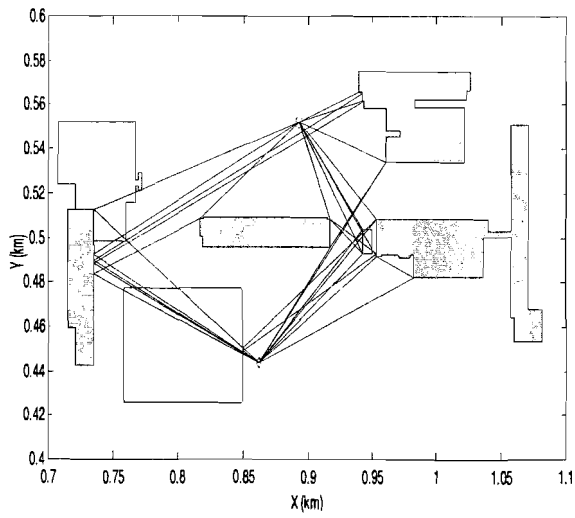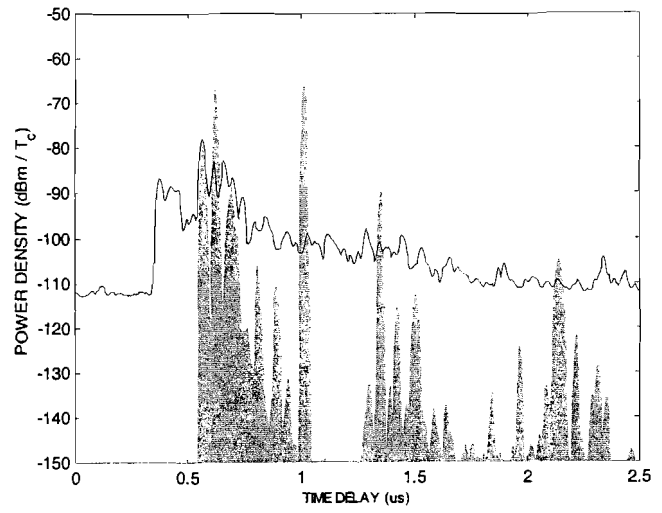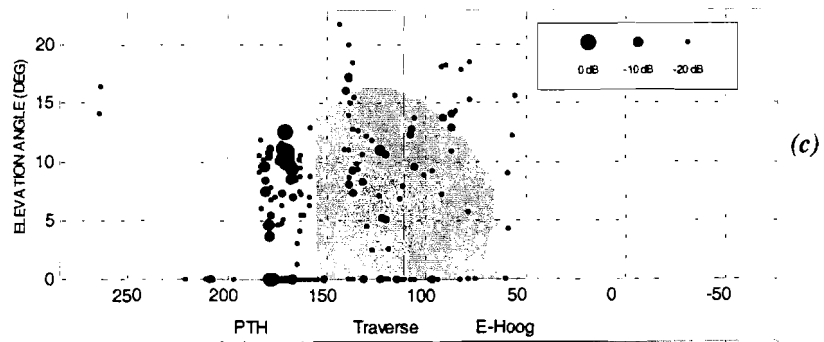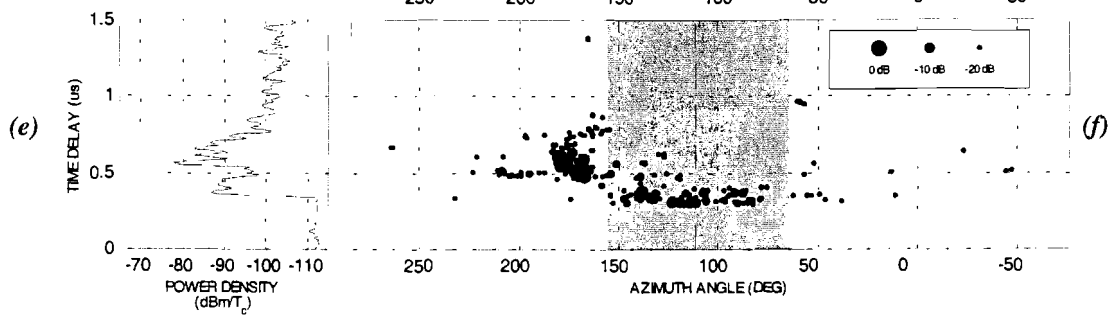
Figure B.2: Tx2 – Rx1.
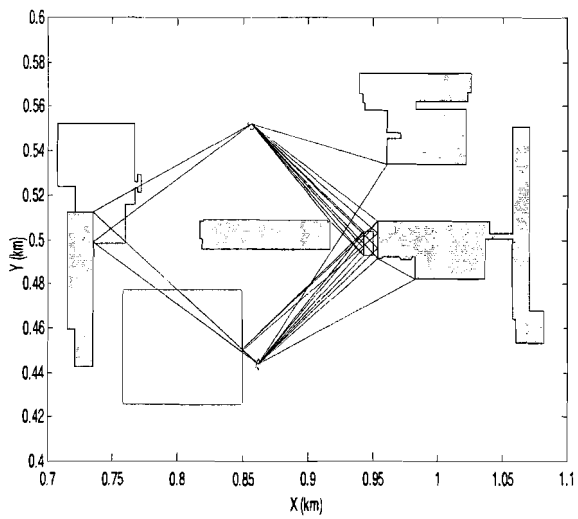
(a)
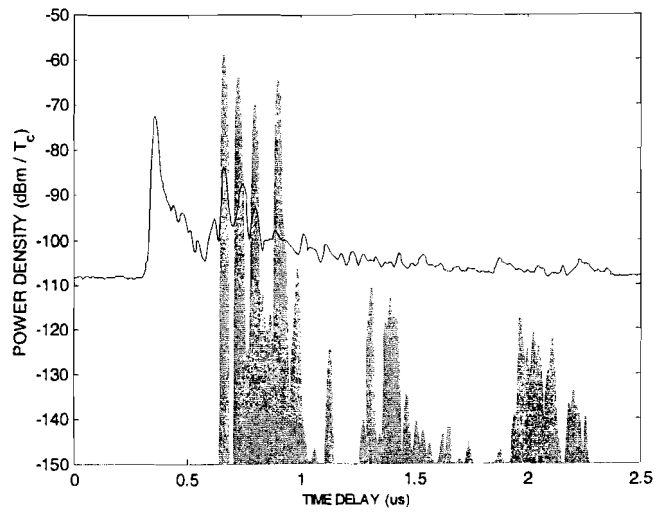
(b)
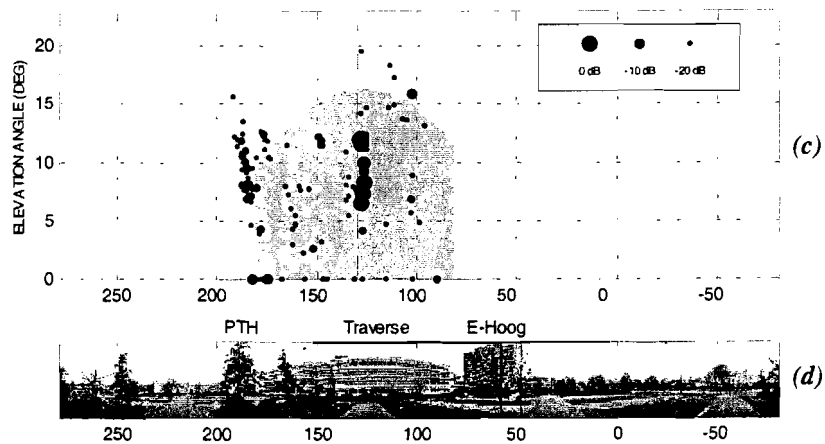
(c)
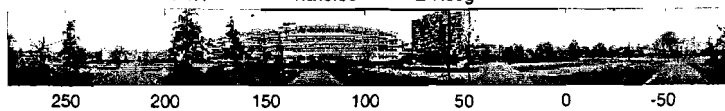
(d)
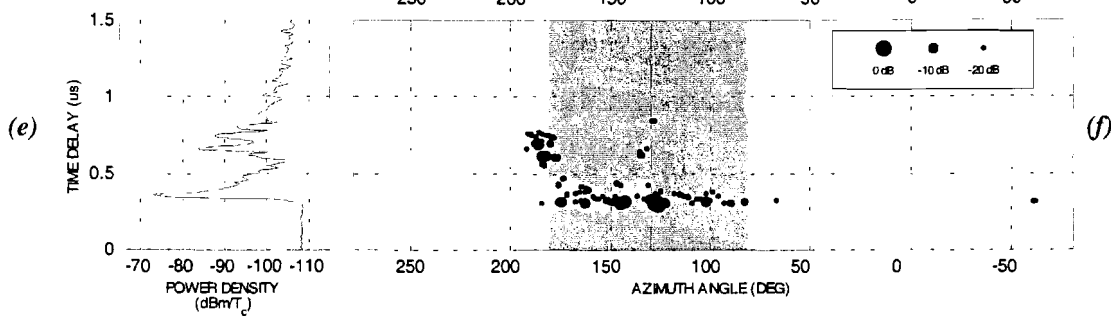
(e)

(f)

Figure A.3: Tx2 – Rx2.
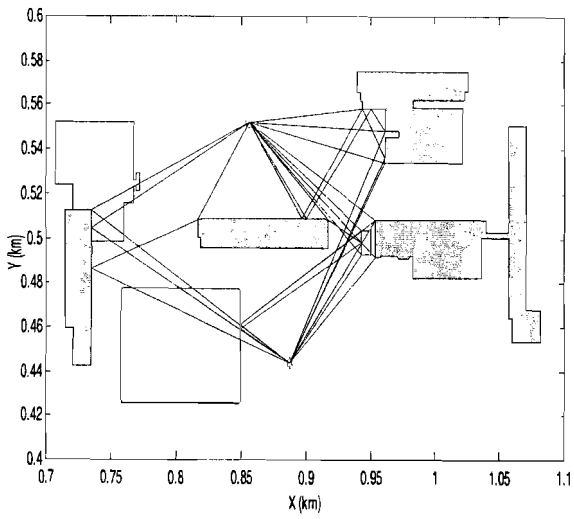
(a)
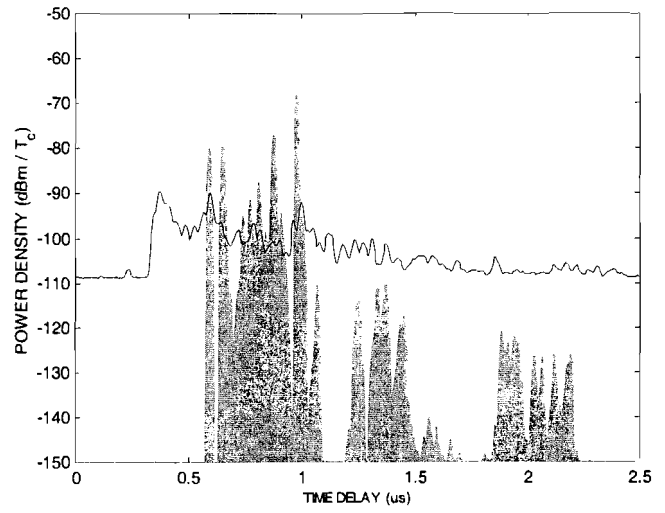
(b)
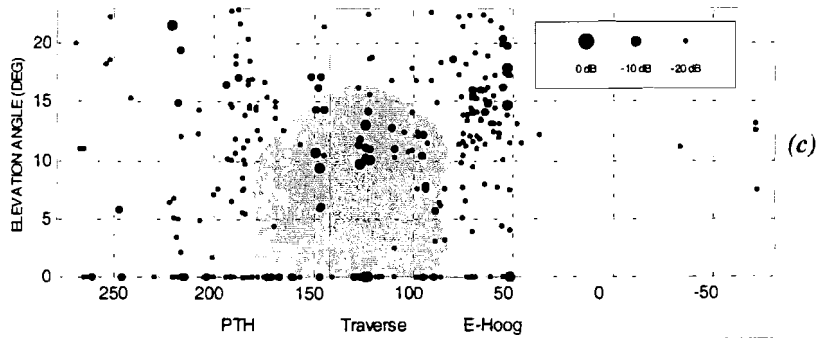
(c)
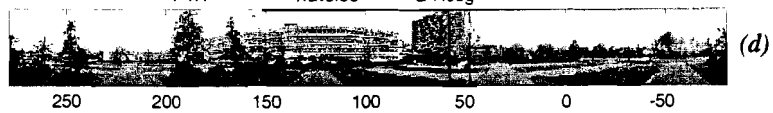
(d)
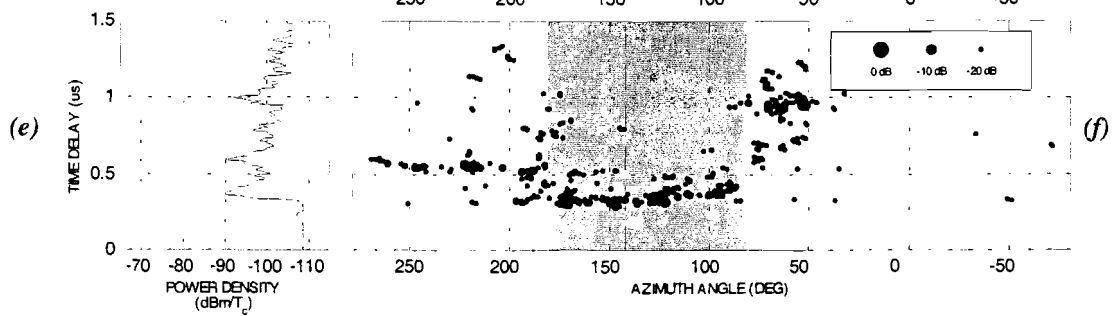
(e)

(f)

Figure A.4: Tx1 – Rx2.
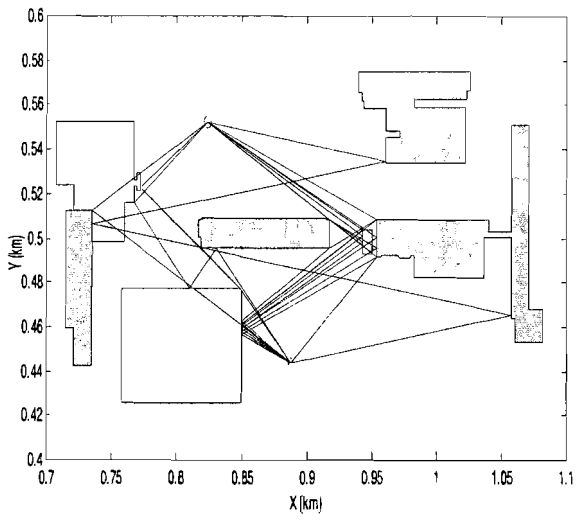
(a)
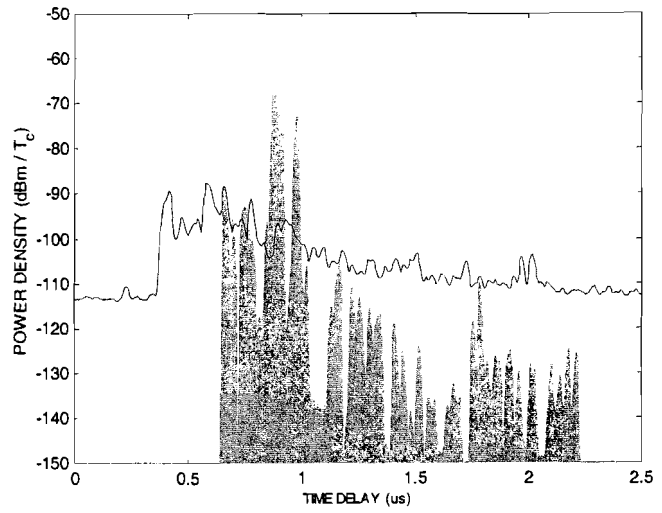
(b)
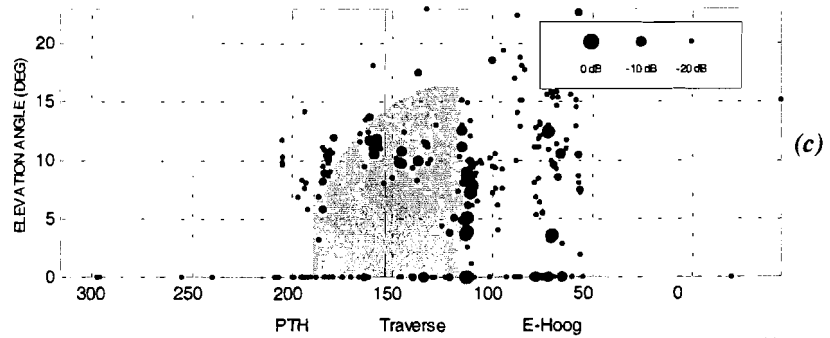
(c)
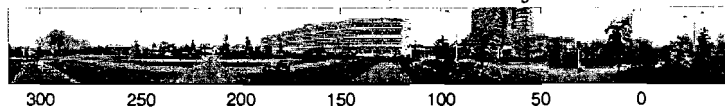
(d)
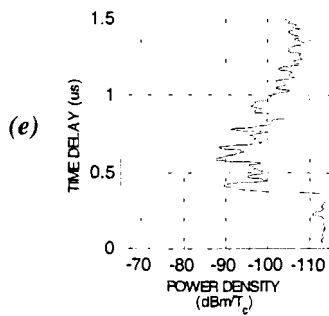
(e)
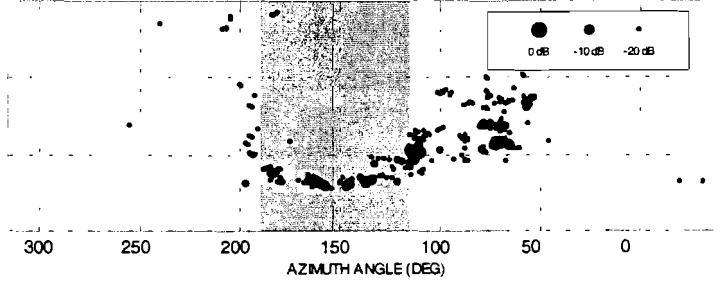
(f)

Figure A.5: Tx1 – Rx3.
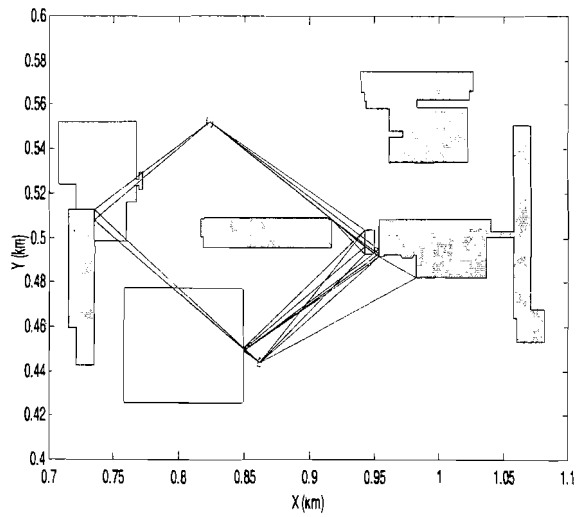
(a)
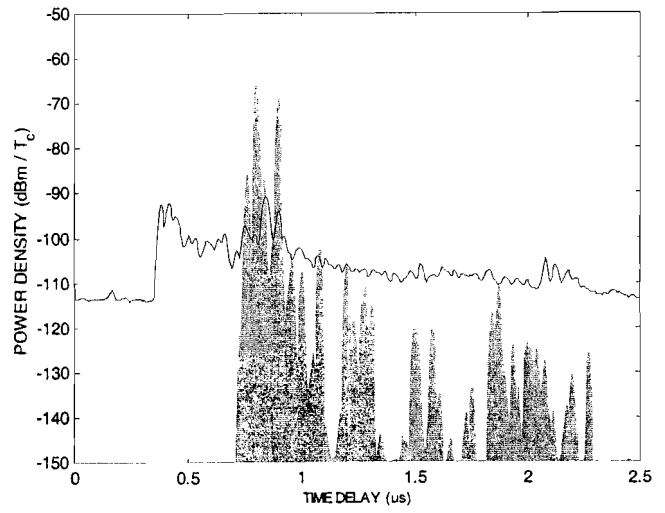
(b)
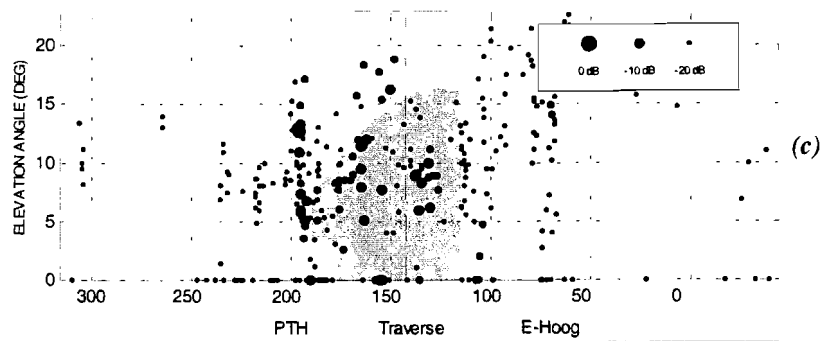
(c)

(d)
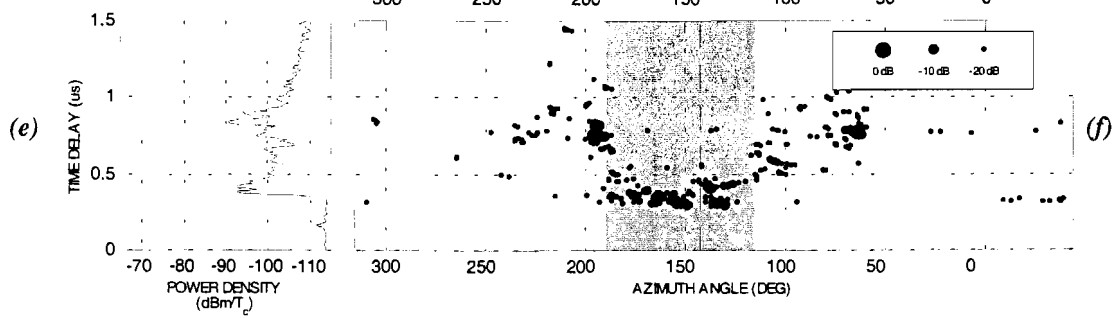
(e)

(f)

Figure A.6: Tx2 – Rx3.

Appendix B

PABO Building – angular distributions

(a)

(b)

(c)

PABO   IPO

(d)

(e)   (f)

Figure B.1: Tx1 – Rx1

(a)

(b)

(c)

(d)

(e)

(f)
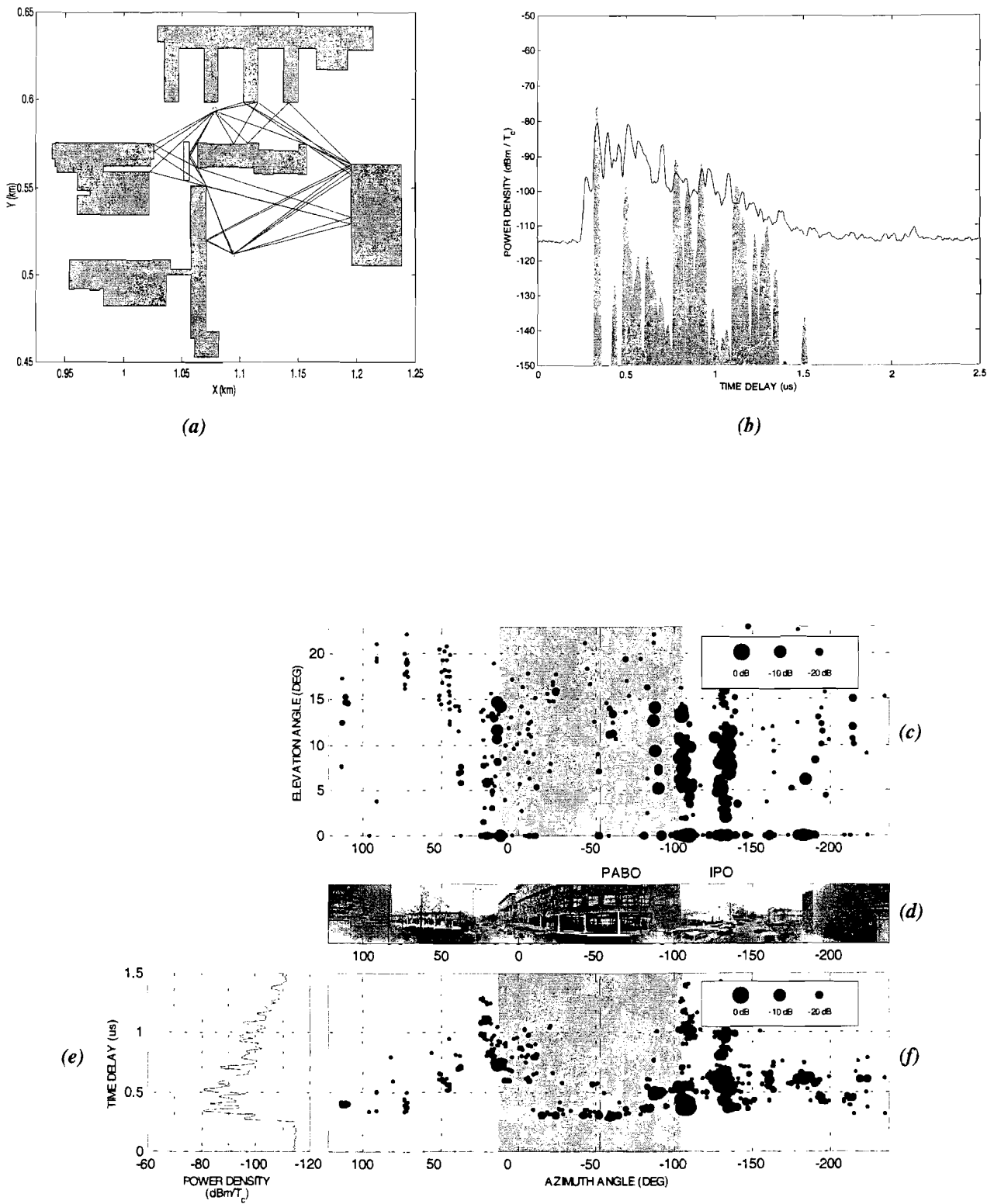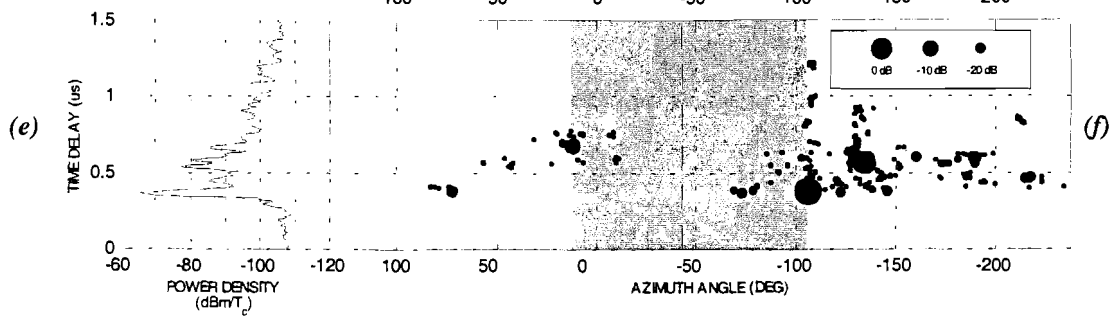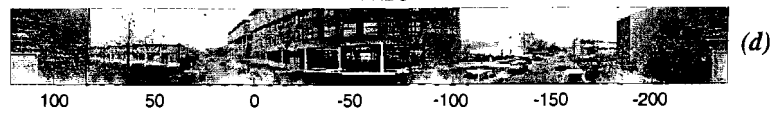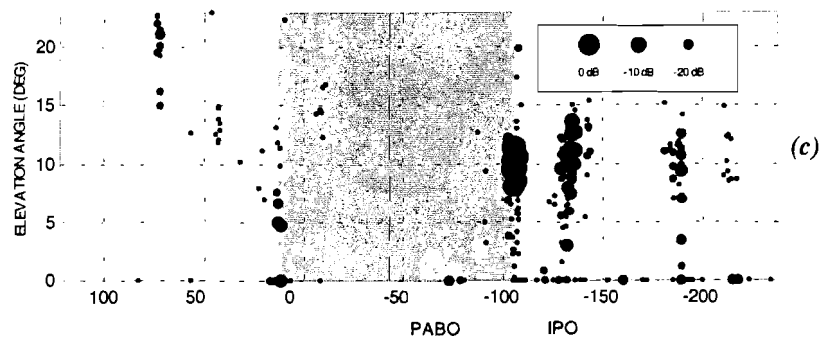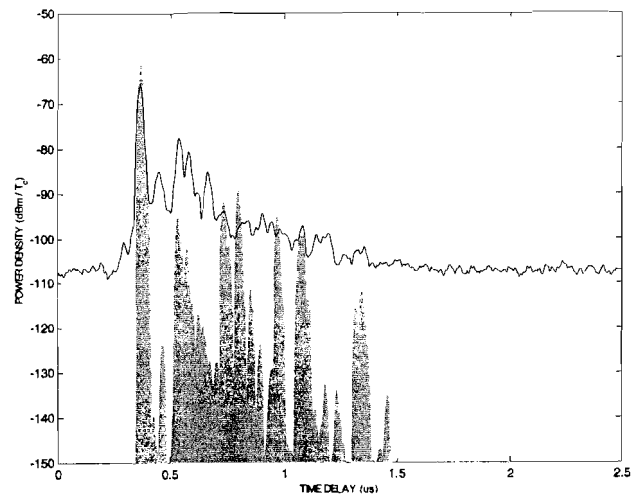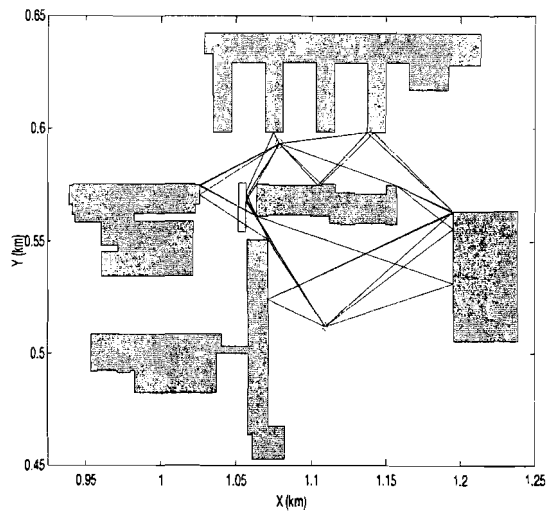
Figure B.2: Tx2 – Rx1.
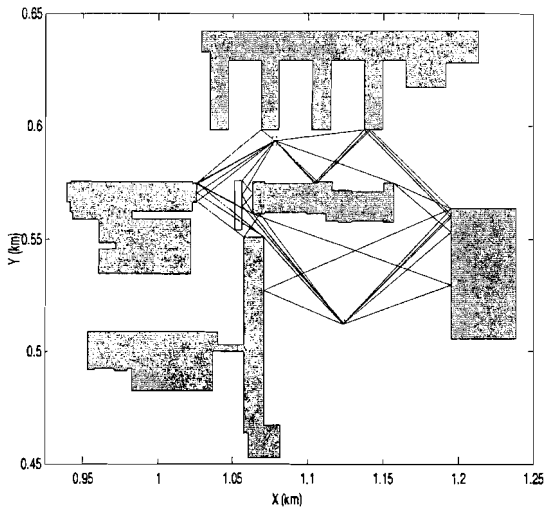
(a)
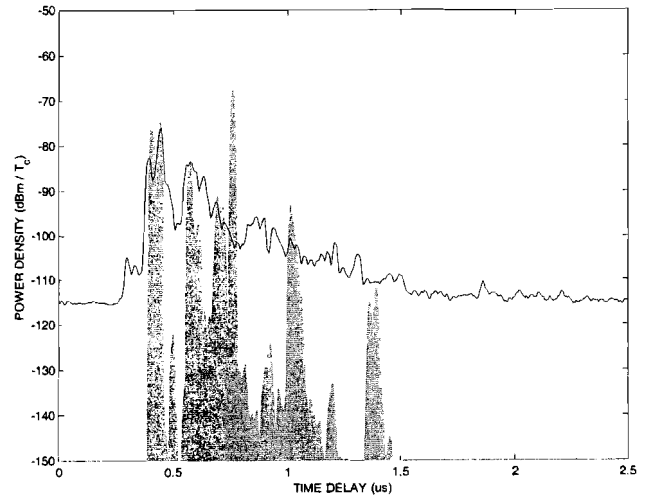
(b)
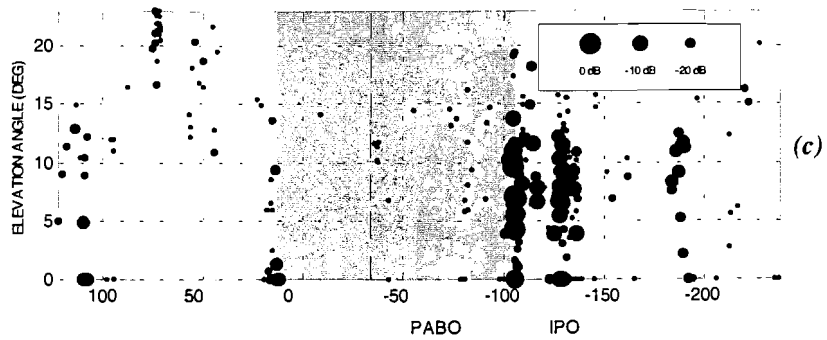
(c)
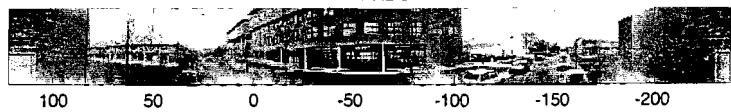
(d)
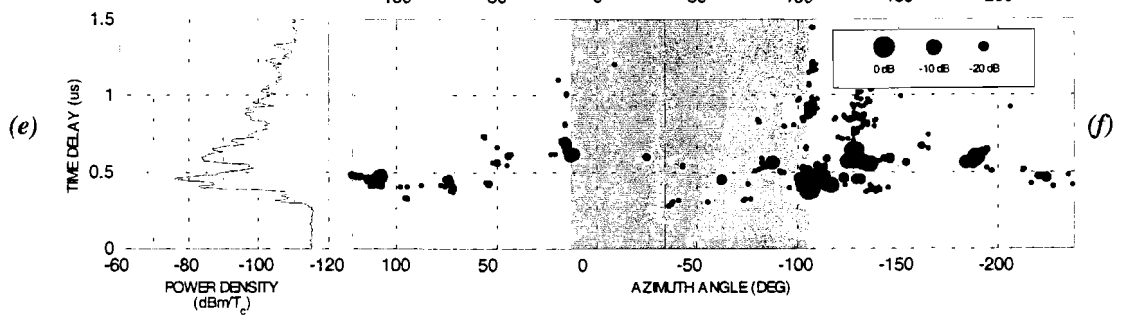
(e)

(f)

Figure B.3: Tx3 – Rx1.
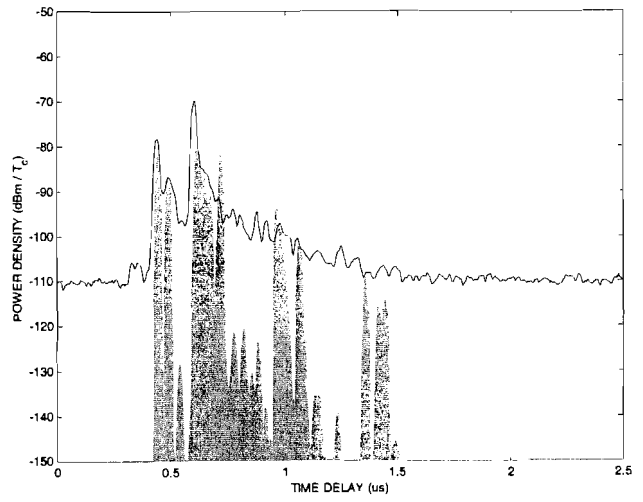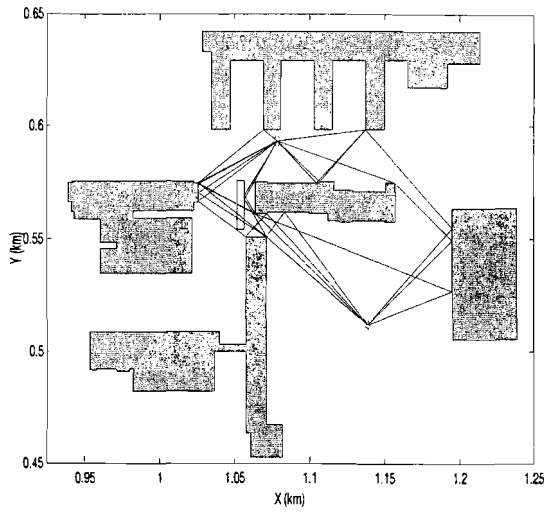
(a)

(b)
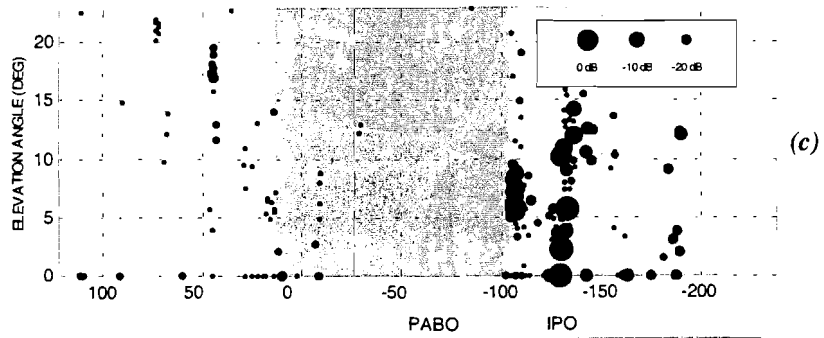
(c)
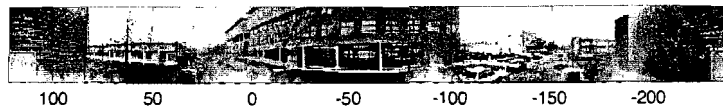
(d)
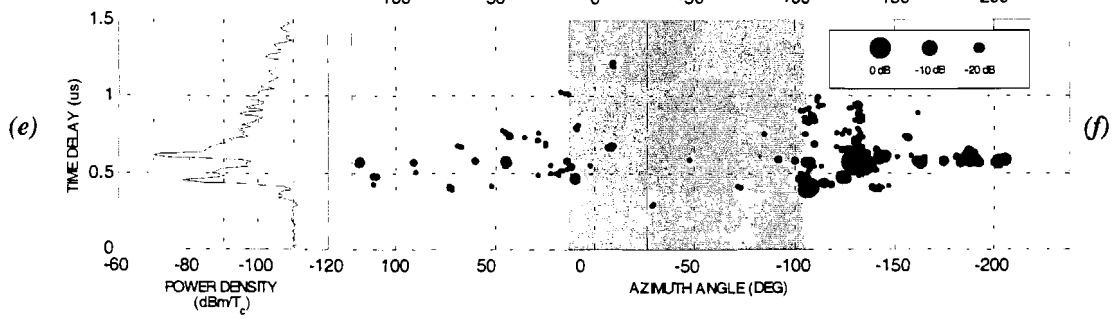
(e)

(f)

Figure B.4: Tx4 –Rx1.
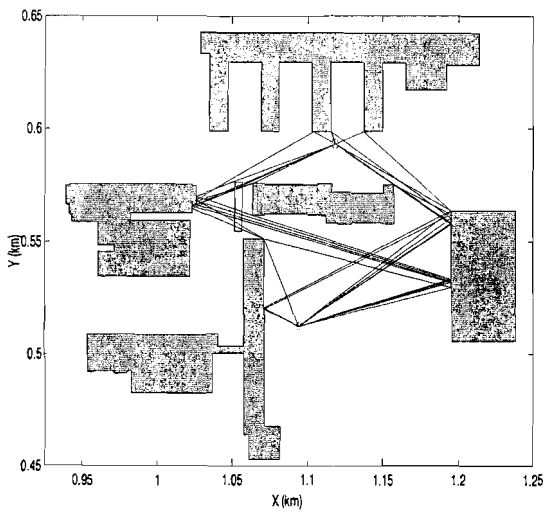
(a)
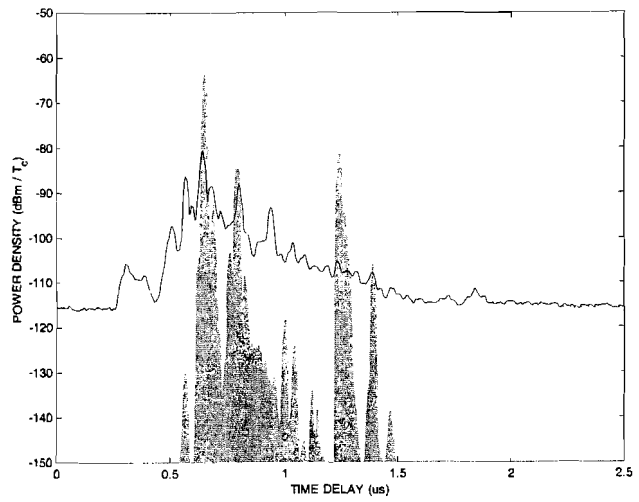
(b)
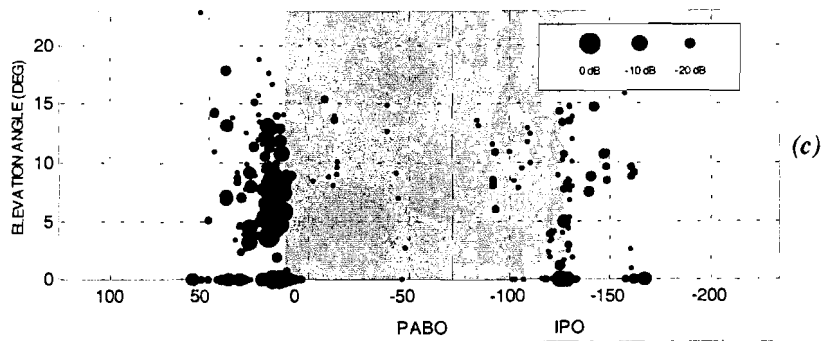
(c)
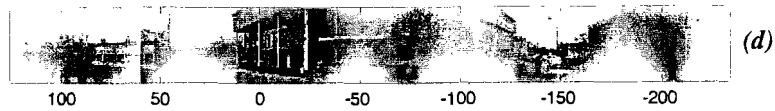
(d)
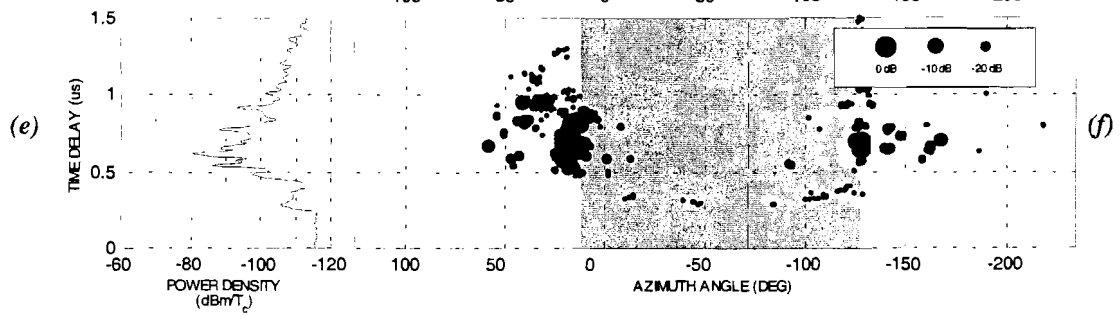
(e)

(f)

Figure B.5: Tx1 – Rx2.

(a)

(b)

(c)

(d)

(e)

(f)
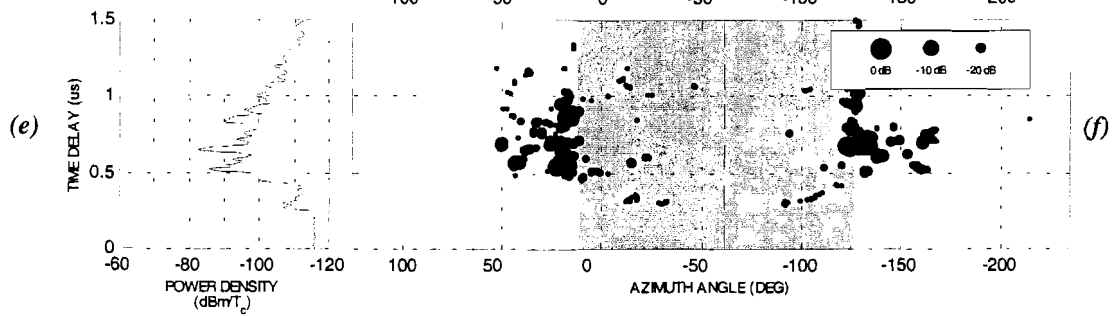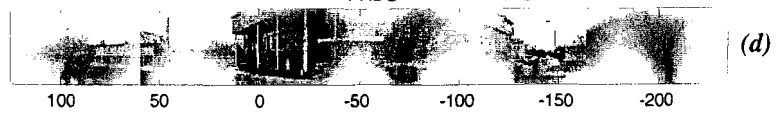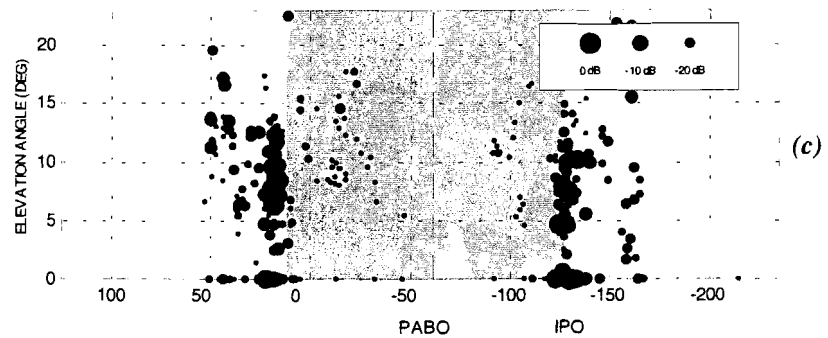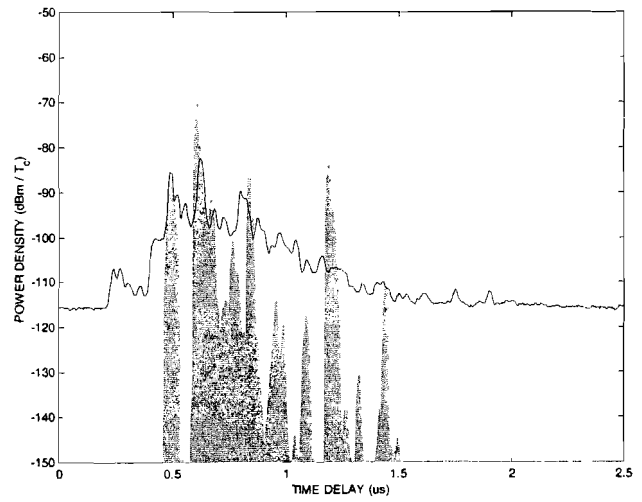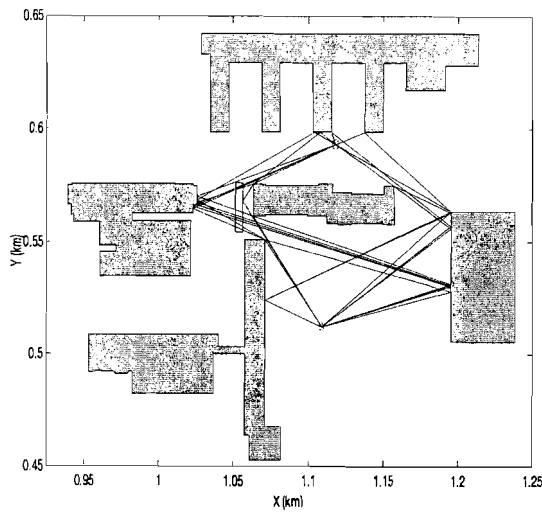
Figure B.6: Tx2 – Rx2.

(a)

(b)

(c)

(d)

(e)

(f)
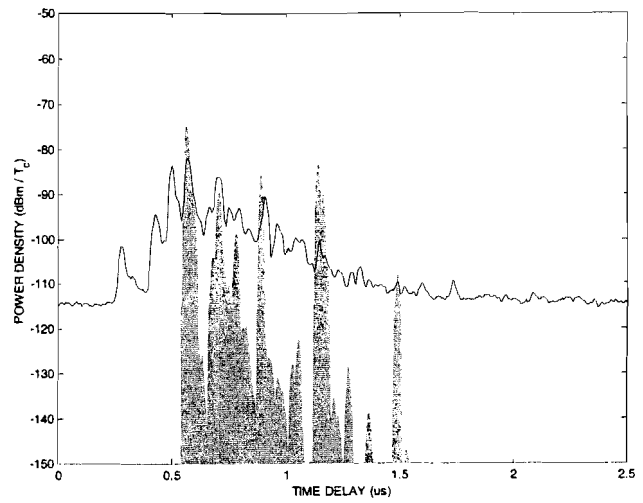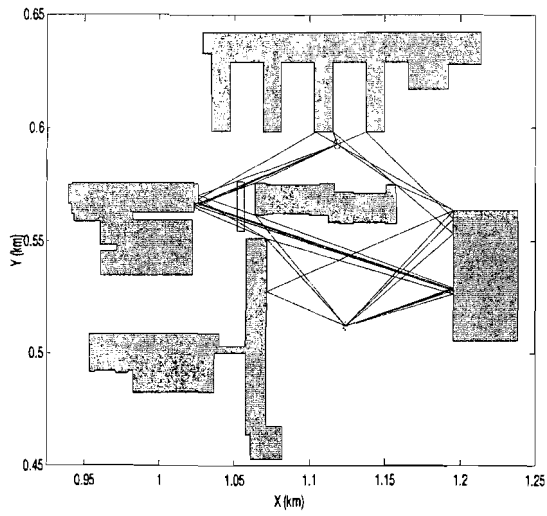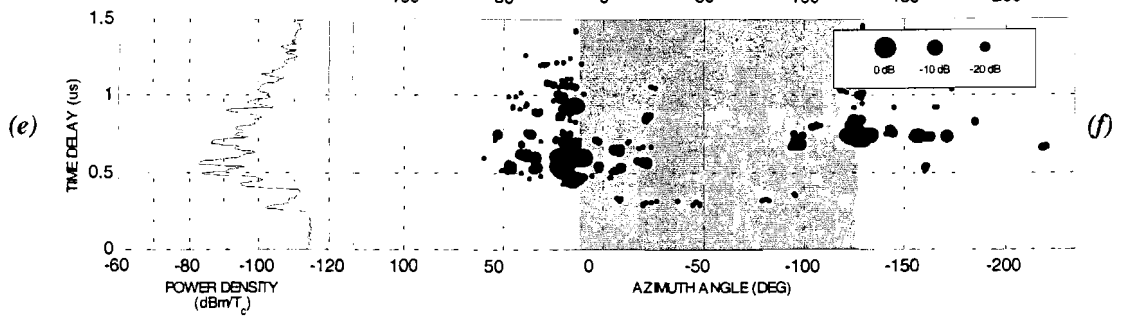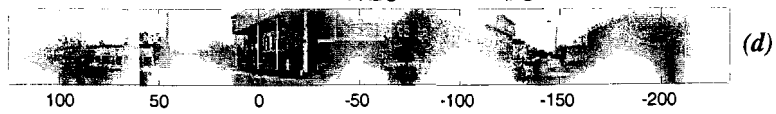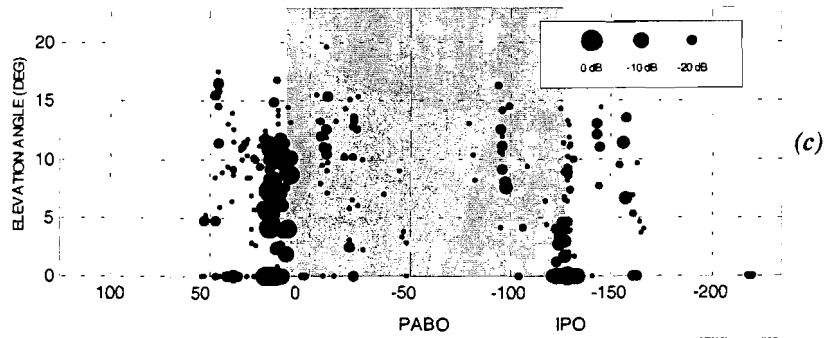
Figure B.7: Tx3 – Rx2.
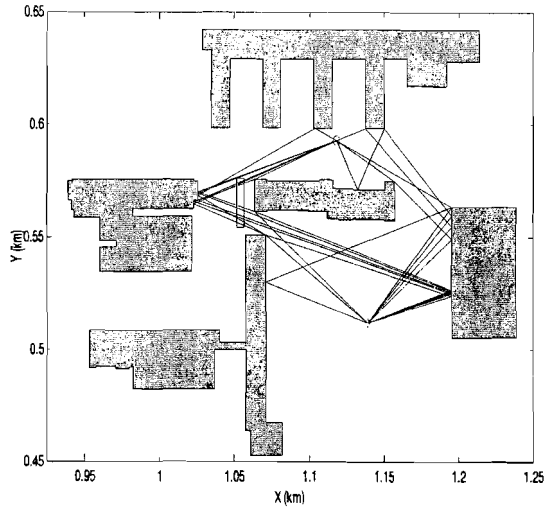
(a)
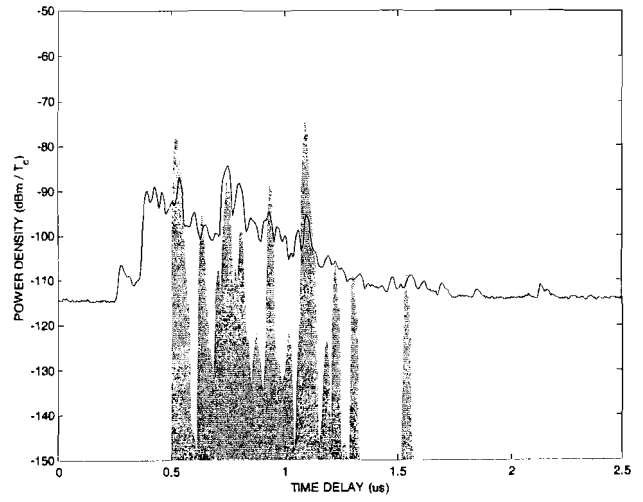
(b)
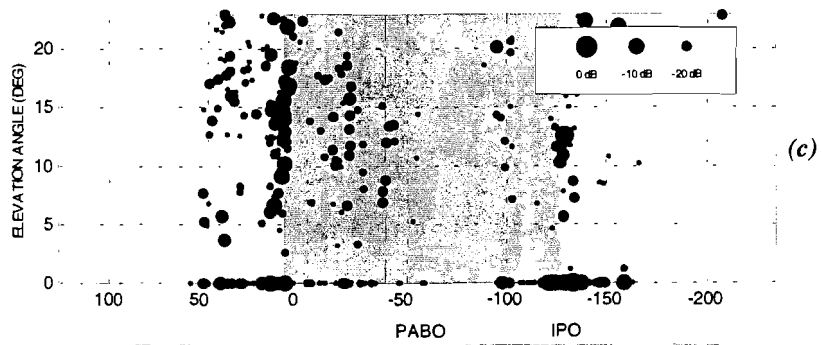
(c)
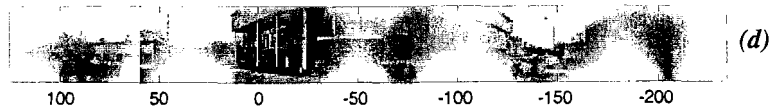
(d)
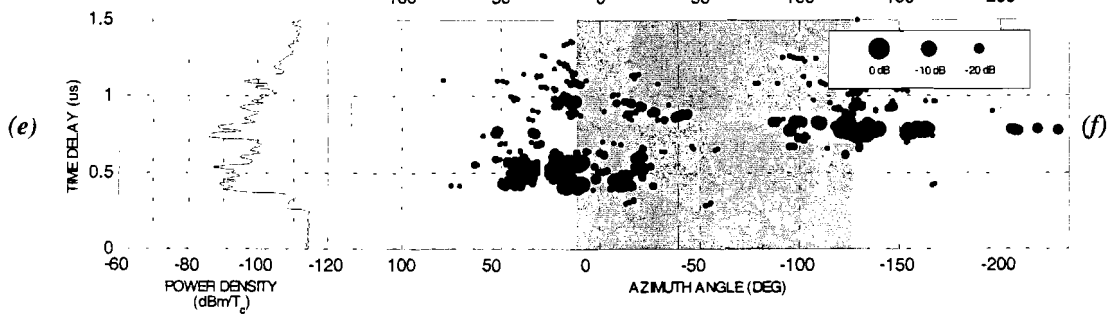
(e)
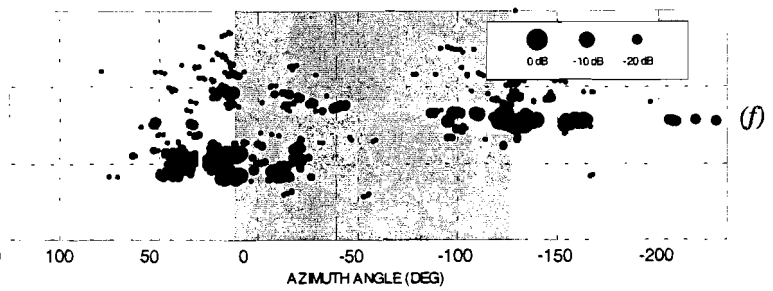
(f)

Figure B.8: Tx4 – Rx2.
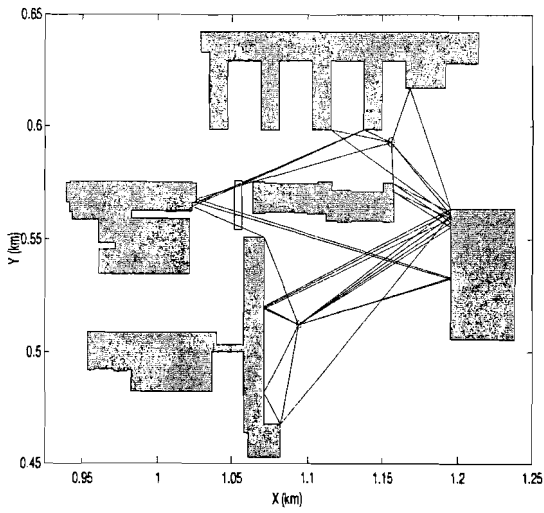
(a)
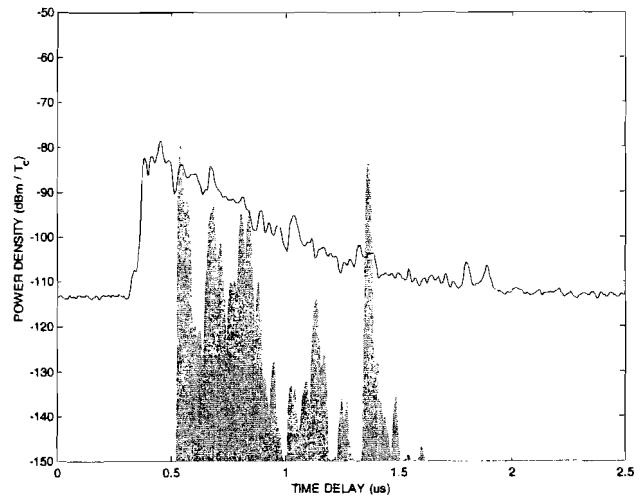
(b)
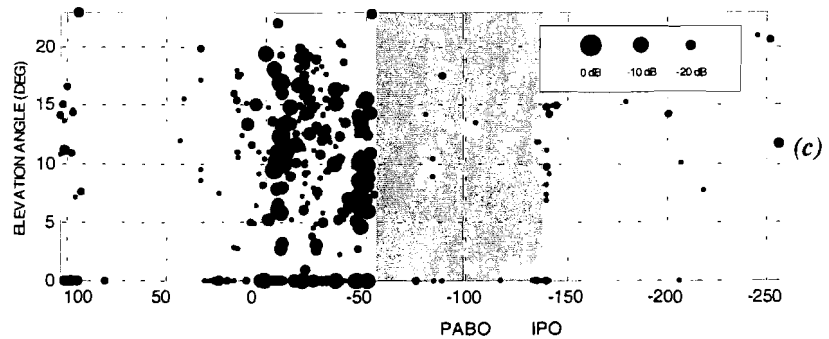
(c)
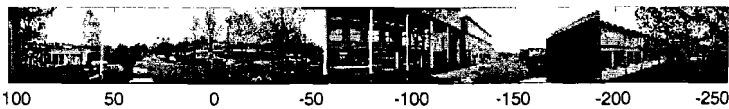
(d)
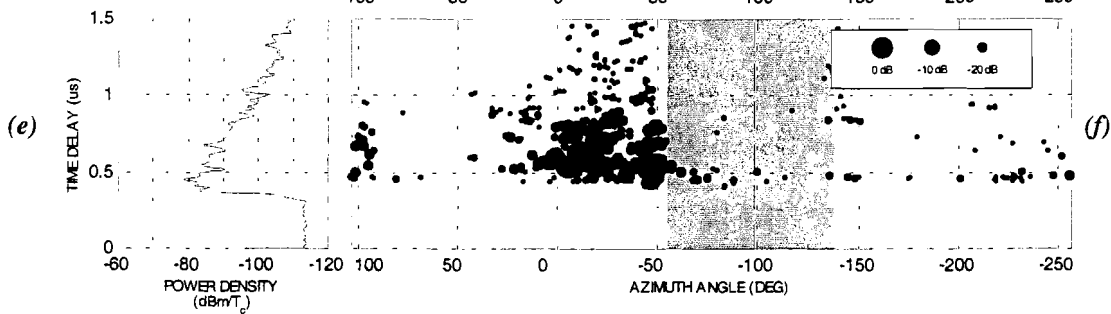
(e)

(f)

Figure B.9: Tx1 – Rx3.
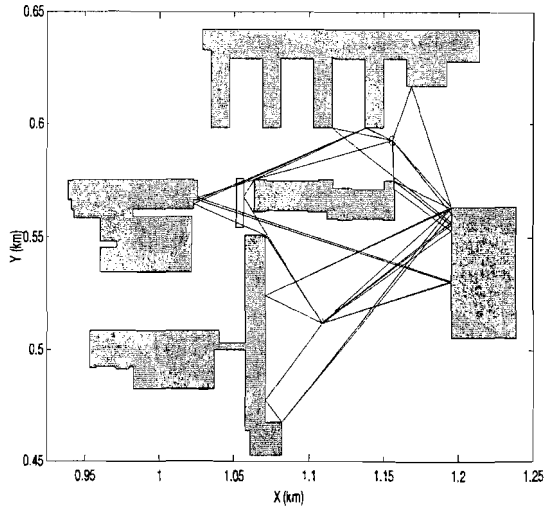
(a)
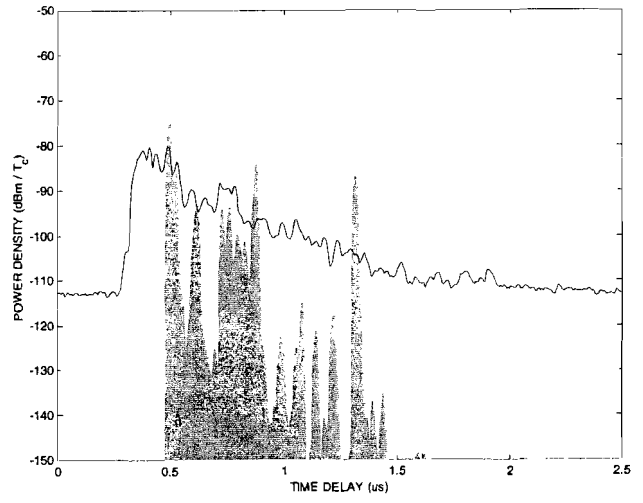
(b)
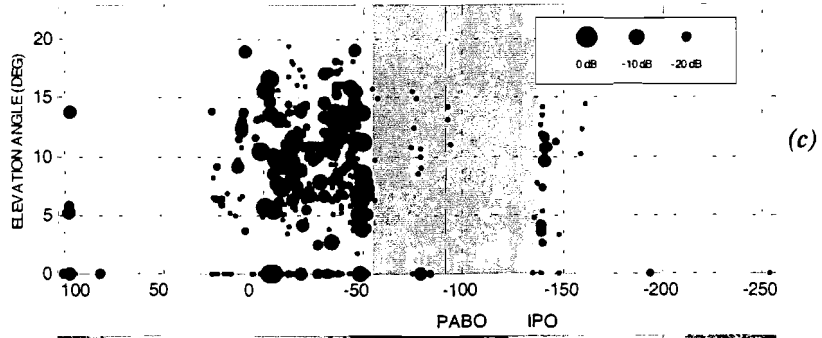
(c)
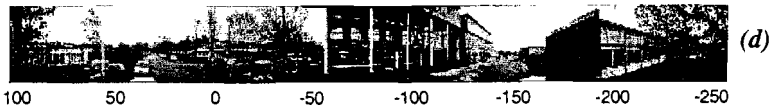
(d)
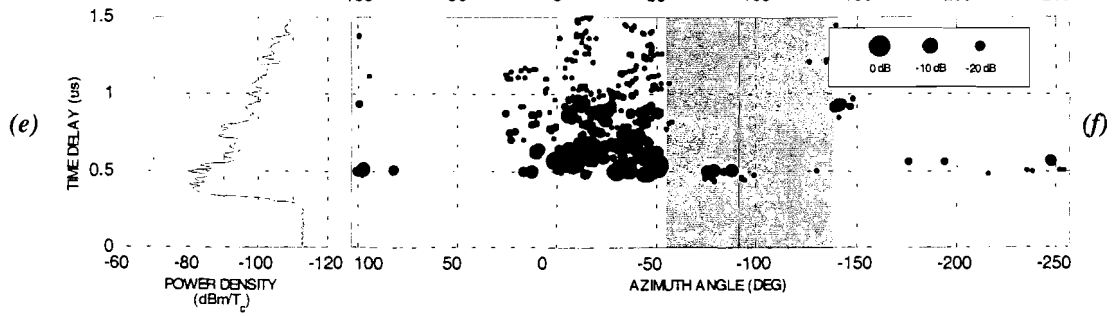
(e)

(f)

Figure B.10: Tx2 – Rx3.

(a)

(b)

(c)

(d)

(e)

(f)
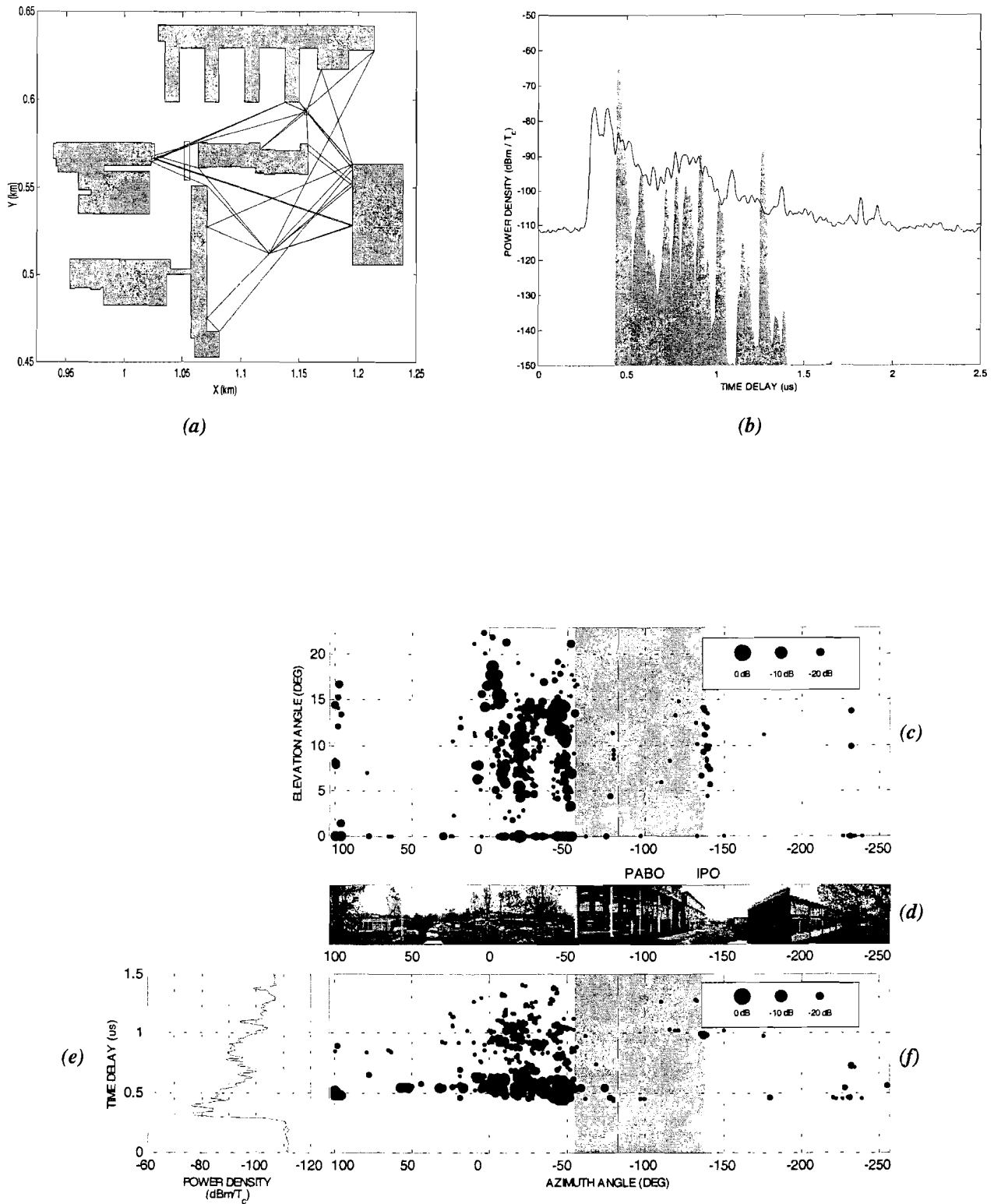
Figure B.11: Tx3 – Rx3.

(a)

(b)

(c)
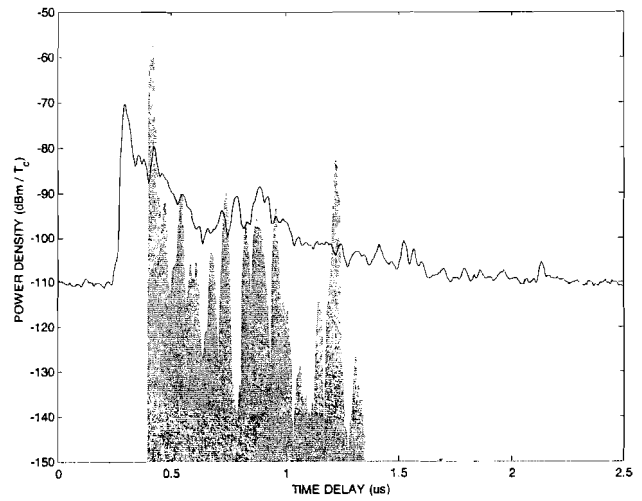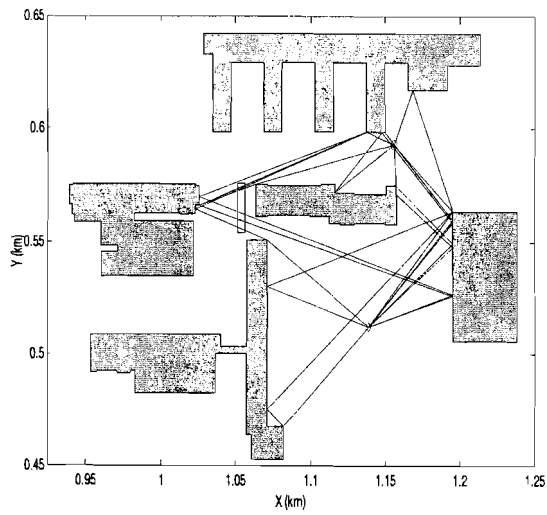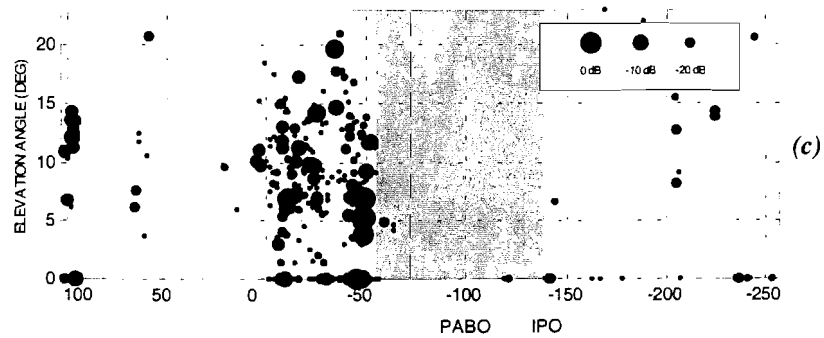
(d)
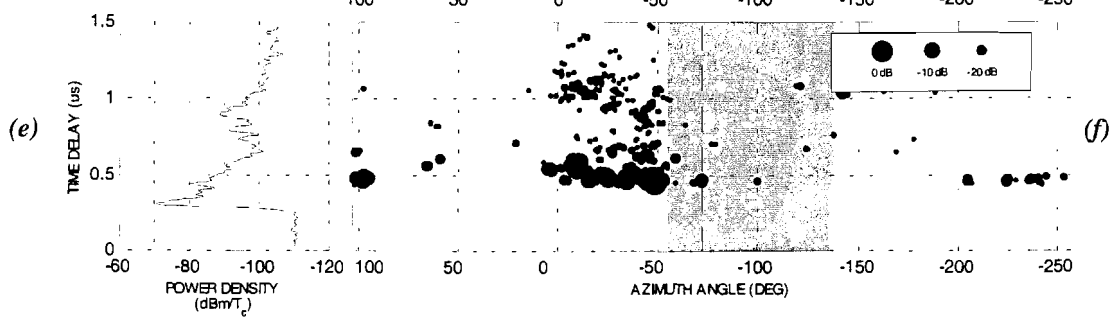
(e)

(f)

Figure B.12: Tx4 – Rx3.

Appendix C

Measurement results of buildings in microcells

Residential row houses

Heermoes
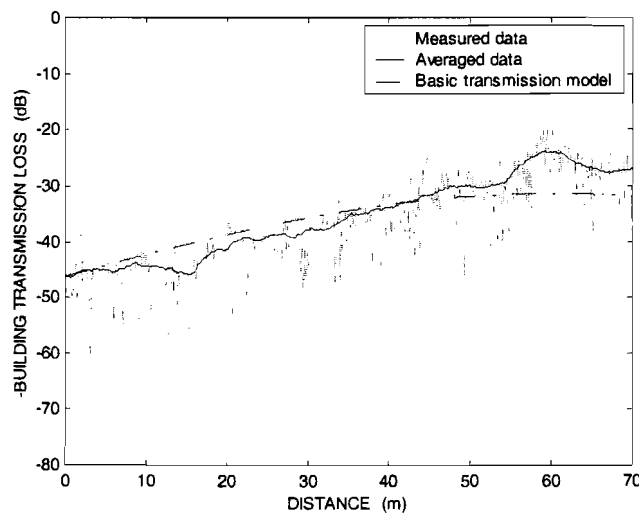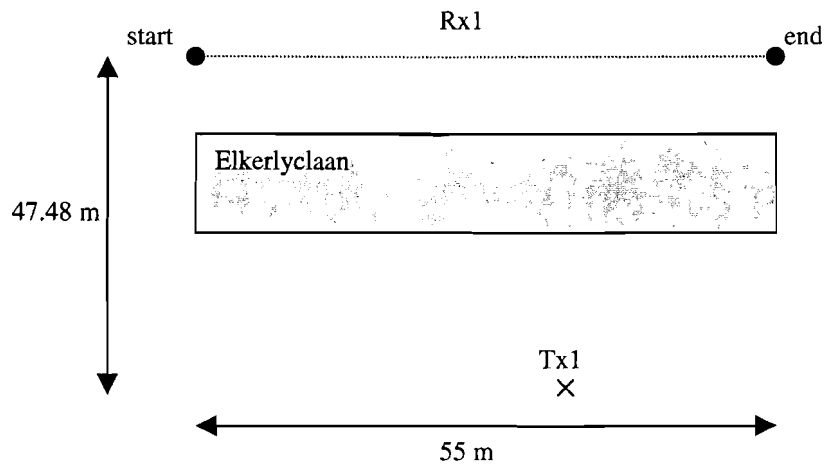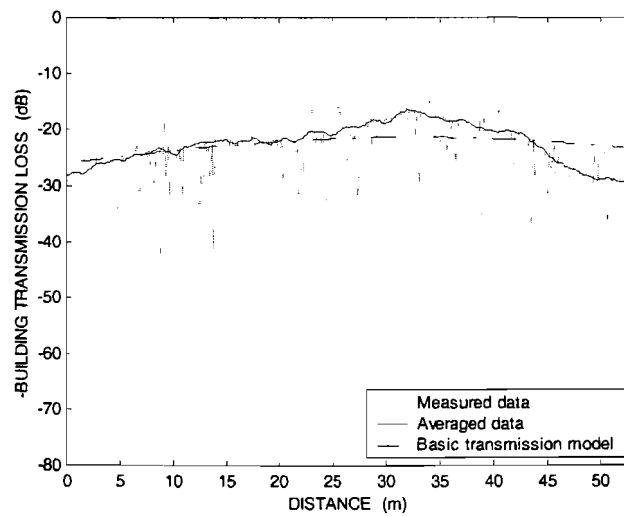

Back view.

Front view.
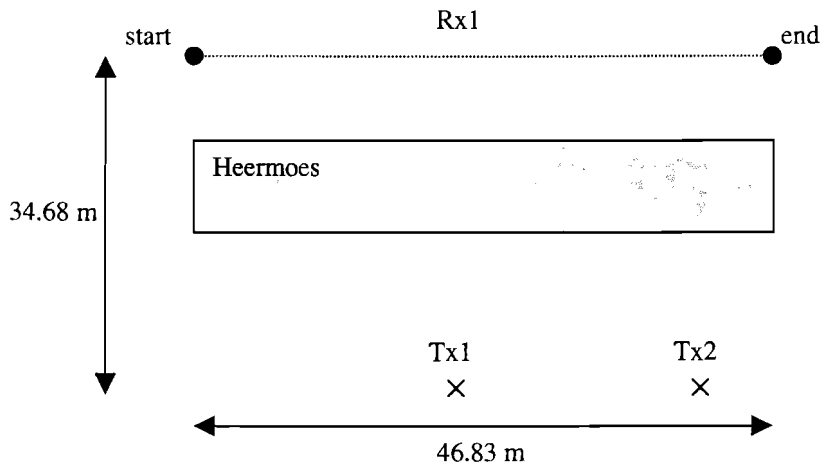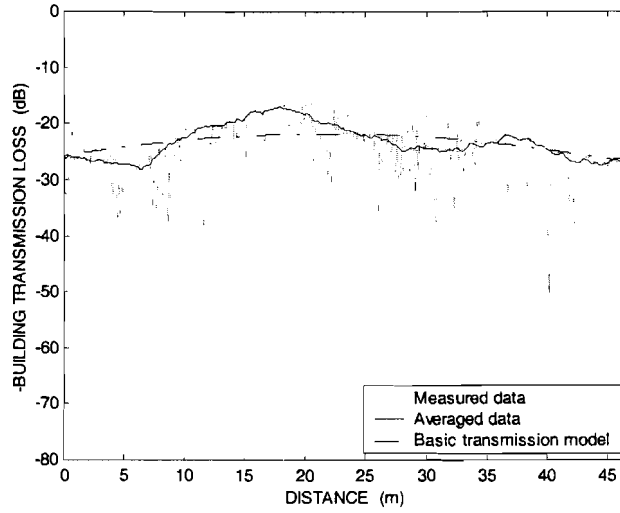
Plan view.

Comparison of Tx1 – Rx1 measured building transmission loss with basic transmission model.
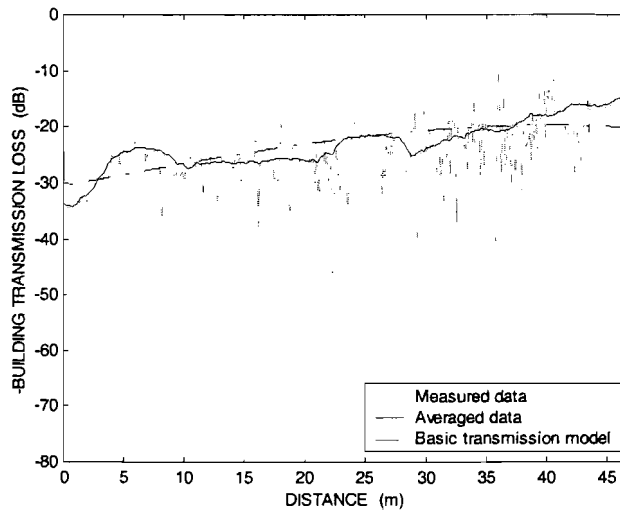
Comparison of Tx2 – Rx1 measured building transmission loss with basic transmission model.

Oudaen

Back view.
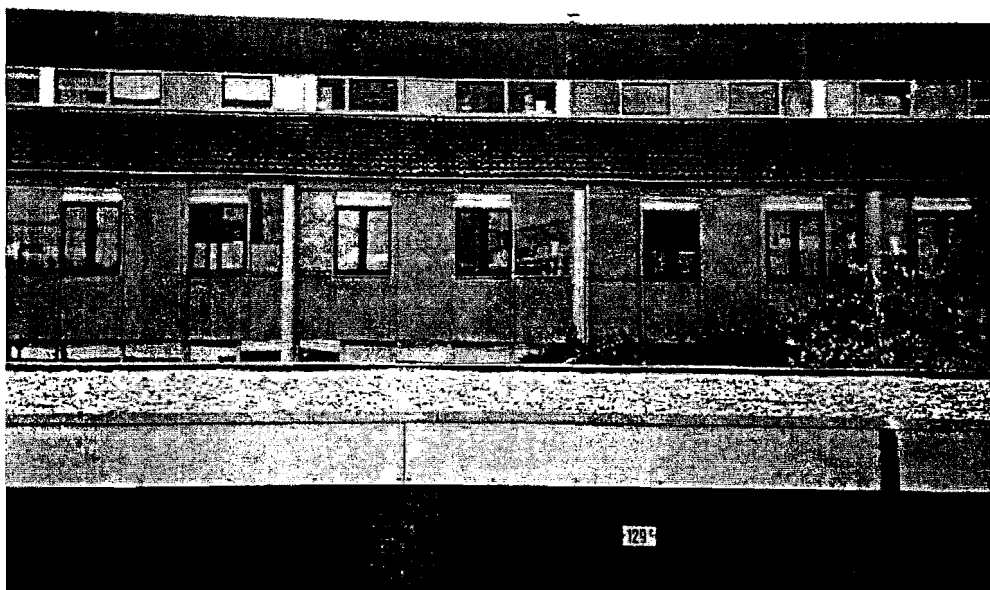
Front view.
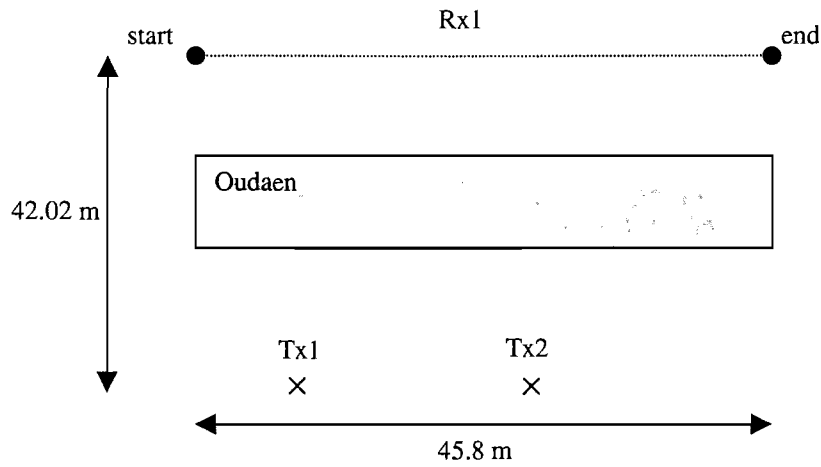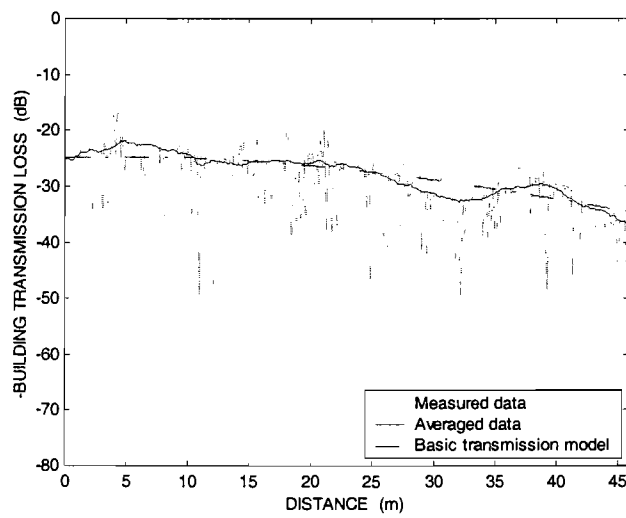
Rx1

start ●···● end

42.02 m

Oudaen

Tx1   Tx2
×   ×

45.8 m

Plan view.

*Comparison of Tx1 – Rx1 measured building transmission
loss with basic transmission model.*
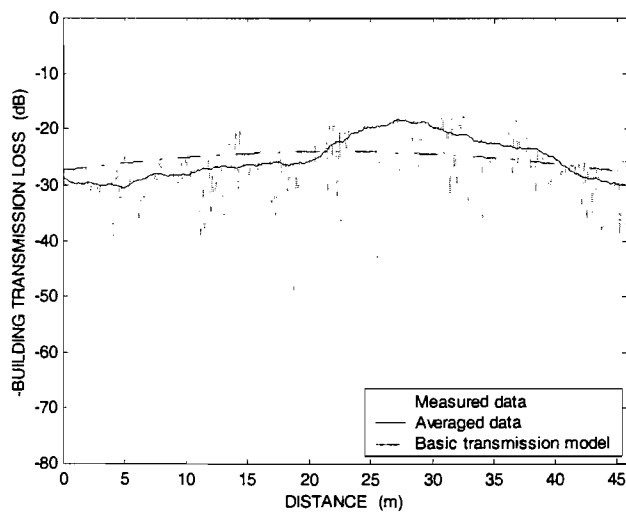
*Comparison of Tx2 – Rx1 measured building transmission
loss with basic transmission model.*

Kasteellaan

Back view.

Front view.
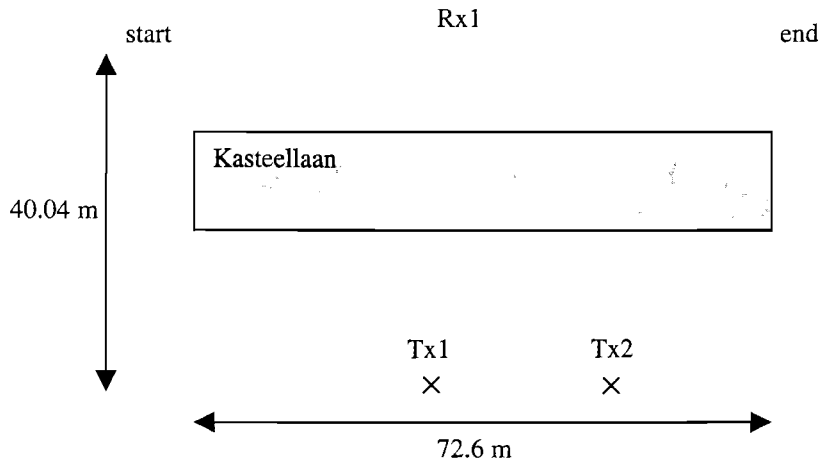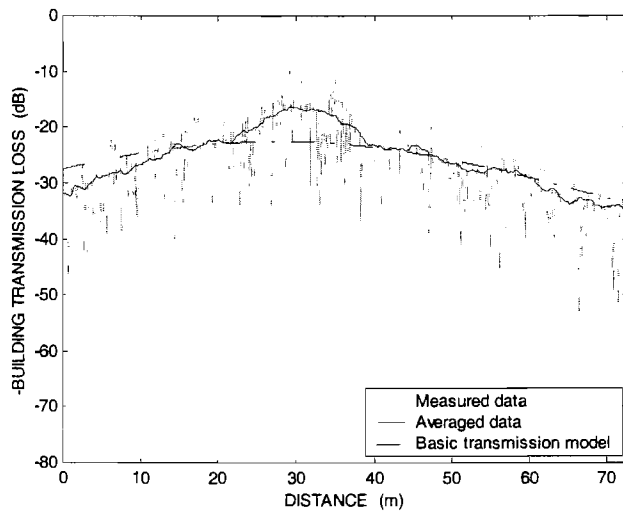
Plan view.

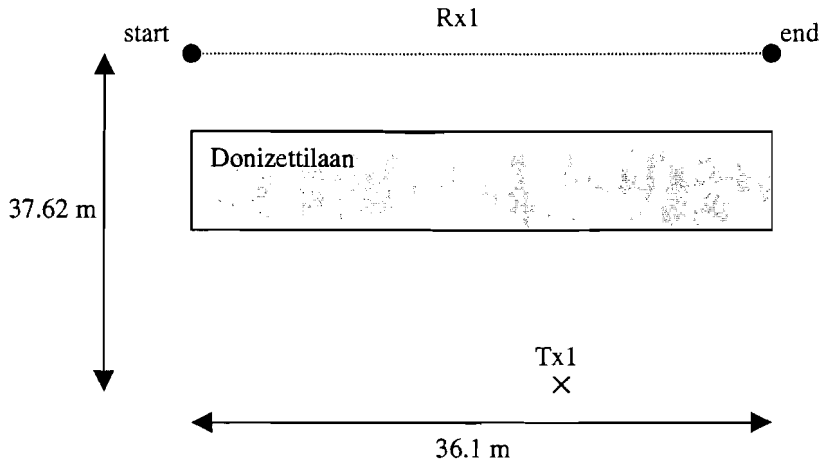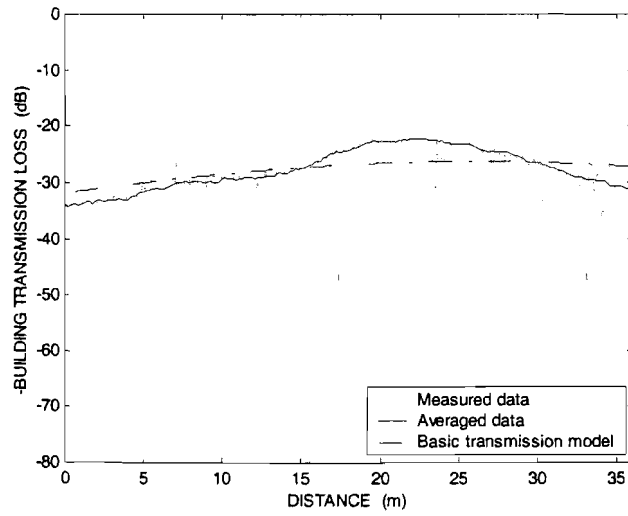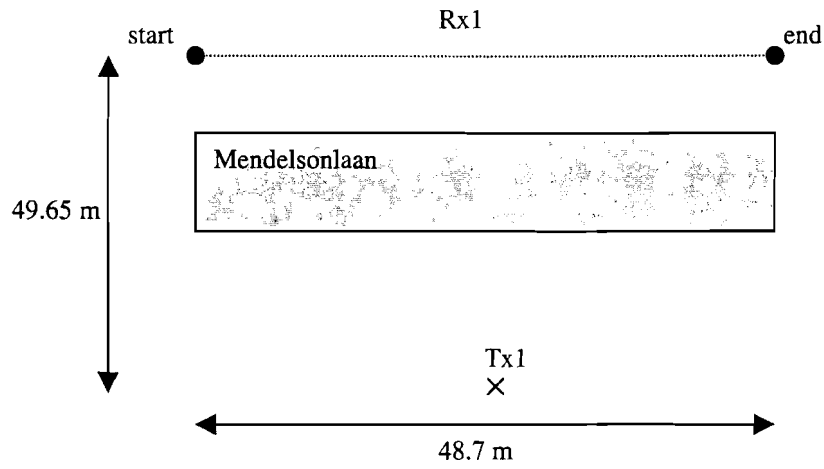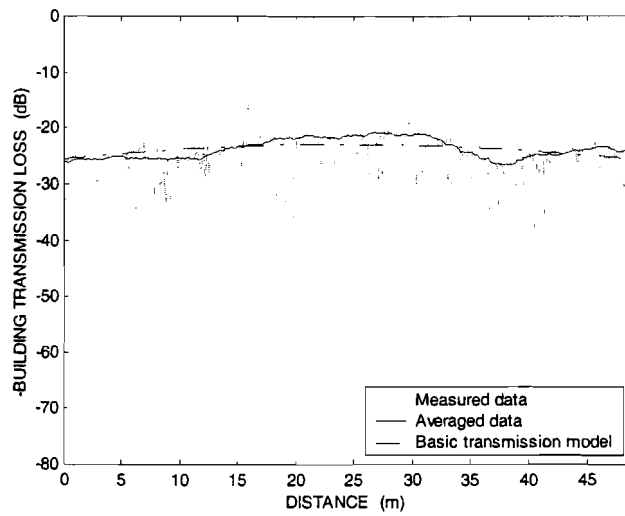*Comparison of Tx1 – Rx1 measured building transmission loss with basic transmission model.*
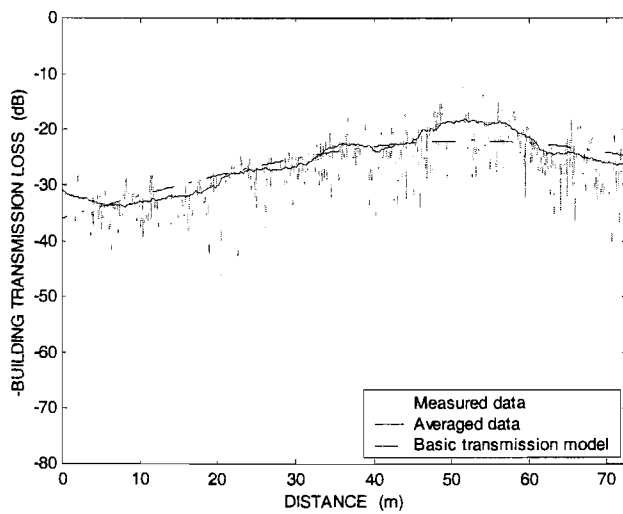
Comparison of Tx2 – Rx1 measured building transmission loss with basic transmission model.

Vivaldistraat

Back view.
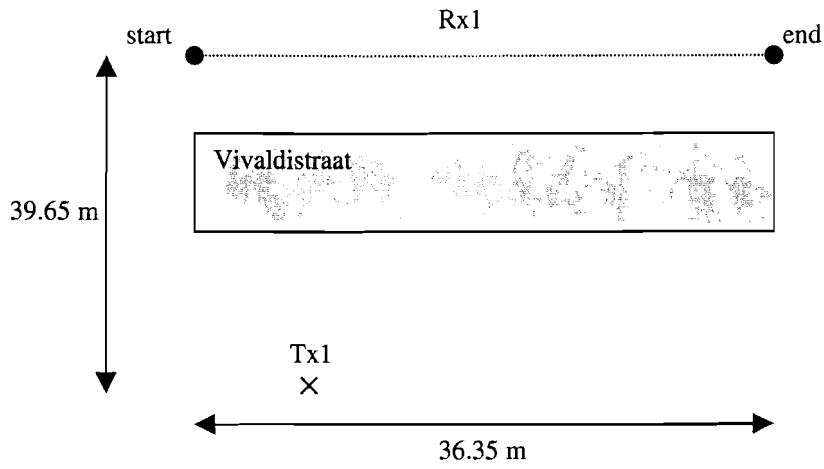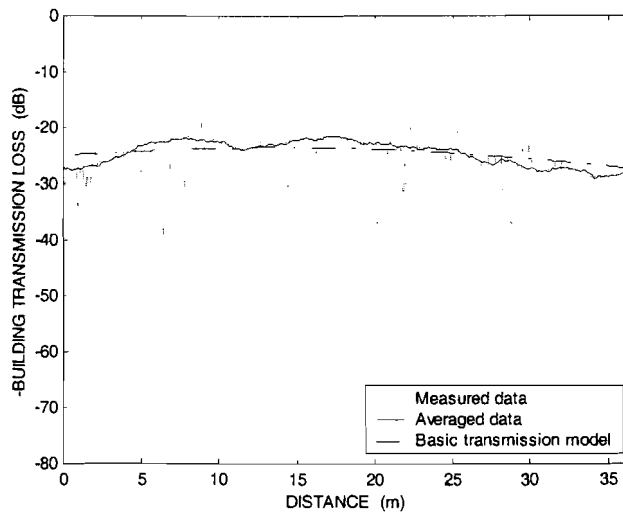
Front view.

Rx1

start ●··● end

39.65 m

Vivaldistraat

Tx1
×

←————————————————————→
36.35 m

Plan view.

*Comparison of Tx1 – Rx1 measured building transmission
loss with basic transmission model.*

Adelaarstraat

Back view.

Front view.

Rx1

start ●┄┄┄┄┄┄┄┄┄┄┄┄┄┄┄┄┄┄┄┄┄┄┄┄┄┄┄┄┄┄┄● end

Adelaartstraat

38.45 m

Tx1
×

72.5 m

Plan view.

Comparison of Tx1 – Rx1 measured building transmission loss with basic transmission model.

Appartments

Telemannlaan

Back view.

Front view.
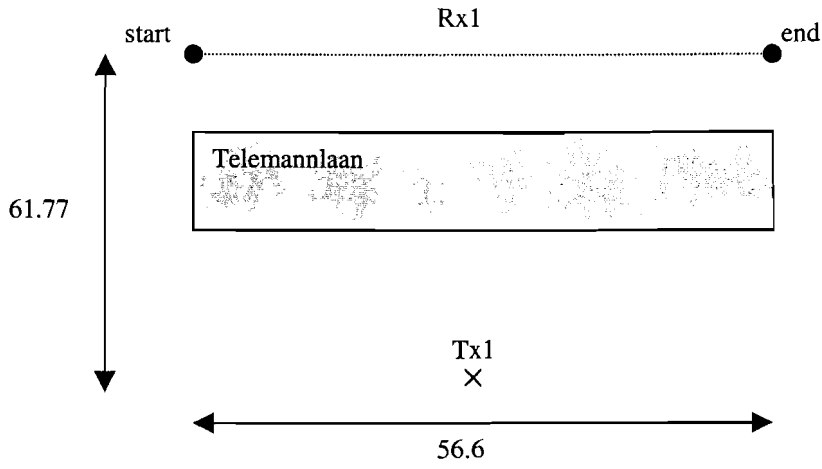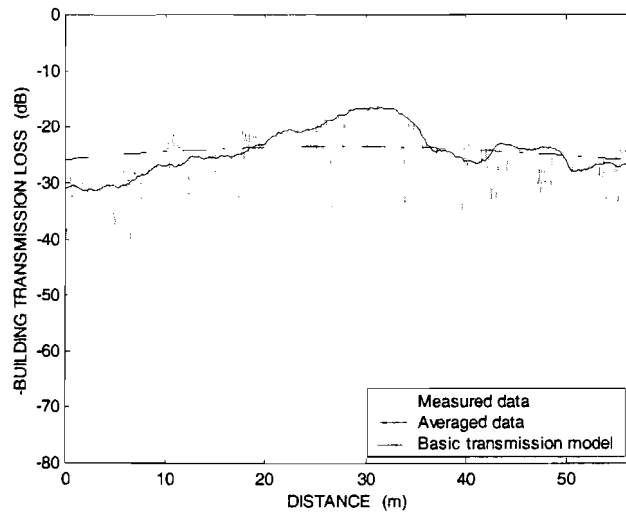
Plan view.

*Comparison of Tx1 – Rx1 measured building transmission
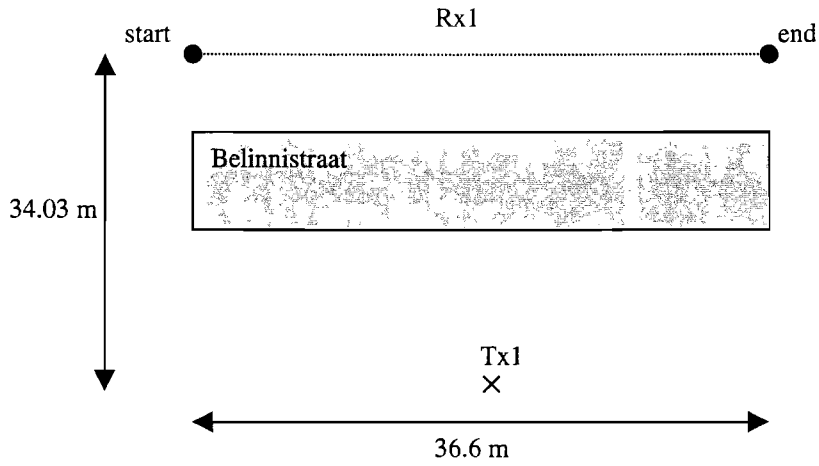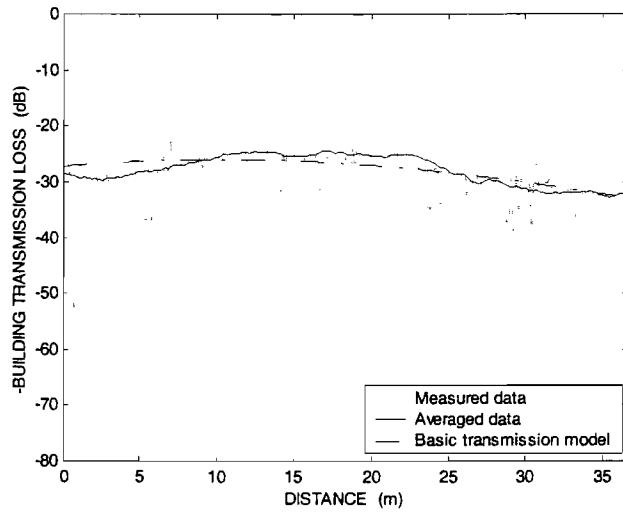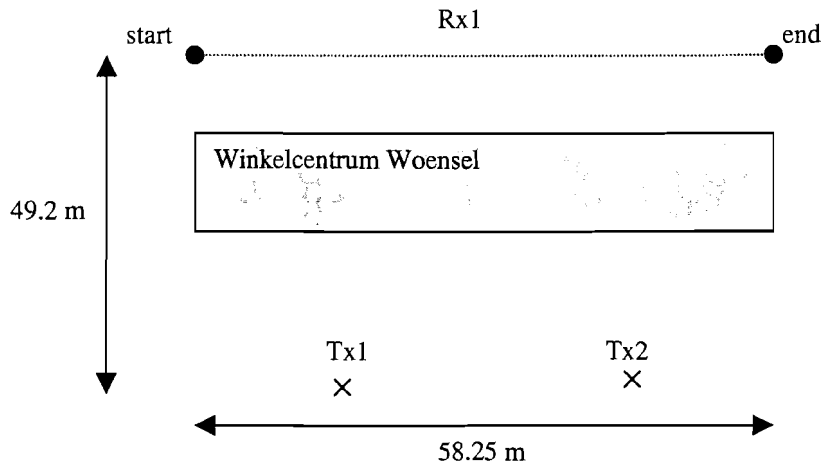loss with basic transmission model.*
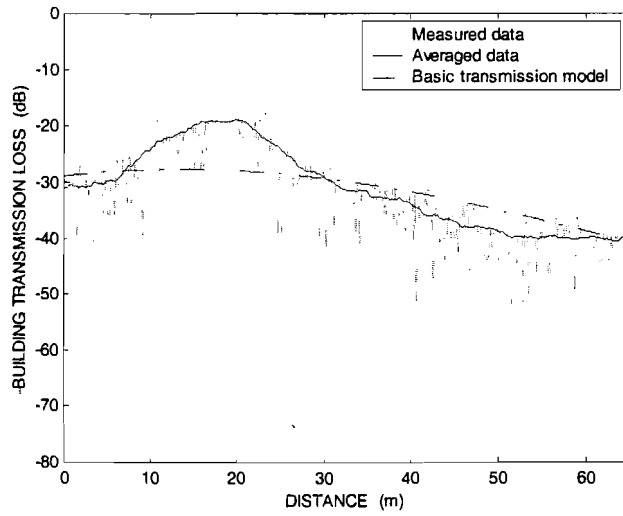
Regerweg
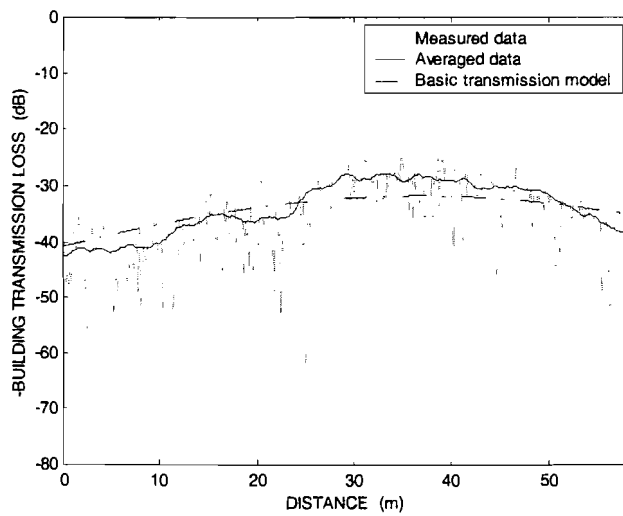

Back view.

Front view.
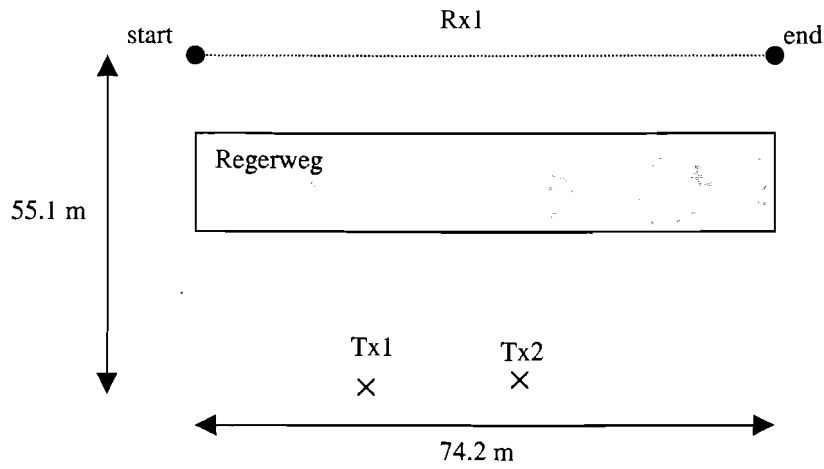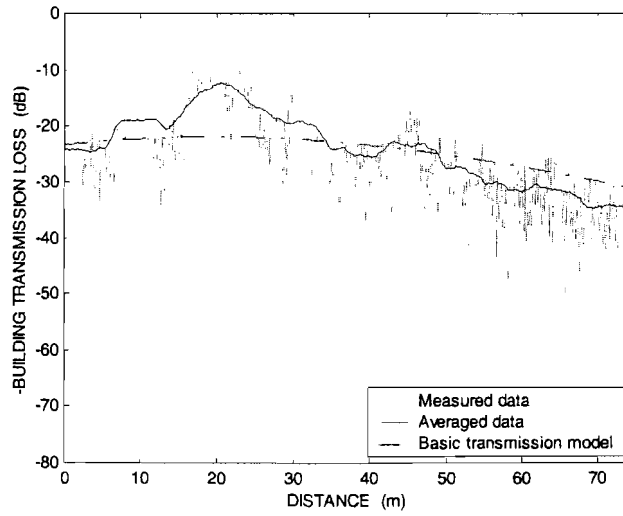
Plan view.

*Comparison of Tx1 – Rx1 measured building transmission
loss with basic transmission model.*
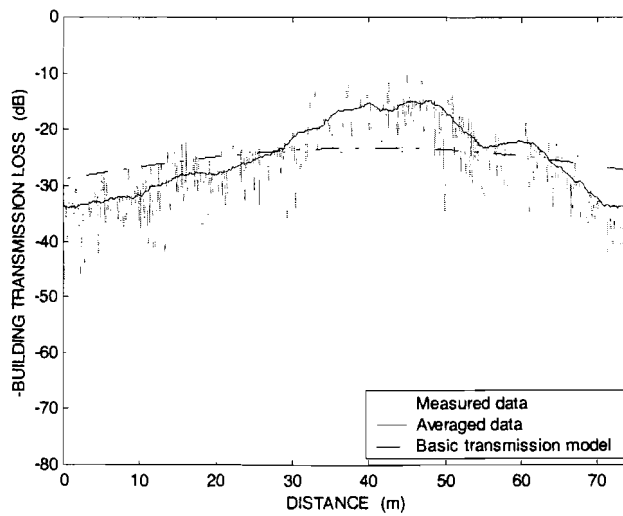
*Comparison of Tx2 – Rx1 measured building transmission
loss with basic transmission model.*

Genovevalaan

Back view.

Front view.
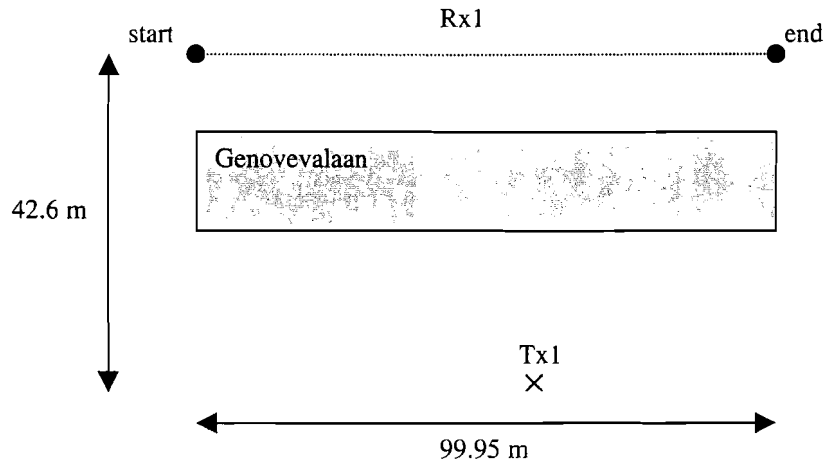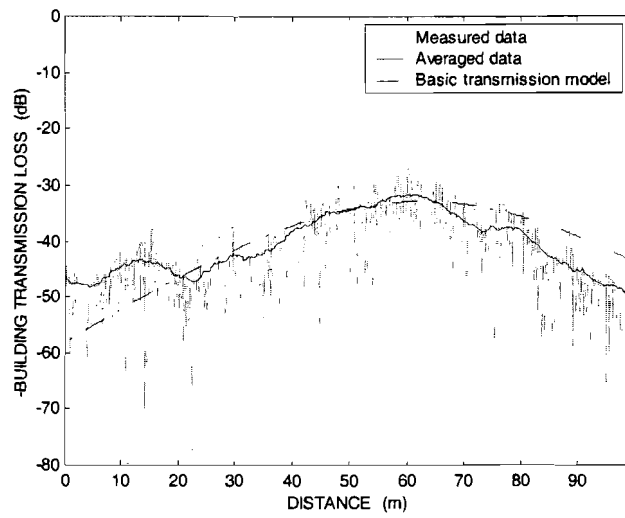
Plan view.

Comparison of Tx1 – Rx1 measured building transmission loss with basic transmission model.

Badelochstraat

Back view.

Front view.
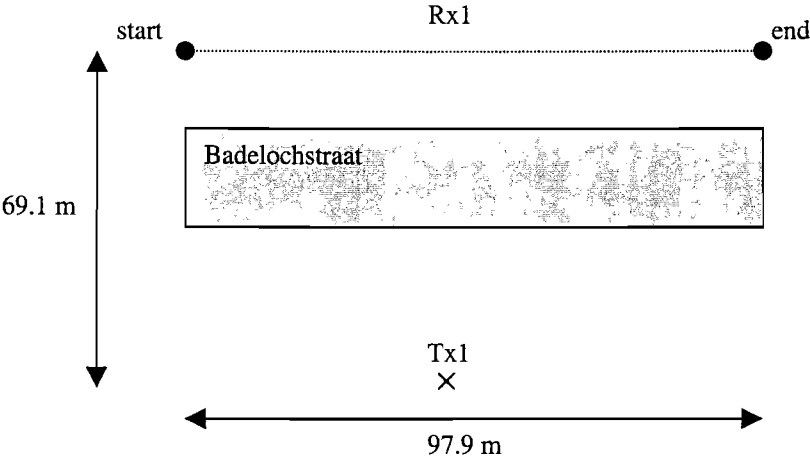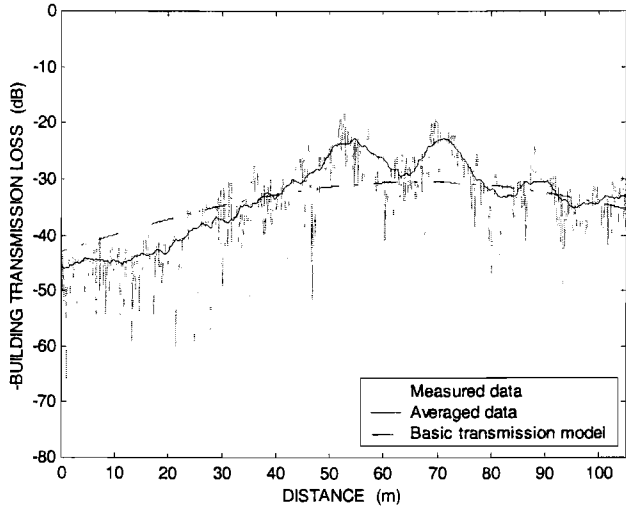
Plan view.

*Comparison of Tx1 – Rx1 measured building transmission
loss with basic transmission model.*

Fruinlaan

Back view.

Front view.
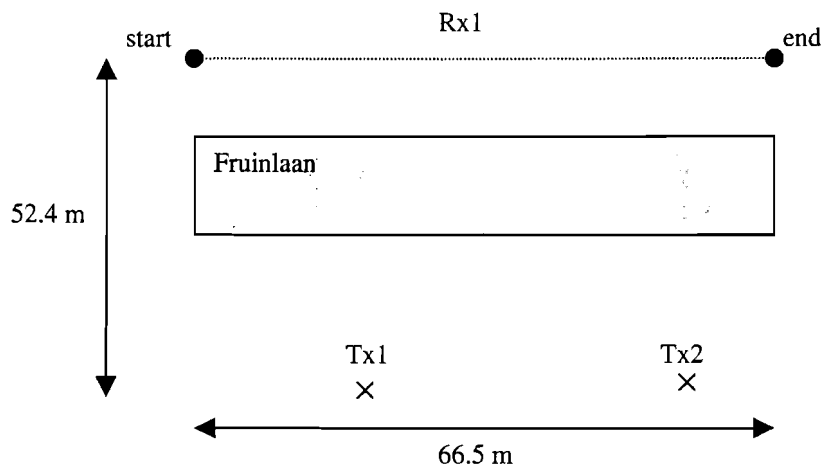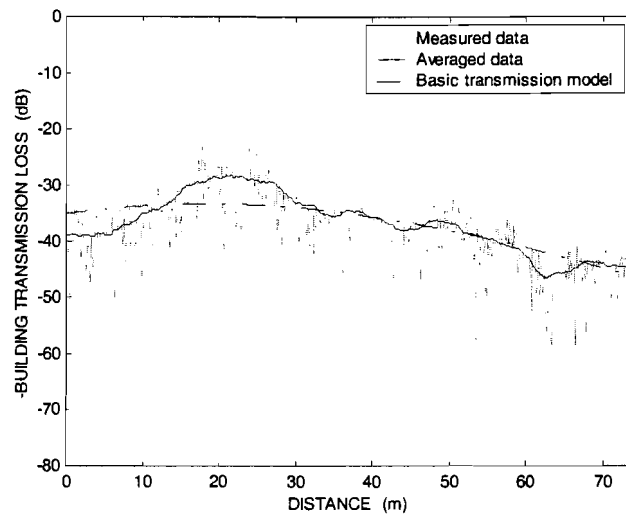
Plan view.

*Comparison of Tx1 – Rx1 measured building transmission
loss with basic transmission model.*

*Comparison of Tx2 – Rx1 measured building transmission
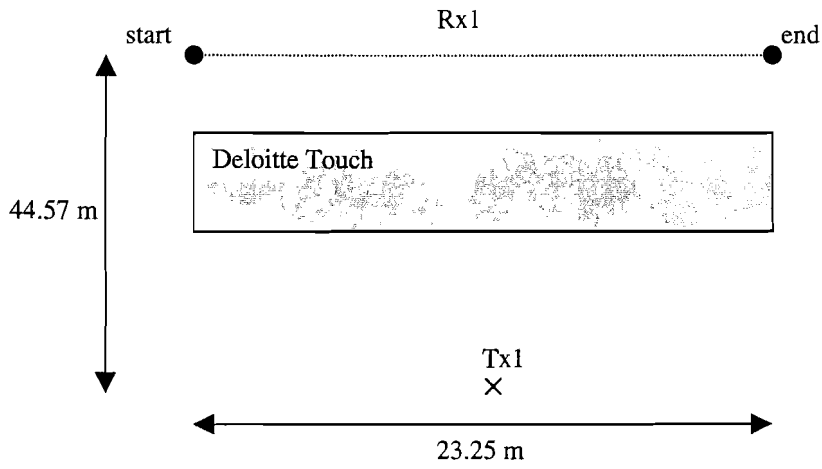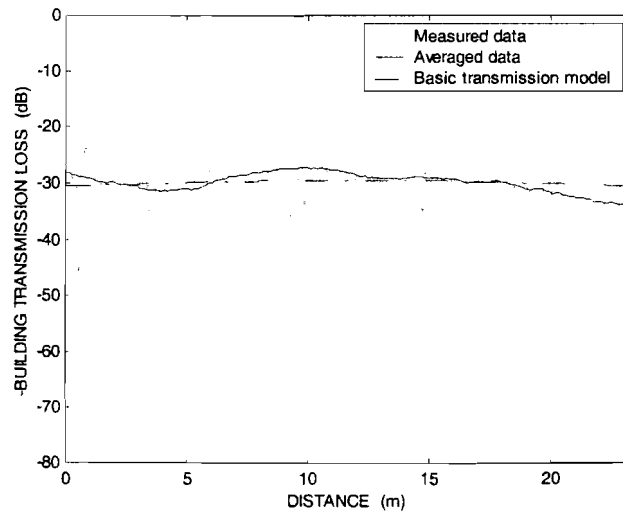loss with basic transmission model.*

Shops located beneath appartments

Elkerlyclaan

back view.

Front view.

Rx1

start ●···● end

Elkerlyclaan

47.48 m

Tx1
×

55 m

Plan view.

Comparison of Tx1 - Rx1 measured building transmission loss with basic transmission model.
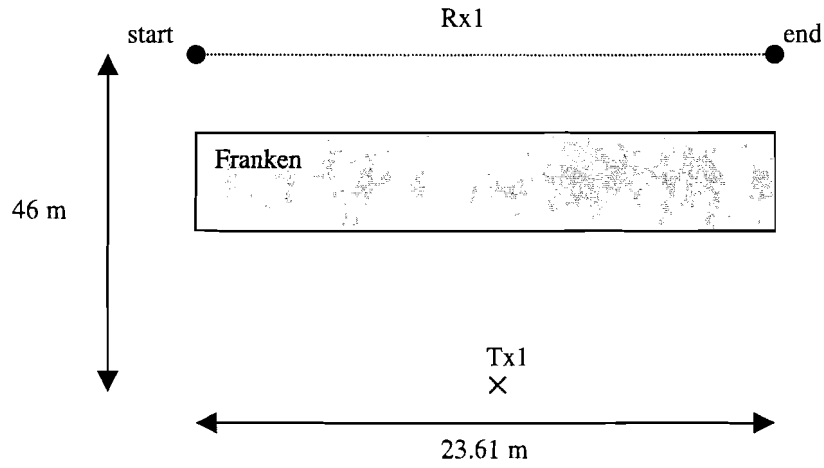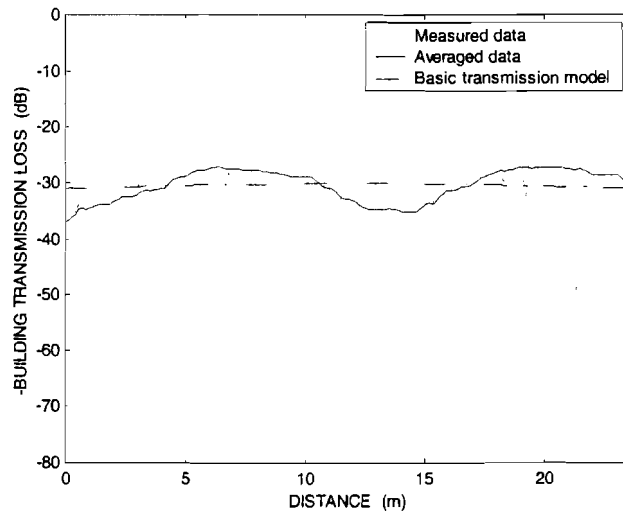
Donizettilaan
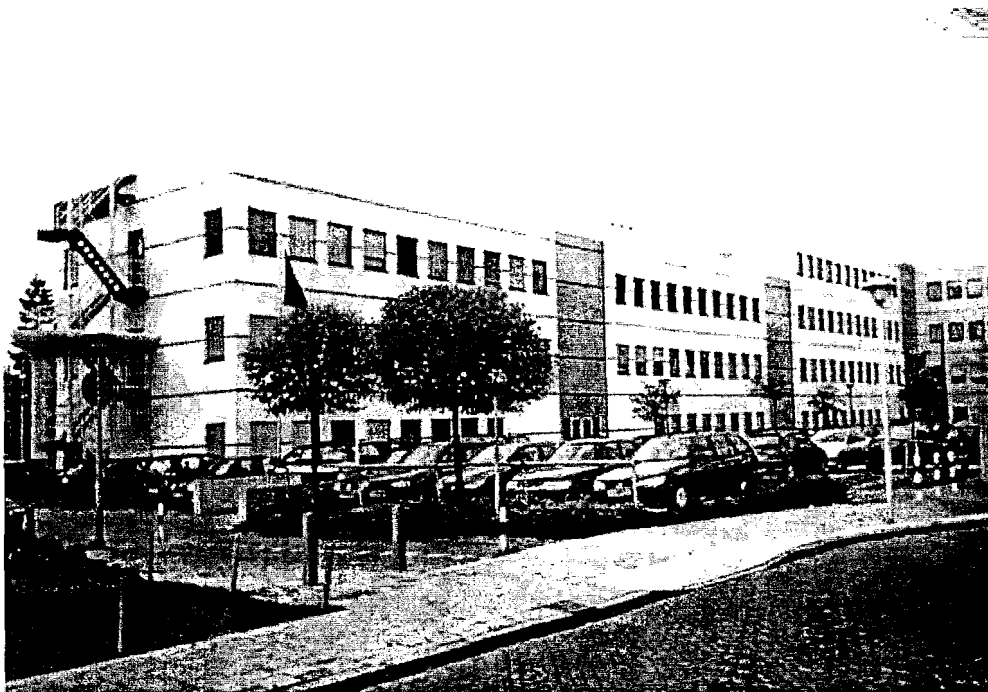

Back view.

Front view.

Plan view.

Comparison of Tx1 – Rx1 measured building transmission loss with basic transmission model.

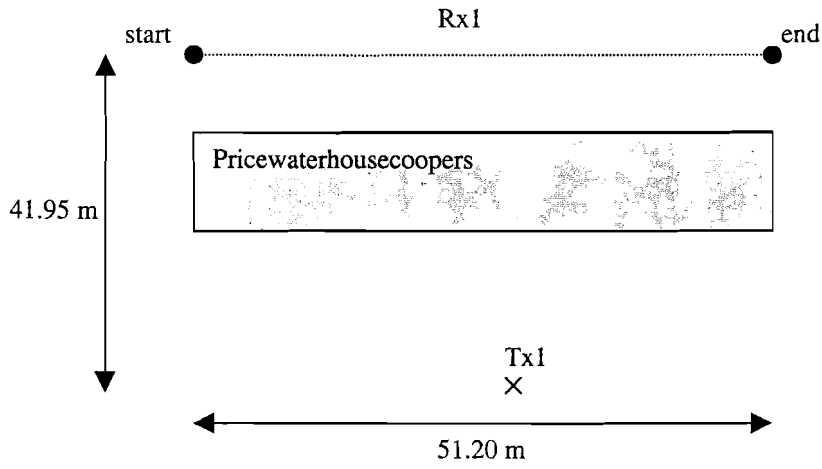# Mendelsonlaan

Back view.

Front view.

Rx1

start ●··● end

Mendelsonlaan

49.65 m

Tx1
×

48.7 m

Plan view.

*Comparison of Tx1 – Rx1 measured building transmission
loss with basic transmission model.*
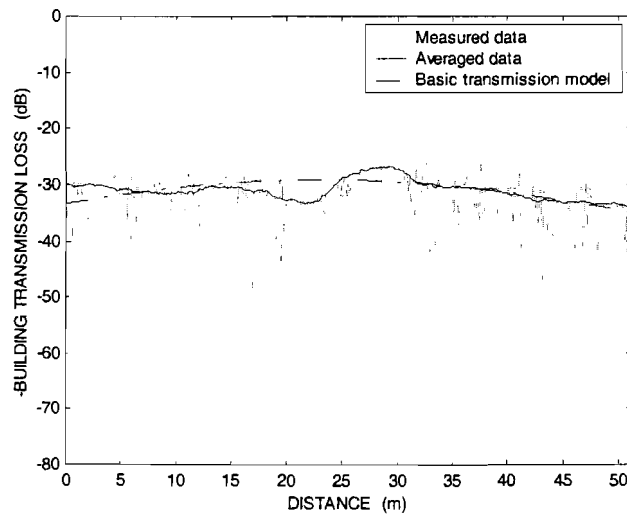
Belinnistraat

Back view.

Front view.

Plan view.

*Comparison of Tx1 – Rx1 measured building transmission
loss with basic transmission model.*

Winkelcentrum Woensel

Back view.

Front view.

Rx1

start ● ⋯⋯⋯⋯⋯⋯⋯⋯⋯⋯⋯⋯⋯⋯⋯⋯⋯⋯⋯⋯ ● end

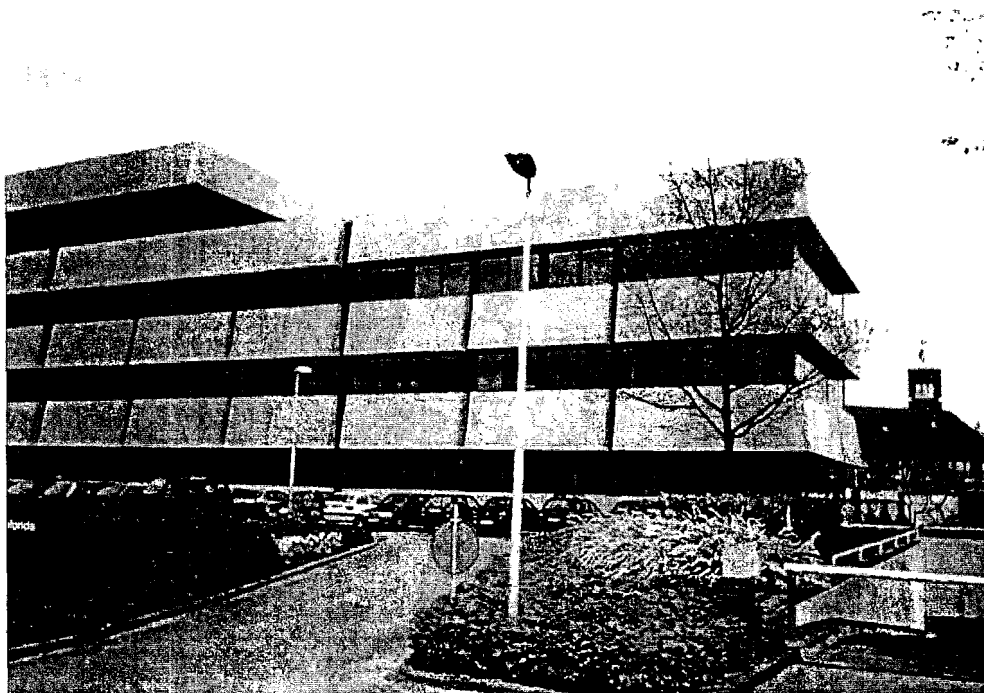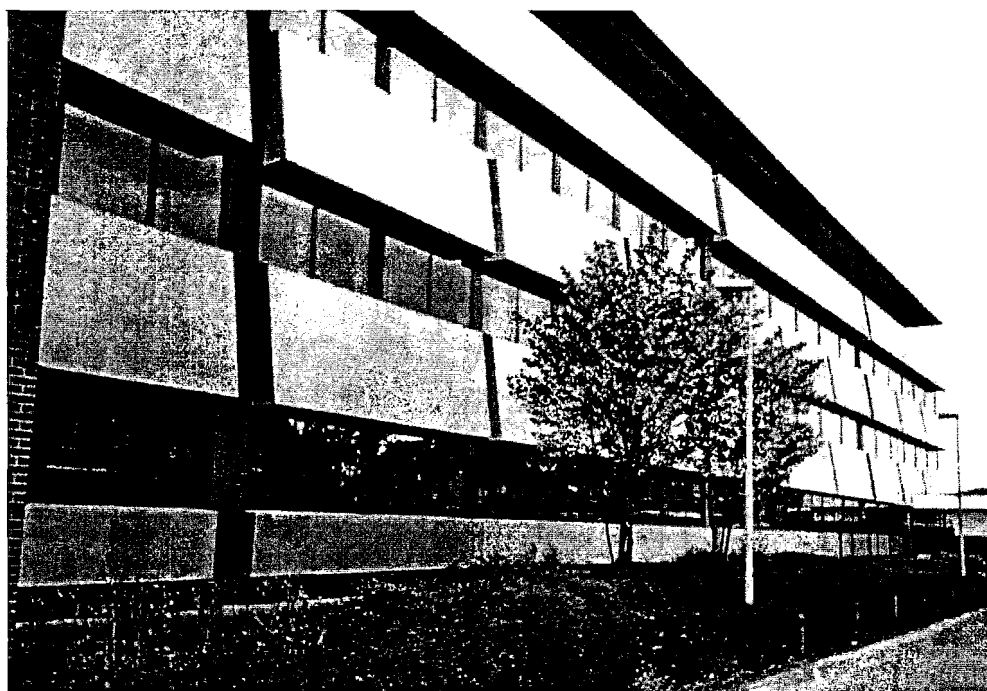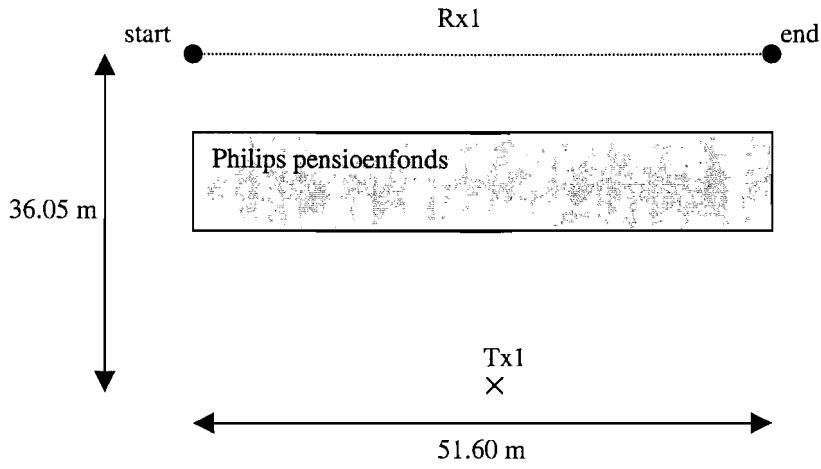49.2 m

| Winkelcentrum Woensel |

Tx1
✕

Tx2
✕

58.25 m

Plan view.

Comparison of Tx1 – Rx1 measured building transmission
loss with basic transmission model.

Comparison of Tx2 – Rx1 measured building transmission
loss with basic transmission model.

Office buildings

Deloitte touch

Back view.

Front view.

Rx1

start   end
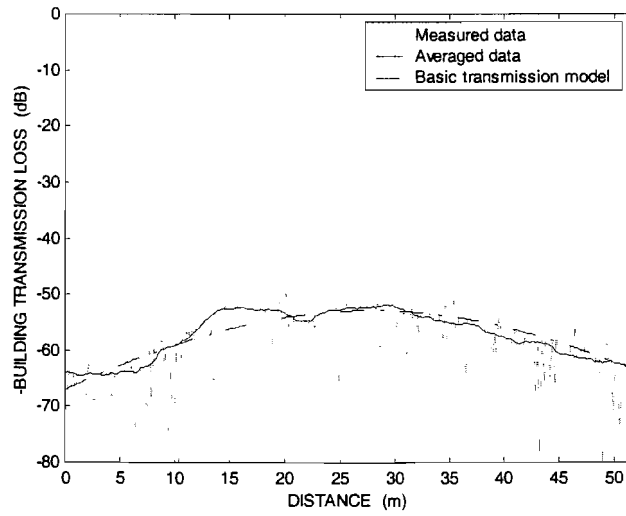
44.57 m

Deloitte Touch

Tx1
×

23.25 m

Plan view.

Comparison of Tx1 – Rx1 measured building transmission loss with basic transmission model.

Franken

Back view.

Front view.

Rx1

start ●···● end

| 46 m

Franken

Tx1
×

←——————————————————→
23.61 m

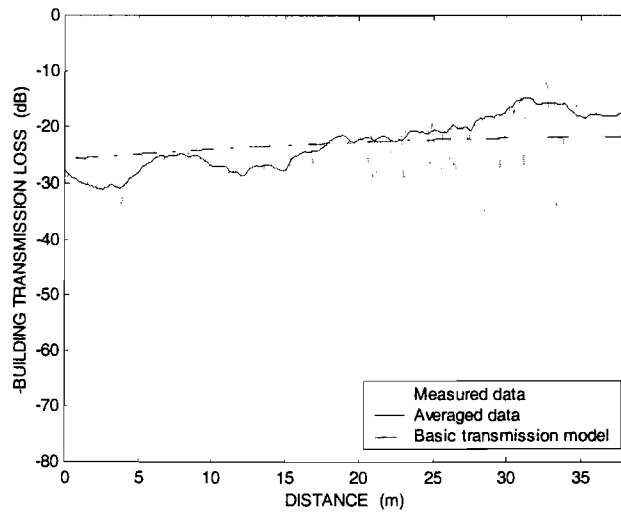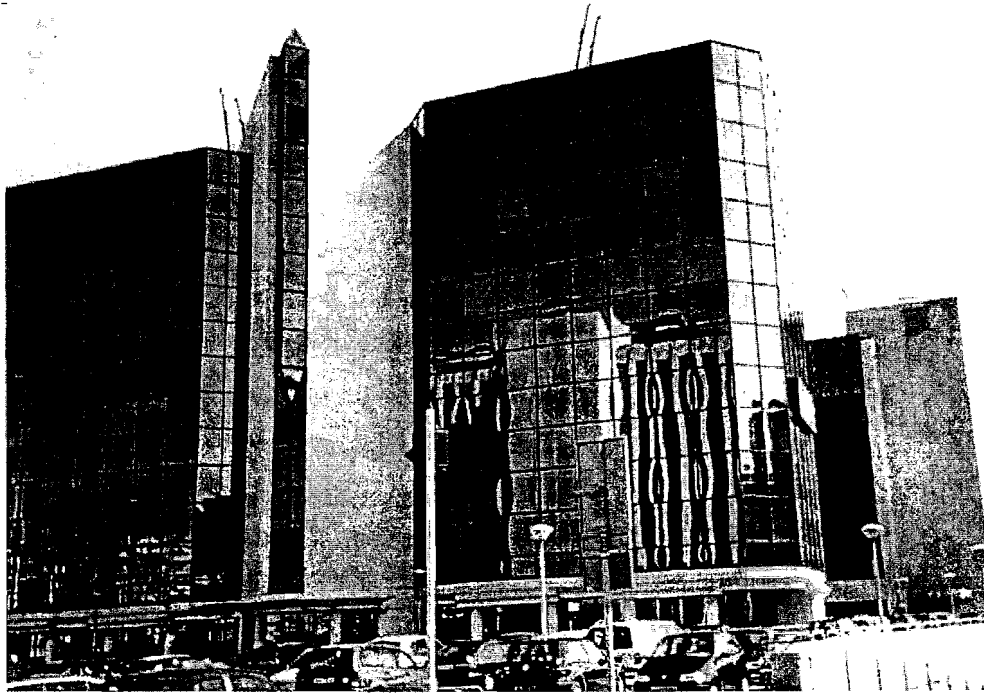*Plan view.*

*Comparison of Tx1 – Rx1 measured building transmission
loss with basic transmission model.*

Pricewaterhousecoopers

Back view.

Front view.

start ●···● end

Rx1

Pricewaterhousecoopers

41.95 m

Tx1
×

← 51.20 m →

Plan view.

*Comparison of Tx1 – Rx1 measured building transmission
loss with basic transmission model.*

Philips pensioenfonds

Back view.

Front view.

Rx1

start ●···● end

Philips pensioenfonds

36.05 m

Tx1
×

←————————————————————→
51.60 m

Plan view.

*Comparison of Tx1 – Rx1 measured building transmission
loss with basic transmission model.*
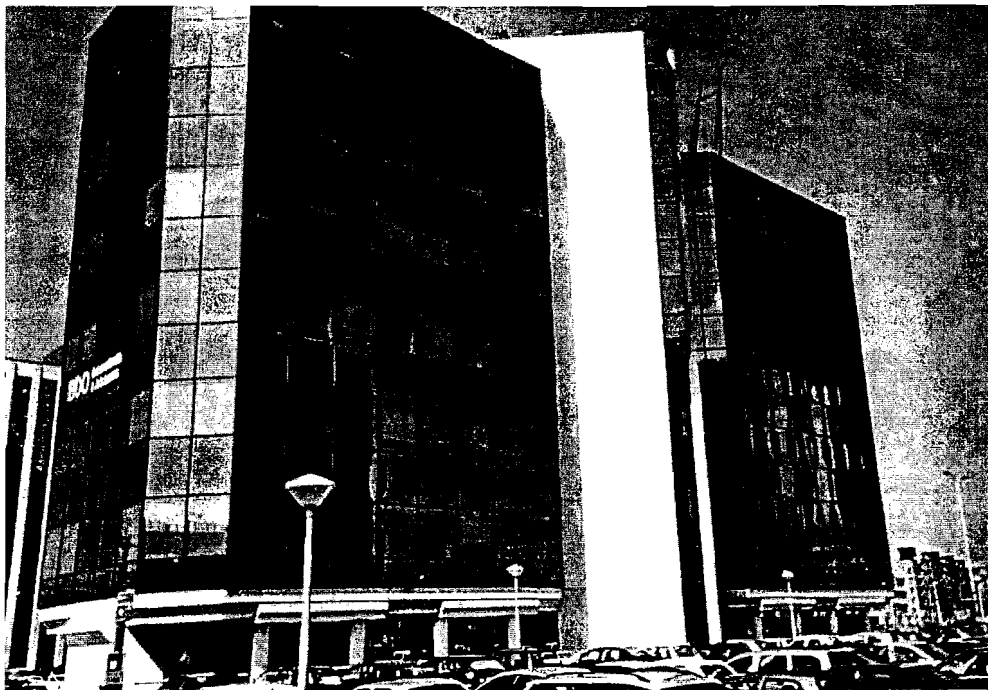
Randstad

Back view.

Front view.
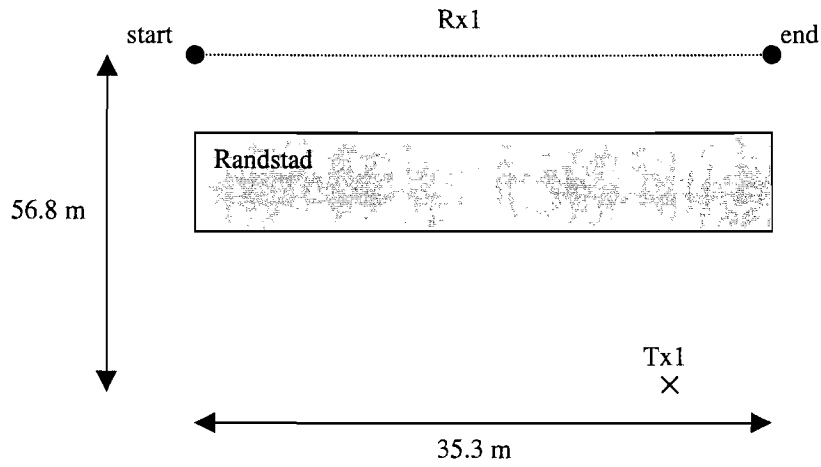
Plan view.

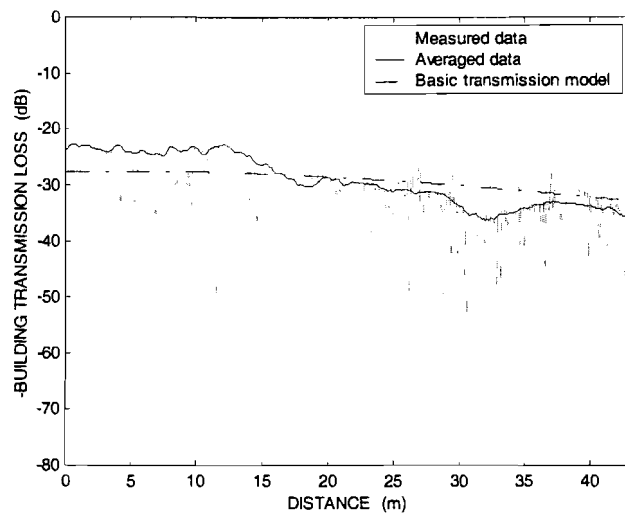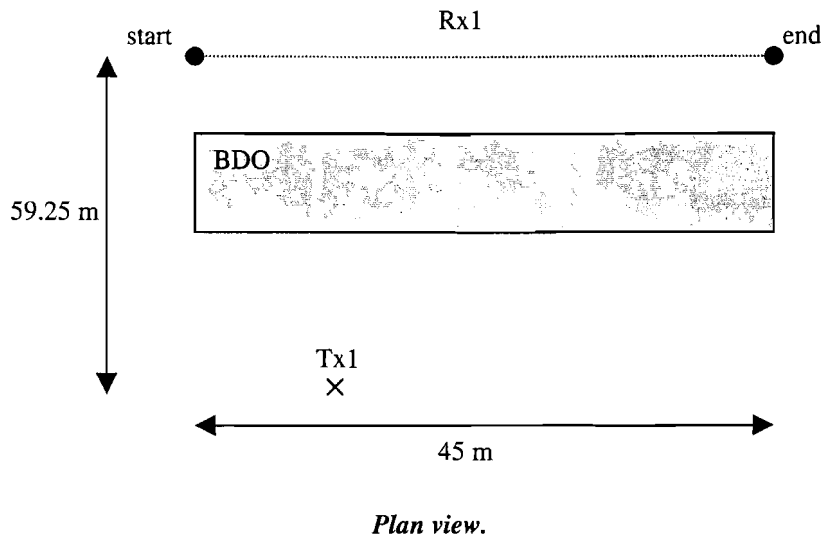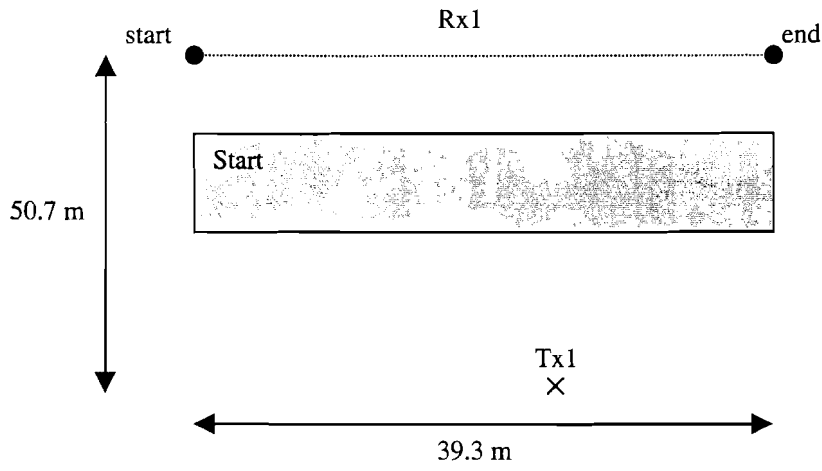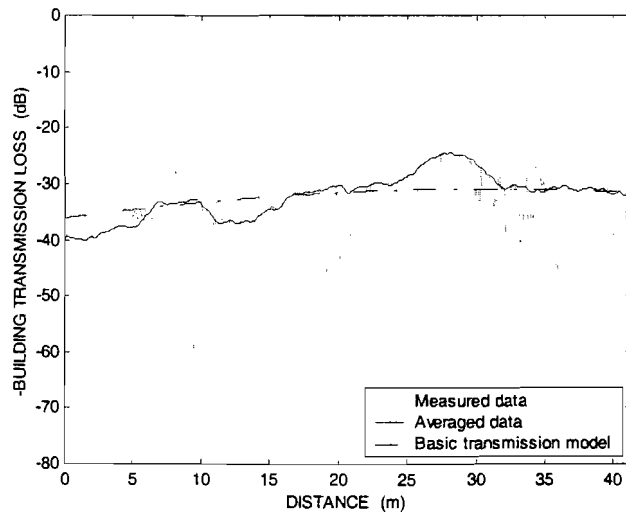*Comparison of Tx1 – Rx1 measured building transmission loss with basic transmission model.*

BDO

Back view.

Front view.

Rx1

start ●···● end

59.25 m

BDO

Tx1
×

◄──────────────────────── 45 m ────────────────────────►

Plan view.

Comparison of Tx1 – Rx1 measured building transmission loss with basic transmission model.
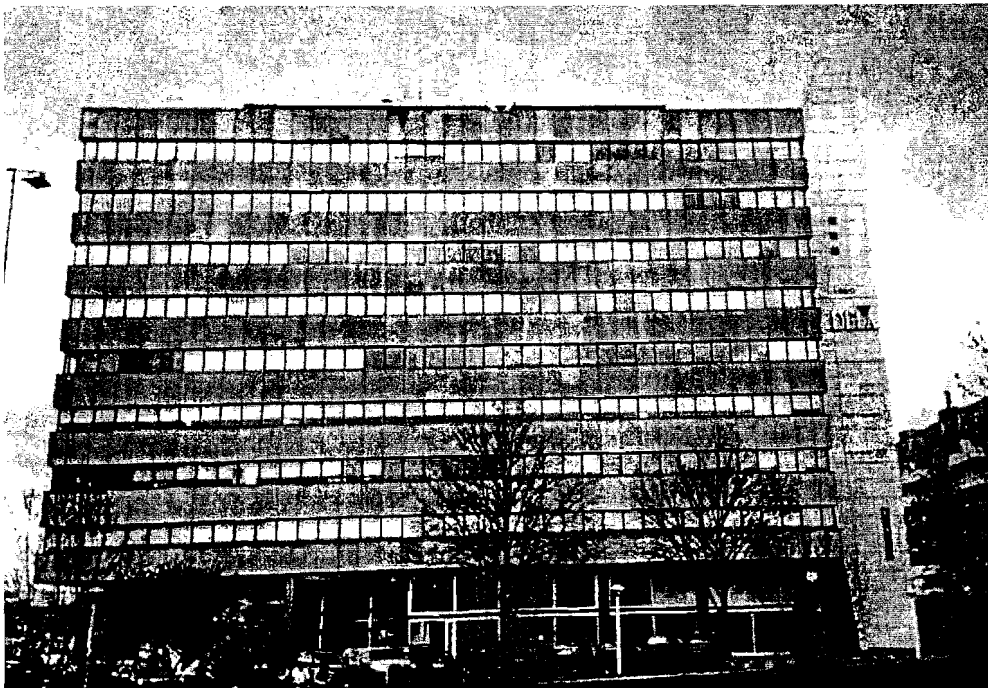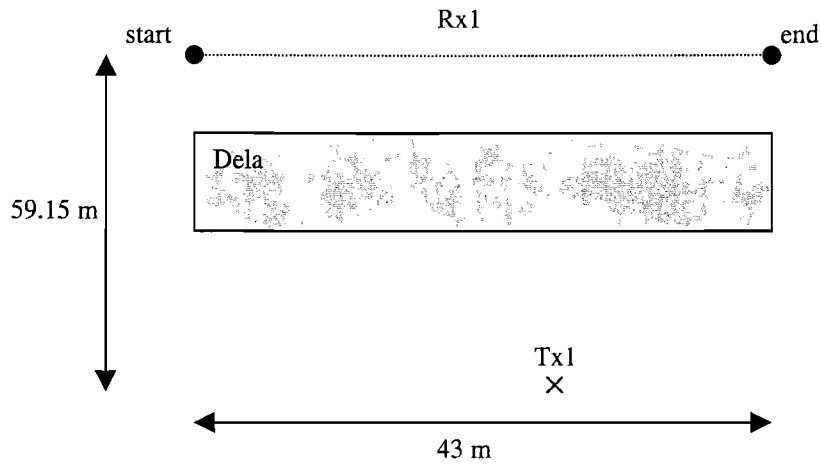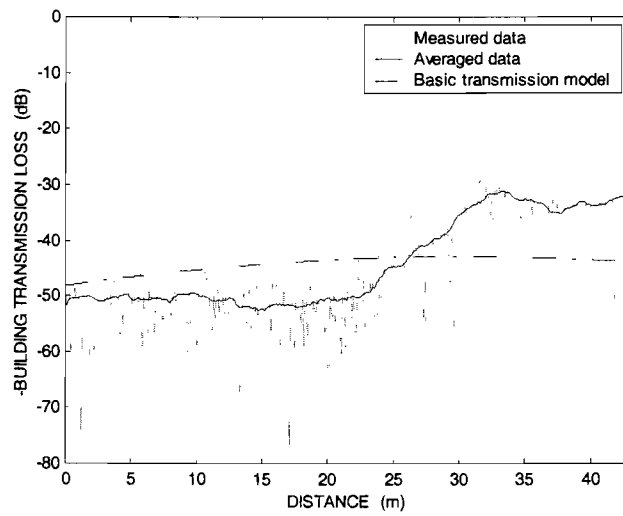
Start

Back view.

Front view.

Plan view.

Comparison of Tx1 – Rx1 measured building transmission loss with basic transmission model.

Dela

Back view.

Front view.

Rx1

start ●·· ● end

Dela

59.15 m

Tx1
×

←———————————— 43 m ————————————→

Plan view.

Comparison of Tx1 – Rx1 measured building transmission loss with basic transmission model.